OPTIMIZATION OF MAGNETIC SUSCEPTIBILITY MEASUREMENTS

OPTIMIZATION OF MAGNETIC SUSCEPTIBILITY MEASUREMENTS ON ULTRATHIN FILMS

By

KATHARINA FRITSCH, B.SC.

A Thesis

Submitted to the School of Graduate Studies

in Partial Fulfilment of the Requirements

for the Degree

Master of Science

McMaster University

MASTER OF SCIENCE (2008) McMaster University
(Physics) Hamilton, Ontario

TITLE: Optimization of Magnetic Susceptibility Measurements on Ultrathin Films

AUTHOR: Katharina Fritsch, B.Sc. (Universität Leipzig, Germany)

SUPERVISOR: Dr. D. Venus

NUMBER OF PAGES: xvii, 152

Abstract

The magnetic properties of ultrathin magnetic films can be investigated *in situ* by the temperature dependent magnetic ac susceptibility $\chi(T)$ using an optical technique - the surface magneto-optic Kerr effect (SMOKE). The performance of the ac susceptibility measurements depends primarily on the optical setup used to detect the Kerr effect and on the mechanical stability of the system. Modifications to the optical setup and the sample holder have significantly reduced the influence of noise due to mechanical vibrations. It has been found that the signal-to-noise ratio has been improved by at least a factor of 2.5 with respect to the previous setup, giving a detection limit of 15 nrad/Oe. This improvement makes measurements on antiferromagnetic ultrathin films feasible. Their susceptibility response has been estimated to be around 20-30 nrad/Oe. As a test study for the performance of the improved setup, transverse susceptibility measurements on 2 ML Fe/W(110) ferromagnetic ultrathin films are presented. These transverse susceptibility signals show interesting features. They have a narrow linewidth and are larger than expected from anisotropy considerations and other work. Also, it has been found that the in-plane and out-of-plane transverse susceptbilities arise from different mechanisms. Several scenarios that might explain the origin, size and shape of the observed signals are discussed.

Acknowledgements

I would like to acknowledge and extend my heartfelt gratitude to the following persons who have made the completion of this thesis possible:

- My supervisor, David Venus, for 2 years of guidance and support,
- Marek Kiela for his invaluable technical assistance and his friendship,
- my comrade in the lab, Nidal, for passing me lab skills and cheering me up when things did not go as planned,
- my friends amongst the graduate students at McMaster,
- and my parents, my constant source of encouragement and support.

Contents

List of Figures

List of Tables

Chapter 1

Introduction

One of the most active fields in experimental condensed matter physics is the investigation of low-dimensional magnetic systems such as ultrathin films, multilayers or magnetic nanostructures. Interest in these materials has been prompted by the observation of novel magnetic phenomena in these systems that differ profoundly from the respective bulk properties [1], and by the perspectives for a variety of technological applications in magnetic data storage industry or in the relatively new field of spintronics [2].

Many interesting phenomena in magnetic ultrathin film systems are a result of the reduced symmetry at the surfaces or interfaces and depend crucially on the balance of the exchange, dipole and anisotropy energies. For the study of magnetic ultrathin films, the controlled and reproducible preparation of high-quality films is imperative. In this thesis, ultrathin films are prepared in an ultrahigh vacuum (UHV) environment using a well-developed technique called molecular beam epitaxy (MBE). Magnetic measurements on

ultrathin films can be realized by a variety of experimental methods, but there is only a small number that allows a non-destructive, *in situ* investigation of the magnetic properties.

One of these *in situ* techniques is the magnetic ac susceptibility χ that is measured in our group by using an optical technique - the surface magneto-optic Kerr effect (SMOKE) [3]. The Kerr effect refers to the rotation of the plane of linear polarization when light is scattered from a magnetic surface. In the past, through careful optical alignment and lock-in detection, small polarization rotations on the order of 10^{-7}-10^{-8} radians could be detected. The ac susceptibility is obtained by applying a small ac magnetic field δH to the magnetic sample to induce a magnetic response that is detected as a Kerr rotation angle $\delta\phi$. Upon changing the temperature of the film, the temperature dependent susceptibility $\chi(T)$ becomes accessible.

The subject of this thesis is the optimization of the ac susceptibility measurements by SMOKE with the goal to increase the sensitivity of the setup. An increased sensitivity is expected to make the detection of susceptibility signals from antiferromagnetic ultrathin films possible. These films usually exhibit a much weaker response since they have no net magnetic moment and couple weakly to an applied magnetic field. The detection of antiferromagnetic ordering in ultrathin films using the magnetic ac susceptibility has, to our knowledge, not yet been achieved. So far, only measurements on thicker films by means of neutron diffraction techniques [4] or on the topmost surface layers by spin-polarized scanning tunneling microscopy [5] or soft X-ray

magnetic dichroism (XMCD) [6] have been reported. The detection of the antiferromagnetic state or of critical properties of antiferromagnetic/ferromagnetic exchange coupled ultrathin films by means of the ac susceptibility would therefore be a major advance in the field.

In order to increase the performance of the setup as used prior to this thesis, the optical setup will be modified to reduce the effect of mechanical vibrations that introduce intensity fluctuations that can cause a false signal at the photodetector on the order of the expected signal sizes. Following this, the signal-to-noise ratio for ac susceptibility measurements will be calculated and compared to previous work. Finally, the improved setup will be used to detect ferromagnetic transverse susceptibilities along the magnetically hard axes of Fe/W(110). The size of these signals should be comparable to that expected from antiferromagnetic ultrathin films because the mechanism giving rise to the susceptibility signal is similar.

This thesis is organized as follows. Following this introduction, chapter 2 will outline the theoretical background relevant to ultrathin film magnetism. The magnetic ac susceptibility technique will be described as a tool for the investigation of surface magnetism. Furthermore, the surface magneto-optic Kerr effect is treated in some detail as the susceptibility measurements in this thesis rely on it. Theoretically expected susceptibility signal sizes for antiferromagnetic ultrathin films are calculated.

Chapter 3 will describe the experimental setup and experimental methods relevant for this thesis. Special emphasis is placed on the implementation

and modification of the optical setup for the detection of the surface magneto-optic Kerr effect and the ac susceptibility.

In chapter 4, the improved system for the measurement of the magnetic ac susceptibility will be characterized with respect to its performance. A simple model incorporating system-specific noise sources will be used to determine the signal-to-noise ratio in typical susceptibility measurements and to compare it to work on the old system by C.S. Arnold. At the end of this chapter, the feasibility of ac susceptibility measurements on antiferromagnetic ultrathin films with the improved setup will be discussed.

The performance of the optimized setup will be tested in experiments on a previously studied 1-2 ML Fe/W(110) system in chapter 5 by means of the transverse susceptibility. It will be shown that the system has been improved with success since very small signals can be detected that have not been observed prior to this thesis. Moreover, the observed transverse susceptibility signals on the Fe/W(110) films exhibit surprising features that will be summarized in the main part of this chapter. Finally, possible explanations of these features will be discussed.

Chapter 6 will present the major conclusions of this work.

Chapter 2

Theory

This chapter will give an overview of the magnetic theory relevant for ultrathin film magnetism. In particular, the most important interactions that determine the magnetic properties of thin films will be introduced. The magnetic ac susceptibility technique will be described in detail as a tool for the investigation of magnetic properties of ultrathin films. The chapter will conclude with a discussion of the surface magneto-optic Kerr effect as the basis for the susceptibility measurements performed in this thesis.

2.1 Magnetic interactions in ultrathin films

The magnetic properties of ultrathin films depend on the interplay between three fundamental interactions: The strong short-range isotropic exchange interaction, the weaker long-range anisotropic dipolar interaction, and the magnetic anisotropy. This section will introduce each of these interactions in turn.

2.1.1 Exchange interaction

Ferromagnetism and antiferromagnetism are magnetic phenomena that are characterized by a spontaneous collective ordering of the magnetic moments in a material below a critical temperature. For ferromagnets, the moments order below a critical temperature called the Curie temperature T_{C}, while in antiferromagnets, magnetic ordering occurs below the Néel temperature T_{N}. Above their critical temperatures, the materials are paramagnetic.

The primary cause for collective magnetism in metals is the exchange interaction. It relies on the Pauli exclusion principle and the Coulomb interaction. Since electrons are fermions, the overall wavefunction of the system must be antisymmetric under the exchange of two electrons. Simply speaking, this means that two electrons of like spin cannot occupy the same state (Pauli exclusion principle). This implies that the single electron wavefunctions for electrons with same spin are spatially more distant from each other than for wavefunctions of electrons with opposite spin, leading to a reduction in electrostatic energy through the Coulomb interaction between the electrons.

The exchange interaction between spin pairs can be described by a Heisenberg Hamiltonian

$$H_{\mathrm{ex}} = -J \sum_{i,j}^{NN} \vec{S}_i \cdot \vec{S}_j. \tag{2.1}$$

Since the exchange interaction is short-ranged, the sum is taken over nearest neighbors only. $\vec{S}_i$ and $\vec{S}_j$ are usually classical spins, except for some calculations of critical properties. J denotes the exchange interaction constant

between nearest neighbors. For a positive J, all spins point in one direction in order to reach the minimum total energy. The ground state is therefore ferromagnetic, and a macroscopic magnetization can be detected (the magnetization is given by the sum (per unit volume) of all the magnetic moments $\vec{\mu} = -\mu_B g \vec{S}$). If J is negative, neighboring spins point in opposite directions and the ground state becomes antiferromagnetic. The macroscopic magnetization vanishes.

2.1.2 Dipolar interaction

The magnetic dipole-dipole interaction considers the fact that each spin has a magnetic moment causing a magnetic dipole field. Neighboring moments start to align along the field lines, creating a sample environment that favors an anti-parallel alignment of the moments. The dipolar interaction energy is given by

$$H_{\mathrm{dd}} = \frac{\Omega}{2} \sum_{i,j}^{N} \frac{1}{r_{ij}^3} \left(\vec{S}_i \cdot \vec{S}_j - 3 \frac{1}{r_{ij}^2} (\vec{S}_i \cdot \vec{r}_{ij})(\vec{S}_j \cdot \vec{r}_{ij}) \right). \tag{2.2}$$

The first part of the equation is minimized for spins pointing in opposite directions, thus favoring an antiferromagnetic coupling. The second part is minimized for spins that point along the direction of the vector between them. This agrees with the observation of magnetic poles at the ends of a bar magnet. The strength of the dipolar interaction drops off quickly (as $1/r^3$) but not as quickly as the exchange interaction. As a consequence, the dipolar interaction dominates at long distances.

The dipolar interaction can be associated with the so-called demagnetizing field since it opposes ferromagnetic ordering. Based on the geometry of the sample, a geometric factor, the demagnetization factor N can be introduced to relate the net magnetization of the sample to the demagnetizing field:

$$\vec{H}_d = -N\vec{M}. \tag{2.3}$$

N is a second rank tensor that is usually diagonalized by using the principal axes of an ellipsoid. For example, the components of the demagnetization factor for a sphere are $N_x = N_y = N_z = 1/3$, whereas for a flat plate, the components parallel and perpendicular to the surface become zero ($N_x = N_y = 0$) and 1 ($N_z = 1$), respectively.

The dipolar interaction can also explain the domain structure of ultrathin films. For a system with perpendicular magnetization, the second part of eq. 2.2 vanishes and the dipolar energy is effectively antiferromagnetic favoring the formation of striped domains. For in-plane magnetized films, the second part in eq. 2.2 dominates the dipolar interaction which becomes ferromagnetic in nature. Therefore, a single domain state is favored.

2.1.3 Magnetic anisotropies

The term *magnetic anisotropy* describes the fact that in solids, the magnetization is not isotropic but prefers to lie in particular crystallographic directions and in directions that are determined by the sample shape. These two contri-

butions to the anisotropy are called magnetocrystalline and shape anisotropies and will be treated in this section. Other contributions to the total anisotropy such as the magnetoelastic anisotropy that arises from mechanical strains in the material (especially in epitaxial structures such as ultrathin films) are neglected here because they depend on the specific material under study.

Magnetic anisotropy is described by the magnetic anisotropy energy density (MAE) which is the difference in free energy density for two directions of the magnetization in a sample. In general, the preferred direction of the magnetization for which the free energy density is minimized is called easy axis, while the least preferred direction is called hard axis.

Magnetocrystalline anisotropy

The microscopic origin of the magnetocrystalline anisotropy is the spin-orbit coupling

$$H_{\mathrm{LS}} = -\lambda \vec{L} \cdot \vec{S} \tag{2.4}$$

The orbital momentum $\vec{L}$ of the electrons in a solid is influenced by the crystal field from the lattice. Since the electron spin $\vec{S}$ couples to $\vec{L}$ and hence to the lattice, the crystal field has a direct influence on the magnetic anisotropy in the solid. The resulting anistropy energy density can be described phenomenologically by introducing an expression for the directional energy dependence of the magnetization in the lattice. There are many ways of approximating this energy depending on the crystal symmetry. In a cubic material, it is customary to express the energy in terms of the direction cosines α_i with respect

to the cubic axes. A more general treatment uses an expansion in spherical harmonics that reflect the underlying crystal symmetry.

For a cubic system such as Fe, the magnetocrystalline anisotropy free energy density can be shown to be:

$$f_c = \frac{F_c}{V} = K_1(\alpha_1^2\alpha_2^2 + \alpha_2^2\alpha_3^2 + \alpha_3^2\alpha_1^2), \tag{2.5}$$

where K_1 is an anisotropy constant. This can also be expressed in polar coordinates (with θ measured from (001) and ϕ measured from (100) in the xy plane) as

$$\begin{aligned} f_c = \frac{F_c}{V} &= K_1(\frac{1}{4}\sin^4\theta\sin^4\phi + \frac{1}{4}\cos^4\theta + \sin^4\theta\sin^2\phi\cos^2\phi \\ &\quad -\frac{1}{2}\sin^2\theta\cos^2\theta\sin^2\phi + \sin^2\theta\cos^2\theta\cos^2\phi). \end{aligned} \tag{2.6}$$

For the magnetization in the plane such as in the case of Fe/W(110), this simplifies to a uniaxial anisotropy

$$f_c(\theta = \pi/2, \phi) = \frac{K_1}{4}(\sin^2(2\phi) + \sin^4\phi). \tag{2.7}$$

Shape anisotropy

The second contribution to the MAE is the shape anisotropy that has its origin in the dipolar interaction. The energy density is in general given as

$$f_d = \frac{F_d}{V} = \frac{1}{2}\mu_0(\vec{M}N\vec{M}), \tag{2.8}$$

where N is the demagnetization tensor introduced before ($Tr(N) = 2N_{\|} + N_{\perp} = 1$). Using θ as the angle between the magnetization and the film normal

(as before), the energy density can be written as

$$f_d = \frac{F_d}{V} = \frac{1}{2}\mu_0 M^2 (N_{\|} \sin^2\theta + N_{\perp} \cos^2\theta). \tag{2.9}$$

Since for ultrathin films $N_{\|} = 0$ and $N_{\perp} = 1$, the shape anisotropy energy density becomes simply

$$f_d = \frac{F_d}{V} = \frac{1}{2}\mu_0 M^2 \cos^2\theta. \tag{2.10}$$

So far, only bulk anisotropies have been discussed. However, in ultrathin films, anisotropies arising from the local symmetry breaking at the surface of the film play a much bigger role than the contributions from the bulk. In the total MAE, this effect is taken into account by adding a surface anisotropy term that depends on the thickness of the film:

$$f_t = \frac{F_t}{V} = f_{\text{bulk}} + \frac{2 f_{surface}}{t}, \tag{2.11}$$

where

$$f_{\text{bulk}} = f_c + f_d \quad \text{and} \quad f_{\text{surface}} = \sigma_c. \tag{2.12}$$

t is the film thickness, f_{surface} is the surface anisotropy energy per unit area given by the surface magnetocrystalline anisotropy density (σ_c). The factor of two is due to the fact that there are two surfaces (the free surface of the film and the substrate-film interface). From eq. 2.11, it becomes obvious that for a very thin film, the surface anisotropy term dominates, while for a thicker film, the bulk anisotropies are more important. Furthermore, an interesting feature

in eq. 2.11 is that a spin reorientation is possible with increasing thickness of the film. This has been observed experimentally for several systems, for instance for Fe/Cu(001) [7], Co/AU(111) [8] and Fe/Ni/W(110) [9]. This phenomenon is due to the competition of the anisotropy terms. As can be seen from eq. 2.10, the shape anisotropy favors an easy axis in the film plane, whereas, depending upon the sign of the magnetocrystalline anisotropy, the total anisotropy may prefer an easy axis in the plane of the film or normal to it. The resulting easy axis of the system is therefore depending on the balance of the bulk (shape and magnetocrystalline) and surface (magnetocrystalline) anisotropy terms.

The MAE is strongly dependent on temperature. After a model by Callen and Callen [10], the anisotropy constants k_i should vanish at the Curie temperature with the magnetization

$$\frac{k_l(T)}{k_l(0)} = \left(\frac{M(T)}{M(0)}\right)^{l(l+1)/2} . \tag{2.13}$$

Here, the anisotropy constants were obtained from an expansion in spherical harmonics (so the k_i are different from the K_i introduced before), and l gives the order of the spherical harmonics (l=2 for uniaxial, l=4 for cubic symmetry, etc.). What is remarkable is the fact that the magnetic anisotropy should drop off faster with increasing temperature than the magnetization itself[1].

The MAE is by definition a macroscopic quantity, since it depends on the

[1]In fact, eq. 2.13 is for low temperatures only. For the high temperature regime, the anisotropy coefficients should vanish as $(M(T)/M(0))^l$ which is still faster than the disappearance of M at T_C.

orientation of the magnetization $\vec{M}$. Once the magnetization vanishes above T_C, the MAE disappears, but the underlaying microscopic anisotropies remain. Information about these anisotropies can be obtained by measurements of the magnetic ac susceptibility. This technique is introduced next.

2.2 The magnetic susceptibility

The magnetic susceptibility χ describes the change in magnetization $\vec{M}$ in response to an applied magnetic field $\vec{H}$

$$\vec{M} = \chi \vec{H}. \tag{2.14}$$

Strictly speaking, the susceptibility is the response to an infinitesimally small magnetic field. It can therefore be seen as the slope of the initial magnetization curve $M(H)$ at zero field. In experiments performed in this work, a small magnetic field amplitude of approximately 0.1 mT (=1 Oe) is applied, so that the susceptibility can be approximated by

$$\chi = \frac{\Delta M}{\Delta H}. \tag{2.15}$$

In general, the susceptibility is a second rank tensor with its components χ_{ij} given by

$$\chi_{ij} = \frac{\partial M_i}{\partial H_j} \quad \text{with} \quad i, j = x, y, z. \tag{2.16}$$

However, it is usually the diagonal terms that are measured experimentally as parallel and transverse (or perpendicular) susceptibilities with respect to the

magnetization direction. For example, consider a film with an in-plane easy axis of magnetization as shown in figure 2.1. Contributions to the parallel

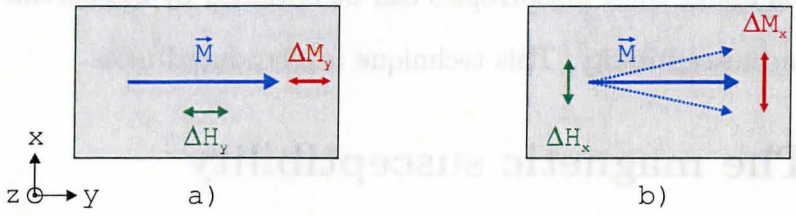

Figure 2.1: Definition of a) the parallel susceptibility $\chi_p = \frac{\Delta M_y}{\Delta H_y}$ and b) the transverse (or perpendicular) susceptibility $\chi_{t,x} = \frac{\Delta M_x}{\Delta H_x}$. The transverse susceptibility in z direction is not shown here.

susceptibility are expected when the amplitude of the magnetization changes, for example through critical fluctuations near T_C, through domain wall motion (averaged over several domains), or spin reversal. On the other hand, a transverse susceptibility is measured when the magnetization is "wiggled" out of its equilibrium position. This is used in anisotropy measurements, for example, where the reciprocal of the size of the susceptibility is a measure for the strength of the anisotropy. In particular, this means that when the anisotropy gets smaller, the magnetization is more easily tilted from its equilibrium axis and the susceptibility signal increases. These three processes that are giving rise to susceptibility signals are discussed in more detail in section 2.2.1.

In this thesis, the magnetic susceptibility is measured using an ac technique: A small ac modulated magnetic field of a chosen frequency is applied to the magnetization and the magnetic response parallel to the field is measured by dual-phase lock-in detection. By using the lock-in technique, the real

(in-phase) and imaginary ($\pi/2$ out-of-phase) components of the complex ac susceptibility are measured.

$$\chi = \chi' + i\chi'' \tag{2.17}$$

The lock-in amplifier has several purposes. First, it supplies the reference frequency ω of the modulating magnetic field $H(\omega) = H_0 \cos(\omega t)$. Furthermore, the lock-in amplifies the measured signal at its input (about 30 dB) and then performs a Fourier-transform "locking in" to the signal at the reference frequency. Finally, the Fourier-transformed signal is integrated with a fixed time constant (τ=1-2 s) acting as a low-pass filter, thereby reducing high-frequency noise. The susceptibility signal $\chi(\omega)$ can be expressed as [11]

$$\chi(\omega) = \frac{1}{H_0 \tau} \int_{-\infty}^{t} \exp(i\omega t') M(t') \exp(-(t')/\tau) \mathrm{d}t', \tag{2.18}$$

with $M(t')$ being the modulated magnetization at the lock-in amplifier input and H_0 being the amplitude of the applied magnetic field.

The origin of the real χ' (in-phase) and imaginary χ'' ($\pi/2$ out-of-phase) parts of the susceptibility can be discussed from the schematic magnetization curves shown in figure 2.2. In a paramagnetic material (fig. 2.2(a)), $\chi(\omega) \approx M(\omega)/H_0$. There is no remanent magnetization ($M(H{=}0){=}0$) and the magnetization is completely in-phase with the applied magnetic field. Thus only a real susceptibility signal is measured for a paramagnetic film. For ferromagnetic films such as shown in figures 2.2(b) and 2.2(c), the magnetization $M(t)$ is phase-shifted from $H(t)$. This means that the susceptibility has a

non-zero imaginary part which corresponds to the work done by the applied field over one cycle of the loop. This can be best seen in figure 2.2(c), where a magnetic film with large coercive field H_c has a very wide hysteresis loop. The $M(t)$ signal is shifted by almost $\pi/2$ with respect to $H(t)$, resulting in a large imaginary part χ''.

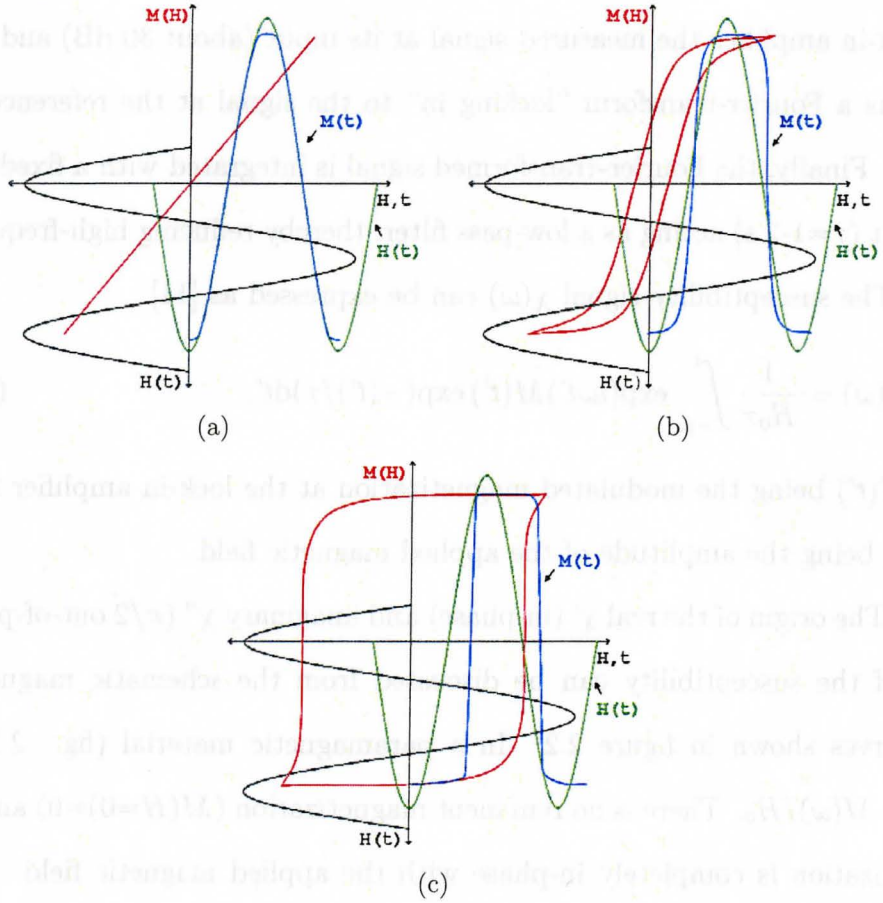

Figure 2.2: The $M(t)$ response for a paramagnet (a) is completely in-phase with $H(t)$, for a ferromagnet with small coercive field (b) $M(t)$ is slightly shifted, and for a ferromagnet with a very large coercive field (c), $M(t)$ is almost shifted by $\pi/2$.

2.2.1 Types of magnetic susceptibility signals

In general, there are three different processes that can give rise to a susceptibility signal.

The first is related to critical fluctuations that become relevant in vicinity of the Curie transition temperature T_C. Near T_C, the correlation length of the magnetization diverges to infinity causing large fluctuations in the magnetization of the film. The magnetic moments along the easy axis can easily be reversed by a very small field, resulting in a large real susceptibility response. In theory, the real component of the susceptibility diverges at T_C (for $T \rightarrow T_C^+$) according to a power law with the critical exponent γ:

$$\chi'(t) = \chi_0^+ t^{-\gamma}, \tag{2.19}$$

where χ_0 is the critical amplitude and t the reduced temperature

$$t = \frac{T - T_C}{T_C}. \tag{2.20}$$

However, in the experiment, a finite susceptibility is observed (see figure 2.3). The reason for this rounding of the real susceptibility peak are finite size effects. In particular, demagnetizing effects have to be taken into account. When applying an external magnetic field H_{ext} to the thin film, a demagnetizing field $H_d = -NM$ forms in the film (N is the demagnetization tensor introduced in section 2.1.3). The field internal to the film is then $H_{int} = H_{ext} + H_d$ resulting in the external measured susceptibility

$$\chi_{ext} = \left(\frac{1}{\chi_{int}} + N \right)^{-1}. \tag{2.21}$$

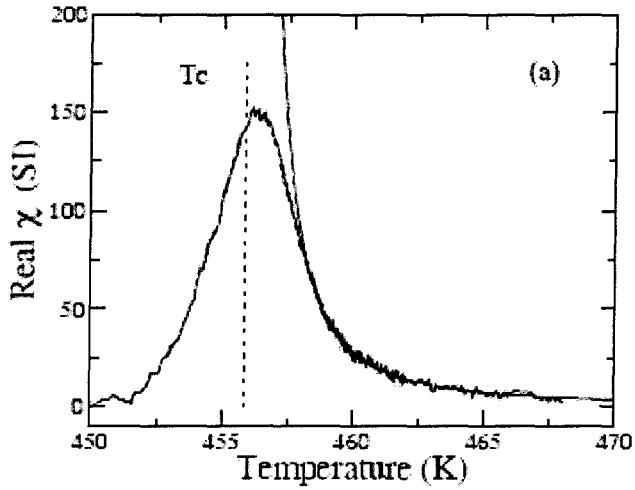

Figure 2.3: Finite real part of the susceptibility near the Curie transition measured from a 2 ML Fe/W(110) film. A power-law fit to eq. 2.19 is shown (taken from [12]).

This implies that the measured susceptibility for an in-plane film ($N = N_{\|}$) goes to $1/N$ at the Curie transition where χ_{int} is infinity. The value of N for in-plane magnetized films has been found to be proportional to the ratio of film thickness to the lateral dimension of the film [13], giving a small value of the order of 10^{-7}. This simple treatment has several shortcomings, namely that it neglects other effects (finite magnetic field, finite size of the sample, etc.) that contribute to the saturation of the measured χ. The value of N gives therefore, at best, an upper limit for the susceptibility peak.

The second process resulting in a magnetic susceptibility signal is related to perpendicularly magnetized films that exhibit a striped domain structure due to the competition between the dipole energy and the perpendicular surface anisotropy. This domain structure in perpendicular films is responsi-

ble for susceptibility signals that are much larger than expected by considering only the demagnetizing factor $N_\perp \approx 1$ in eq. 2.21. The susceptibility signal arises from a net moment along the direction of the applied field caused by the movement of magnetic domain walls, and by domain wall pinning and unpinning processes. All of these processes depend on temperature. For example, at low temperatures, the thermal energy of the domain walls is less than the pinning energy due to defects. This restricts the motion of the domain walls, and the susceptibility signal is small. As the temperature is increased, domain walls gain thermal energy and become unpinned. They can move, creating a net moment (averaged over several domains) along the field direction.

Compared to the previous two mechanisms for which the susceptibility is measured along the easy axis of the magnetization in the ferromagnetic film (parallel susceptibility see fig. 2.1), the susceptibility in the third mechanism is measured perpendicular to the magnetic easy axis, i.e. along a hard axis. By applying a magnetic field along the hard axis, a torque is exerted on the magnetic moments trying to rotate them in the direction of the applied field. This "wiggling" of the magnetic moments produces a small change in the magnetization along the hard axis, producing a small susceptiblity signal. The size of this measured susceptibility is a measure for the strength that keeps the magnetic moments aligned in the easy direction, which is the ferromagnetic anisotropy in the system.

2.2.2 Detection of antiferromagnetism

So far, the ac susceptibility of ferromagnetic ultrathin films has been treated. One goal of this thesis is the improvement of the sensitivity of the susceptibility measurements such that antiferromagnetism can be detected in ultrathin films. Besides the fact that ultrathin films yield only very small signals due to the small amount of magnetic film material, the main difficulty in the detection of antiferromagnetism results from a lack of macroscopic magnetism. For thicker films and multilayer stacked films, polarized neutron reflectometry (PNR) has been used to measure antiferromagnetic signals [4]. Antiferromagnetic ordering of the surface layer on ultrathin films has also been studied by spin-polarized scanning tunneling microscopy [5]. Using X-ray magnetic dichroism (XMCD), the interface exchange coupling between a ferromagnetic/antiferromagnetic (FM/AFM) bilayer system (Co/FeMn) has been used to gain insight on the structure of the antiferromagnetic layer [6].

The magnetic ac susceptibility is useful for studying antiferromagnetic ultrathin films in two ways: Qualitatively, the interface exchange coupling in a FM/AFM system can be used to extract magnetic properties such as the Néel temperature T_N, the orientation of easy and hard axes or even spin re-orientation transitions of the AFM. Quantitatively, the susceptibility of an antiferromagnetic film can be measured directly after polarizing the fluctuating moments in the two magnetic sublattices near T_N, creating a small net magnetic moment. In what follows, both methods will be described briefly.

AFM via exchange coupling at an AFM/FM interface

The interaction at the interface between AFM and FM ultrathin films offers a possibility to study antiferromagnetism in ultrathin films. The reason for this is that the AFM layer is exchange-coupled to the FM layer, an example of a very strong surface anisotropy. The FM layer then produces a susceptibility signal due to changes in its FM magnetic moment. An externally applied magnetic field then can couple indirectly to the AFM through the FM layer. In particular, the exchange interaction influences the magnetization curves of an FM/AFM coupled system, inducing a uniaxial anisotropy for the system below the critical temperature of the antiferromagnetic layer T_N. Macroscopically, this phenomenon is observed as a shift in the hysteresis curve from the origin along the applied field axis. This shift is commonly referred to as *exchange bias*. The spin configurations in a FM/AFM bilayer and the creation of the exchange bias are shown schematically in figure 2.4.

When the AFM/FM bilayer is cooled in the temperature range from $T_N < T < T_C$ in an external field, the FM spins align with the field. For $T < T_N$, the AFM spins next to the FM spins will align either ferromagnetically or antiferromagnetically with the FM spins because of the exchange coupling at the interface. Removing the external field traps the system in a metastable state, pinning the AFM spins and thus creating an effective anisotropy for the ferromagnet through the exchange interaction. This means that if a transverse magnetic field is applied to the system, the pinned AFM spins at the interface

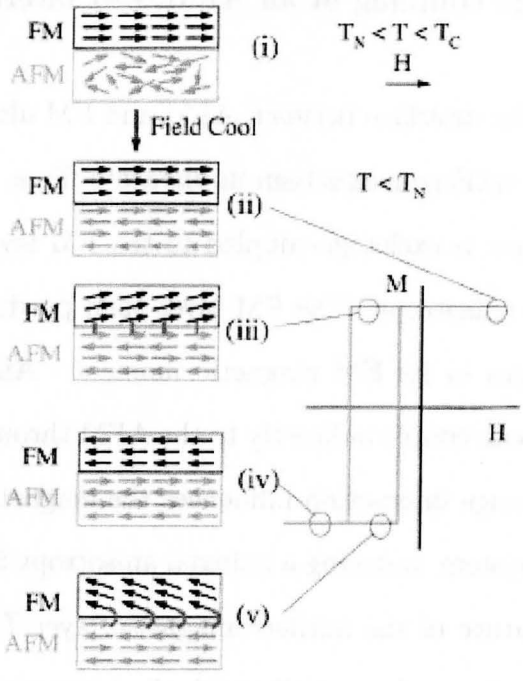

Figure 2.4: Schematic diagram illustrating the spin configuration in a FM/AFM bilayer (taken from [14]).

will exert a microscopic torque on the FM spins to keep them aligned in their original direction.

The exchange induced magnetic anisotropy can be measured by the transverse susceptibility, even without biasing the system in an external magnetic field [15]. The anisotropy is probed by measuring how difficult it is to "wiggle" the FM moments by applying a small ac magnetic field (on the order of Oersteds). Upon increasing the temperature from below T_N, two distinct peaks in the imaginary part of the transverse susceptibility appear, corresponding to the blocking temperature T_B (where the FM spins are no longer

pinned by the AFM) and to the Néel temperature T_N where the alignment of the AFM moments disappears. Here, it is the imaginary part of the susceptibility that contains the relevant information as it gives the dissipative response of the system relaxing toward equilibrium as the temperature is increased.

Direct measurement of the AFM susceptibility

The direct observation of the susceptibility in antiferromagnetic ultrathin films is a more challenging problem since there is, on average, no magnetic moment near T_N that the magnetic field could couple to. To our knowledge, it has not yet been accomplished. The role of the ac magnetic field in this case is not only to probe the magnetization but also to induce a magnetic moment in the first place, by polarizing the fluctuating moments in the two sublattices of the AFM near T_N. It is this small net magnetic moment that might be detected by the ac susceptibility. The shape of the susceptibility of an AFM should be different from that of FM materials, displaying a rather broad peak at T_N and a characteristic shape below T_N, depending on the orientation of the field with respect to the AFM easy axis (see figure 2.5).

According to van Vleck [16], the susceptibility below T_N along the hard axis of the antiferromagnet stays roughly constant with decreasing temperature, while it decreases with decreasing temperature along the easy axis. This feature of the susceptibility is shown in figure 2.5(a) for measurements of a Cr_2O_3 single crystal.

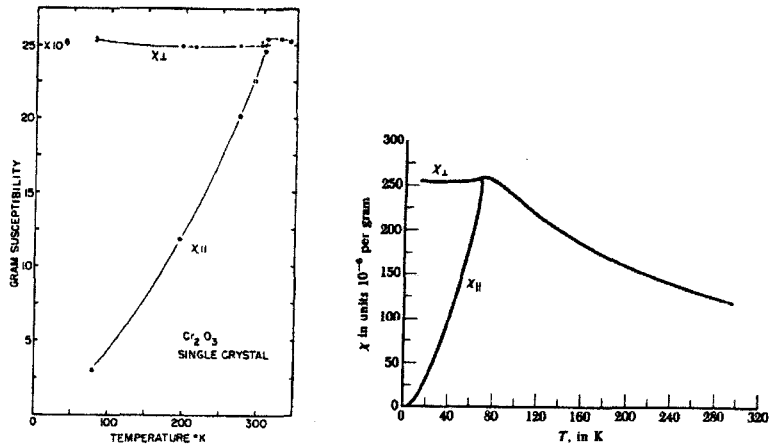

(a) (b)

Figure 2.5: Dc susceptibility measurements on 2.5(a) Cr_2O_3 along the easy ($\chi_\parallel$) and hard ($\chi_\perp$) crystallographic axes [17]. In 2.5(b), the parallel and perpendicular dc susceptibility for MnF_2 is shown, illustrating the broad peak at the Néel temperature [18].

2.3 The surface magneto-optic Kerr effect

The susceptibility measurements performed in this thesis rely on the surface magneto-optic Kerr effect (SMOKE). For this reason, a detailed discussion of the physical origin and the experimental manifestations of SMOKE will be given in this section.

Unlike some other magneto-optic effects that are quadratic in the magnetization (for example, the Voigt effect), SMOKE has the advantage of producing an optical signal (a polarization rotation) that is directly proportional to the magnetization. Therefore, it can be exploited as a tool to measure the

ac magnetic susceptibility

$$\chi \propto \frac{\Phi_K}{H}, \tag{2.22}$$

where Φ_K is the complex Kerr rotation and H the (small) applied field.

SMOKE has first been used for the investigation of magnetism in thin films and ultrathin films in 1985 [19] and has since become one of the most popular techniques in the field of surface magnetism. It has also made a large impact on data storage technology where it is employed as readout mechanism in magneto-optical disk drives [20]. The main disadvantage of SMOKE lies in the fact that it does not yield measurements in absolute magnetic units but rather in units of polarization rotation (on the order of 10^{-6} radians for ultrathin films). Nevertheless, through a careful optical calibration an approximate magnetic calibration is possible (see Chapter 3.3.1).

2.3.1 Introduction

The surface magneto-optical Kerr effect is characterized by a complex rotation of the plane of polarization of linearly polarized light upon reflection from a magnetic surface.

To illustrate how this rotation arises, consider the electric field vector of an electromagnetic wave that propagates in z-direction with wave number k and frequency ω:

$$\vec{E}(\vec{r},t) = Re\left(e^{i(\omega t - kz)}\begin{pmatrix} E_{0,x} \\ E_{0,y} \\ 0 \end{pmatrix}\right). \tag{2.23}$$

Here, $E_{0,x} = |E_{0,x}|\, e^{i\delta_x}$ and $E_{0,y} = |E_{0,y}|\, e^{i\delta_y}$ (δ being a phase angle) represent the complex field amplitudes whose ratio $E_{0,y}/E_{0,x}$ defines the polarization state of the wave. This ratio can be expressed in terms of two angles characterizing an ellipse, the azimuthal angle θ (orientation of the ellipse's major axis) and the ellipticity angle η (minor axis/major axis) (see figure 2.6):

$$\frac{E_{0,y}}{E_{0,x}} = \frac{\tan\theta + i\tan\eta}{1 - i\tan\theta\tan\eta}. \tag{2.24}$$

If $E_{0,x}$ and $E_{0,y}$ have the same complex phase δ, eq. 2.24 gives a linear polarization state with azimuthal angle $\theta = \tan^{-1}(E_{0,y}/E_{0,x})$. This means that the direction of the wave $\vec{E}_k$ remains constant in time (apart from a minus sign). A relative phase $\Delta\delta$ between $E_{0,x}$ and $E_{0,y}$ causes the wave to rotate with time, tracing out an ellipse. This is incorporated into eq. 2.24 by the ellipticity $\eta = \tan^{-1}(b/a)$, with a and b denoting the major and minor axes of the ellipse, respectively.

In general, the Kerr effect is very small ($\approx 10^{-4}$-10^{-6} radians). This justifies the approximation of eq. 2.24 by

$$\frac{E_{0,y}}{E_{0,x}} \approx \theta + i\eta, \tag{2.25}$$

giving

$$\theta \approx Re\left(\frac{E_{0,y}}{E_{0,x}}\right) \quad \text{and} \quad \eta \approx Im\left(\frac{E_{0,y}}{E_{0,x}}\right). \tag{2.26}$$

The angles θ and η can also be expressed by the components of the Fresnel reflection matrix that refer to the usual standard polarization directions with

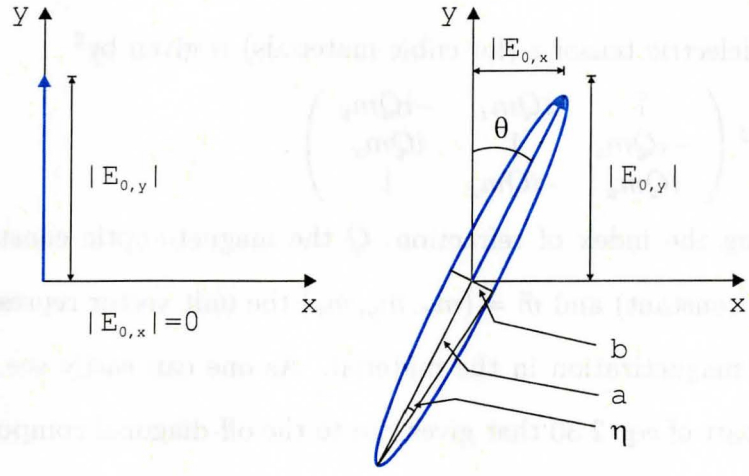

Figure 2.6: Initially linearly polarized light along the y axis (left) is reflected into an elliptical polarization state (right) characterized by an azimuthal angle θ from the y axis and an ellipticity $\eta = \tan^{-1}(b/a)$.

respect to the plane of incidence of the wave, perpendicular (s) or parallel (p).

$$R = \begin{pmatrix} r_{ss} & r_{sp} \\ r_{ps} & r_{pp} \end{pmatrix} \tag{2.27}$$

For s-polarized light, one therefore gets

$$\theta \approx Re\left(\frac{r_{ps}}{r_{ss}}\right) \quad \text{and} \quad \eta \approx Im\left(\frac{r_{ps}}{r_{ss}}\right), \tag{2.28}$$

whereas for p-polarized light, the azimuth and ellipticity become

$$\theta \approx Re\left(\frac{r_{sp}}{r_{pp}}\right) \quad \text{and} \quad \eta \approx Im\left(\frac{r_{sp}}{r_{pp}}\right). \tag{2.29}$$

The components of R are related to the dielectric properties of the material via the boundary conditions of the Maxwell equations at the surface of the material (see section 2.3.3). In particular, the dielectric displacement is given by

$$\vec{D} = \epsilon\vec{E} = N^2(\vec{E} + i\vec{E} \times Q\vec{m}), \tag{2.30}$$

where the dielectric tensor ϵ (for cubic materials) is given by[2]

$$\epsilon = N^2 \begin{pmatrix} 1 & iQm_z & -iQm_y \\ -iQm_z & 1 & iQm_x \\ iQm_y & -iQm_x & 1 \end{pmatrix}, \tag{2.31}$$

with N being the index of refraction, Q the magneto-optic constant (often called Voigt constant) and $\vec{m} = (m_x, m_y, m_z)$ the unit vector representing the direction of magnetization in the material. As one can easily see, it is only the second part of eq. 2.30 that gives rise to the off-diagonal components of ϵ, and hence to SMOKE.

So far, only a phenomenological description of SMOKE has been given. In the next sections, the physical origin of the Kerr effect is explored and a macroscopic formalism to describe the experimentally accessible quantities is presented for arbitrary magnetization directions and film configurations.

2.3.2 Microscopic approach

The magneto-optic Kerr effect is a quantum mechanical effect as the electrical field of the light is coupled to the electron spin in the magnetic material through the spin-orbit interaction. Simply speaking, the SMOKE rotation arises from the different response of the electrons (with spin) to the polarization of the photons. One major requirement for the Kerr effect to be observable is set by the necessary energy range of the photons, i.e. the wavelength of the laser light. Only photons with energies in the same range as the energy difference between the valence and conduction bands can promote electrons from

[2]Here, ϵ is given to first order in the magnetization only. Second order effects become important in the Voigt effect, but are neglected in the treatment of SMOKE here.

one state to the other. In this work, this requirement is met by using a HeNe laser (632.8 nm) emitting photons with an energy of 1.96 eV.

The anisotropic dielectric tensor ϵ (eq. 2.31) can be related to optical interband transitions through the the optical conductivity tensor σ. Its off-diagonal elements σ_{xy} are given by the difference in transition probabilities for right and left circularly polarized light[3] using Fermi's golden rule [52]:

$$\sigma_{xy} \propto \sum_{i,f} \left(|\langle i| p_r |f\rangle|^2 - |\langle i| p_l |f\rangle|^2 \right). \tag{2.32}$$

Here, i and f refer to the initial and final electronic states, p_r and p_l are the electric dipole moments for right and left circularly polarized light. The allowed transitions between electronic states i and f (labeled in standard notation according to band index n, quantum numbers l and m_l and spin$\uparrow$ or spin$\downarrow$) are determined by the dipole selection rules:

$$\Delta l = \pm 1, \quad \Delta m_l = \pm 1. \tag{2.33}$$

For transition metals, the first selection rule implies that only transitions between p and d levels or s and p levels are allowed. The second rule refers to transitions induced by right ($\Delta m_l = -1$) and left ($\Delta m_l = +1$) circularly polarized light.

As an example for electric dipole transitions in a $3d$ transition metal ferromagnet such as iron, consider the transition between the two doubly degener-

[3]Obviously, linearly polarized light is obtained as a superposition of right and left circularly polarized modes.

ate $d_{xz}^{\uparrow,\downarrow}$, $d_{yz}^{\uparrow,\downarrow}$ energy levels (with $l = 2, m_l = \pm 1$) and a $p_z^{\uparrow,\downarrow}$ level ($l = 1, m_l = 0$) shown in figure 2.7.

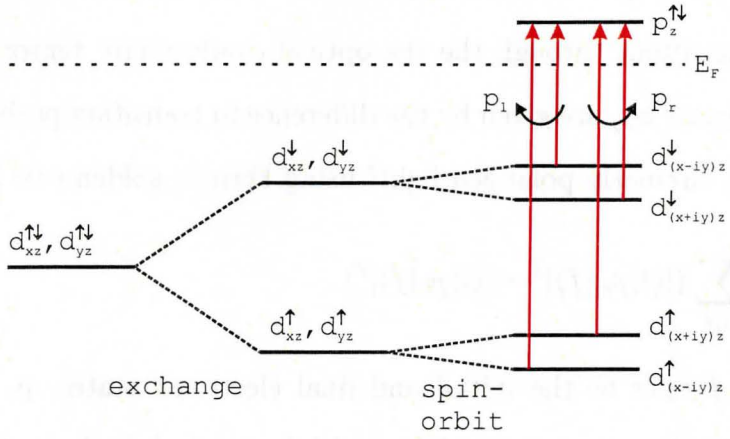

Figure 2.7: Energy levels in a 3d ferromagnet, showing electric dipolar transitions between d and p states, induced by right (p_r) and left (p_l) circularly polarized light.

Due to the exchange interaction, the d levels are split into majority (spin$\uparrow$) and minority (spin$\downarrow$) spin levels. Furthermore, as shown in the figure, the orbital degeneracy of the $d_{xz}^{\uparrow,\downarrow}$, $d_{yz}^{\uparrow,\downarrow}$ levels is lifted due to spin-orbit coupling. The levels are split into $d_{(x+iy)z}^{\uparrow,\downarrow}$ (with $m_l = +1$) and $d_{(x-iy)z}^{\uparrow,\downarrow}$ (with $m_l = -1$) levels. The transitions induced by right (p_r with $\Delta m = -1$) and left (p_l with $\Delta m = +1$) circularly polarized photons occur now from these spin- and spin-orbit split $3d$ levels to a $4p$ level by satisfying both selection rules. The first rule is satisfied by the initial state having $l = 2$ and the final state having $l = 1$, whereas the second rule is satisfied by promoting electrons in a $m = +1$ or $m = -1$ state to a state with $m = 0$. Looking at the right side of figure 2.7, it becomes clear that the transition probability for right and left circularly

polarized photons is different - it is this difference that gives rise to small changes in the polarization state of the reflected light, i.e. the Kerr effect.

For comparison, consider a paramagnet in which only the spin-orbit splitting is present. The $d^{\uparrow,\downarrow}_{xz}$, $d^{\uparrow,\downarrow}_{yz}$ split up in a higher energy level with $d^{\uparrow}_{(x+iy)z}$ and $d^{\downarrow}_{(x-iy)z}$ and a lower level with $d^{\uparrow}_{(x-iy)z}$ and $d^{\downarrow}_{(x+iy)z}$. Since the transition matrix elements for spin$\uparrow$ and spin$\downarrow$ contributions cancel (see eq. 2.34), there will be no change in polarization state and hence no Kerr effect.

$$\begin{aligned} |\langle i\uparrow|p_r|f\uparrow\rangle| &= |\langle i\downarrow|p_l|f\downarrow\rangle| \\ |\langle i\uparrow|p_l|f\uparrow\rangle| &= |\langle i\downarrow|p_r|f\downarrow\rangle| \end{aligned} \tag{2.34}$$

While several detailed microscopic calculations can be found in the literature for the magneto-optic Kerr effect for bulk ferromagnets or thicker multilayers [21–23], calculations for ultrathin films are extremely uncommon. However, it has been found that a macroscopic formalism [24] offers a quite satisfying description of the magnet-optic Kerr effect in ultrathin films.

2.3.3 Macroscopic formalism of SMOKE

A formalism to derive the magneto-optic coefficients ($r_{sp,ps,ss,pp}$) has been proposed in 1990 by Zak *et al.* [24,25] based on the macroscopic phenomenological picture introduced in section 2.3.1. Zak and coworkers express the reflection and transmission matrices[4] by means of universal medium boundary and propagation matrices. Within this framework, arbitrary magnetization directions

[4]So this approach is equally useful for the description of the Faraday effect where the change in polarization state arises from light transmitted through a magnetic medium.

and arbitrary film configurations can be treated on the same footing. The application to ultrathin films is a special case of this formalism and will be described later in this section.

Usually, three distinct configurations for the direction of the magnetization $\vec{M}$ with respect to the plane of incidence of the electromagnetic wave (propagating with wave vector $\vec{k}$) and the plane of the film are used in both theory and experiment because of simplifications in the expressions for θ and η. These geometries are depicted in figure 2.8.

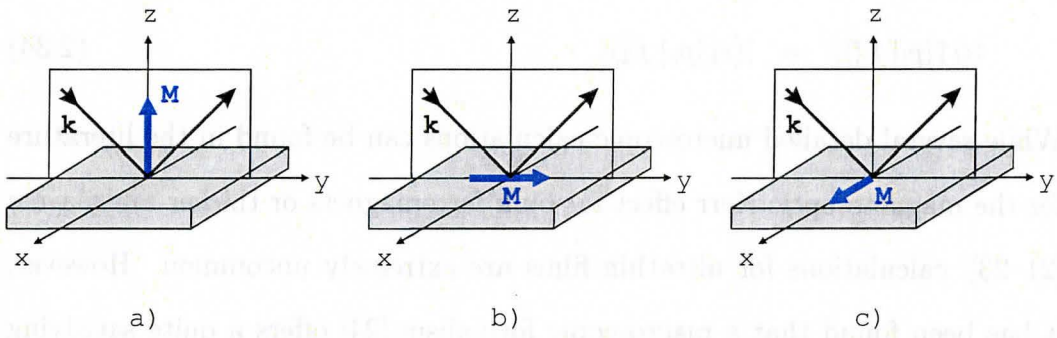

Figure 2.8: Different SMOKE geometries: a) - polar, b) - longitudinal, c) - transverse

In the polar geometry, the magnetization $\vec{M}$ is directed perpendicular to the film surface and lies in the plane of incidence of the light. As can be seen from the cross product in eq. 2.30, a SMOKE rotation can be observed for both polarization directions of the incident light (parallel and perpendicular to the plane of incidence). The polar effect is strongest for normal incidence at which the component of $\vec{E}$ perpendicular to $\vec{M}$ is largest.

The longitudinal geometry describes a situation in which the magnetization $\vec{M}$ lies parallel to both the film plane and the plane of incidence. The

Kerr signal depends on the angle of incidence (from the normal) and is largest for grazing incidence. The effect can be observed for s- or p-polarized incident light.

The transverse geometry is characterized by a magnetization $\vec{M}$ that lies parallel to the film plane but perpendicular to the plane of incidence. Consequently, no Kerr signal will arise from s-polarized light since it is parallel to $\vec{M}$. Only p-polarized light will result in a Kerr signal, however, it will not be given by a rotation of the polarization state but rather by a change in amplitude of the reflected wave. Because of the experimental apparatus and the detection method used in this thesis, this effect is especially hard to detect (see chapter 3.3.1). As in the case of the longitudinal Kerr effect, the transverse effect is largest for grazing incidence.

For an arbitrary magnetization direction, a superposition of the magneto-optic coefficients from the different geometries is expected. It is therefore convenient to choose an experimental geometry that allows for the either longitudinal or polar Kerr effect measurements.

Following the treatment by Zak *et al.*, the starting point for the calculation of the magneto-optic coefficients is the dielectric tensor ϵ (taken from eq. 2.31) describing the medium with an arbitrary magnetization direction with respect to the plane of incidence (yz) and the film plane (xy):

$$\epsilon = N^2 \begin{pmatrix} 1 & iQ\cos\varphi & -iQ\sin\gamma\sin\varphi \\ -iQ\cos\varphi & 1 & iQ\cos\gamma\sin\varphi \\ iQ\sin\gamma\sin\varphi & -iQ\cos\gamma\sin\varphi & 1 \end{pmatrix}, \qquad (2.35)$$

where the magnetization vector $\vec{M}$ is specified in polar coordinates:

$$\begin{aligned} M_x &= M \sin\varphi \cos\gamma, \\ M_y &= M \sin\varphi \sin\gamma, \\ M_z &= M \cos\varphi. \end{aligned} \tag{2.36}$$

Following this, the medium boundary matrix A for an incoming wave with wave vector $\vec{k}$ is calculated from the boundary conditions for $\vec{E}$ and $\vec{H}$ at the surface imposed by Maxwell's equations. To that end, two vectors are introduced that incorporate a) the tangential components of the electric and magnetic fields (the xy plane is the film plane) and b) the two orthogonal polarization states s and p (perpendicular and parallel with respect to the plane of incidence (yz)) for the incident and reflected waves:

$$\vec{F} = \begin{pmatrix} E_x \\ E_y \\ H_x \\ H_y \end{pmatrix}, \quad \text{and} \quad \vec{P} = \begin{pmatrix} E_s^i \\ E_p^i \\ E_s^r \\ E_p^r \end{pmatrix}. \tag{2.37}$$

These two vectors are connected through the medium boundary matrix A:

$$\vec{F} = A\vec{P}. \tag{2.38}$$

Knowing A, however, only gives a solution for a single boundary between two media. If one has a multilayer system or an ultrathin film in which the substrate also plays a role for the magneto-optic coefficients because of the larger penetration depth of the light wave with respect to the film thickness, the propagation of the wave in the material has to be considered. This is

achieved by introducing a medium propagation matrix labeled D (not to be confused with the dielectric displacement vector $\vec{D}$). Finally, to solve for the incident and reflected polarization vectors in the initial (i) and final (f) medium for the general multilayer case (k films in the stack), one has:

$$A_i \vec{P}_i = \prod_l^k (A_l D_l A_l^{-1}) A_f \vec{P}_f, \tag{2.39}$$

or in a more convenient way:

$$\vec{P}_i = M \vec{P}_f, \tag{2.40}$$

where the matrix M is given by:

$$M = A_i^{-1} \prod_l A_l D_l A_l^{-1} A_f = \begin{pmatrix} G & H \\ I & J \end{pmatrix}. \tag{2.41}$$

M is a 4×4 matrix that can be divided in four 2×2 matrices two of which have been shown to give the magneto-optic (or Fresnel) coefficients r_{sp}, r_{ps}, r_{ss} and r_{pp} [25]:

$$G^{-1} = \begin{pmatrix} t_{ss} & t_{sp} \\ t_{ps} & t_{pp} \end{pmatrix} \quad \text{and} \quad IG^{-1} = \begin{pmatrix} r_{ss} & r_{sp} \\ r_{ps} & r_{pp} \end{pmatrix}. \tag{2.42}$$

Once having the components of IG^{-1}, the Kerr angle θ and the Kerr ellipticity η for s- and p-polarized light can in principle be obtained using eq. 2.29.

What makes this approach complicated is the involved calculation effort for the medium boundary and propagation matrices and the computation of M. Nevertheless, this formalism is very powerful to describe basically every possible experimental configuration. In what follows, the magneto-optic coefficients and expected signal sizes for the setup used in this thesis are calculated.

2.3.4 SMOKE in ultrathin films - Estimation of signal sizes

In this section, the formalism introduced above is applied to ultrathin films and to the experimental setup used in this thesis. Theoretically expected SMOKE signals for ferromagnetic Fe/W(110) and Co/W(110) are calculated. The Fe/W(110) system has been of interest in the past as a 2-dimensional Ising model system for which the susceptibility at the Curie transition has been studied [26]. In this thesis, the system is investigated using the transverse susceptibility to gain insight on the ferromagnetic anisotropies and the magnitude of the involved susceptibility signals. The SMOKE size for Co/W(110) is calculated in this section mainly for comparison with other work on Co/Cu.

In the SMOKE formalism, the system considered in this thesis consists of a 3 media (vacuum, magnetic film, substrate), 2 boundary (vacuum-magnetic film, magnetic film-substrate) system. At first consider the general medium boundary matrix [24]:

$$A=\begin{pmatrix} 1 & 0 & 1 & 0 \\ \frac{i\alpha_y}{2\alpha_z}Q(\alpha_y g_i - 2\sin\varphi\sin\gamma) & \alpha_z + i\alpha_y\sin\varphi\cos\gamma Q & -\frac{i\alpha_y}{2\alpha_z}Q(\alpha_y g_r - 2\sin\varphi\sin\gamma) & -\alpha_z + i\alpha_y\sin\varphi\cos\gamma Q \\ \frac{i}{2}Ng_iQ & -N & \frac{i}{2}Ng_rQ & -N \\ N\alpha_z & \frac{iN}{2\alpha_z}g_iQ & -N\alpha_z & -\frac{iN}{2\alpha}g_rQ \end{pmatrix} \tag{2.43}$$

In the expression above, $\alpha_z = \cos\vartheta$ and $\alpha_y = \sin\vartheta$, with θ being measured from the vertical (z) axis; $g_i = \alpha_z\cos\varphi + \alpha_y\sin\varphi\sin\gamma$, $g_r = -\alpha_z\cos\varphi + \alpha_y\sin\varphi\sin\gamma$. The angles φ, γ have been defined before (eq. 2.35), N is the refractive index and Q the magneto-optic constant of the medium. Obviously,

when considering special cases such as a non-magnetic medium ($Q = 0$) or a magnetization pointing along a certain axis (polar: $\varphi = 0$, longitudinal: $\varphi = \pi/2, \gamma = \pi/2$ and transverse: $\varphi = \pi/2, \gamma = 0$), the expressions in A simplify considerably.

For the calculation of M, the medium propagation matrix D is also needed:

$$D = \begin{pmatrix} U & U\delta_i & 0 & 0 \\ -U\delta_i & U & 0 & 0 \\ 0 & 0 & U^{-1} & -U^{-1}\delta_r \\ 0 & 0 & U^{-1}\delta_r & U^{-1} \end{pmatrix}, \tag{2.44}$$

where g_i and g_r are given above.

$$\begin{aligned} U &= \exp(-ikNd\alpha_z), \\ \delta_i &= \frac{k}{2} NdQ \frac{g_i}{\alpha_z}, \\ \delta_r &= \frac{k}{2} NdQ \frac{g_r}{\alpha_z}. \end{aligned} \tag{2.45}$$

Here, d is the thickness of the medium and $k = 2\pi/\lambda$ the wavenumber of the incident wave. Upon consideration of the ultrathin film limit condition which is fulfilled for

$$\frac{2\pi}{\lambda} \sum_l d_l \, |N_l| \ll 1, \tag{2.46}$$

where the sum is taken over all magnetic films in the system, the expressions in D can be simplified by expanding U to first order in d: $(U \approx 1 - ikNd\alpha_z)$.

Finally, the magneto-optic coefficients can be calculated from eq. 2.41 and 2.42. In the case of a single ultrathin film on a non-magnetic substrate

investigated in this thesis, eq. 2.41 becomes

$$M = A_i^{-1} A_m D_m A_m^{-1} A_f, \tag{2.47}$$

with A_i being the medium boundary matrix for vacuum ($N = 1, Q = 0$), A_f being the matrix for the non-magnetic tungsten substrate ($N = N_s$ and $Q = 0$). A_m is the matrix for the magnetic film (with N and Q). The magneto-optic coefficients are obtained as

$$r_{ss} = \frac{1 - N_s}{1 + N_s} \tag{2.48}$$

$$r_{pp} = \frac{N_s - 1}{N_s + 1} \tag{2.49}$$

$$r_{ps} = -\frac{2k \cos\vartheta (\cos\vartheta d N^2 Q \cos\varphi - N_s \sin\vartheta d Q \sin\varphi)}{(\cos\vartheta + N_s \cos\vartheta)^2} \tag{2.50}$$

$$r_{sp} = -\frac{2k \cos\vartheta (\cos\vartheta d N^2 Q \cos\varphi + N_s \sin\vartheta d Q \sin\varphi)}{(\cos\vartheta + N_s \cos\vartheta)^2}. \tag{2.51}$$

Here, ϑ is the angle of incidence of the light and φ is the angle by which the magnetization is tilted from the normal in the yz plane. The reflectivities r_{ss} and r_{pp} were calculated to zeroth order in d. As one can see from eqs. 2.50 and 2.51, the coefficients r_{ps} and r_{sp} are a result of a superposition of the polar and the longitudinal effect[5]. The complex Kerr rotation for s- and p-polarized light is then given by

$$\Phi_s = \theta_s + i\eta_s = \frac{r_{ps}}{r_{ss}} \quad \text{and} \quad \Phi_p = \theta_p + i\eta_p = \frac{r_{sp}}{r_{pp}}. \tag{2.52}$$

[5]In the ultrathin film approximation, there is no contribution to the Kerr signal from the transverse effect. This makes sense since the transverse Kerr effect arises from the coefficients r_{ss} and r_{pp} ($r_{sp} = r_{ps} = 0$) which are only related to the index of refraction of the substrate and the initial medium, i.e. vacuum. The small thickness of the film will barely have an influence on the reflectivity of the substrate, hence there will be no observation of a transverse SMOKE.

In particular, the complex Kerr rotation in the polar case ($\varphi = 0$) simplifies to

$$\Phi_s = -\Phi_p = -\frac{2kdQN^2}{1 - N_s^2}, \tag{2.53}$$

while for the longitudinal case ($\varphi = 90°$) it becomes:

$$\Phi_s = \Phi_p = \frac{2kdQN_s}{1 - N_s^2} \tan\vartheta. \tag{2.54}$$

With the expressions above, the theoretically expected SMOKE signal sizes can be estimated. The incident angle for the used HeNe laser light ($\lambda = 632.8$ nm) is $\vartheta = 45°$ for the setup used in this thesis. This geometry results from constraints relating to the setup of the UHV chamber (UHV windows are at oriented at $\vartheta = 45°$ to the vertical). The index of refraction of the tungsten substrate at 632.8 nm is $N_W = 3.65 + i2.92$ [11]. For iron, $N_{Fe} = 2.87 + i3.36$ and $Q_{Fe} = 0.0376 + i0.0066$ [25] is used. For comparison, cobalt has a reflection index of $N_{Co} = 2.25 + i4.07$ and a magneto-optic constant of $Q_{Co} = 0.043 + i0.007$ [27].

	Fe/W(110)	Co/W(110)
long. Φ (μrad/ML)	$-39 + i24$	$-32 + i20$
long. $\lvert\Phi\rvert$ (μrad/ML)	46	37
polar Φ (μrad/ML)	$167 + i93$	$108 + i135$
polar $\lvert\Phi\rvert$ (μrad/ML)	191	173

Table 2.1: Expected Kerr rotation for Fe/W(110) and Co/W(110)

The values given in table 2.1 give an estimate for the size of the experimentally expected signals. However, since the values for refractive indices

and the magneto-optic constant Q have been obtained under different experimental conditions, for instance from thicker films or polycrystalline materials, deviations from the above values are expected and have indeed been observed. For example, for Fe/W(110), a longitudinal signal of 250 μrad/ML has been observed previously [11] and is used for the magnetic calibration of the susceptibility signals (see eq. 3.16).

As one can see in table 2.1, the polar signals are about 4-5 times larger than the longitudinal signals (for Fe/W(110) $|\Phi_{\mathrm{pol}}|/|\Phi_{\mathrm{long}}| \approx 4.2$). For the experiment on in-plane magnetized films this means that already a small tilt of the magnetization out of the film plane suffices to produce a polar signal. Furthermore, the calibration to magnetic units has to take into account these two different geometries when comparing signal sizes.

Upon comparison of measured rotations with those shown in table 2.1, it has been found that the calculated values are smaller than the observed ones. This is attributed to the fact that in ultrathin films, the measured signal does not originate exclusively from the Kerr effect but from a superposition of both Kerr and Faraday effects[6].

[6]Since the penetration depth of visible laser light into metals is much larger (> 20 nm [3]) than the thickness of the magnetic films ($\approx 0.2 - 1$ nm), the beam is passing through the film, is reflected from the metallic substrate and is transmitted back through the film causing a Faraday rotation. The detected signals are thus a combination of both Kerr and Faraday signals.

2.4 Estimates of antiferromagnetic susceptibility signals

In this section, admittedly rough estimates for the expected sizes of antiferromagnetic ac susceptibility signals will be given based on past experiments and on the above calculated and experimentally observed sizes of the complex Kerr rotations. The two approaches for the detection of antiferromagnetism via ac susceptibility measurements introduced in section 2.2.2 will be used as basis for the calculations.

In the method based on the exchange coupled FM/AFM bilayers, recent work [15] has provided susceptibility signals for the Co/CoO bilayer system as shown in figure 2.9.

From the graph, choosing a peak rotation of the imaginary part of the susceptibility (χ'') for a roughly 8 nm Co/4-10 nm CoO bilayer gives a value of about -0.2 mrad/Oe[7]. Assuming a saturation magnetization of Co/W(110) corresponding to the complex Kerr rotation of 37 μrad/ML in the longitudinal configuration calculated in table 2.1, the transverse susceptibility signal expected for the 32 ML thick (8 nm/(2.5 Å/ML)=32 ML) AFM exchange

[7]This thickness range of the CoO layer is mainly chosen because for 4 and 10 nm, the peak susceptibility value stays constant. Also, T_B (the lower peak at around 80 K) can be clearly observed, while for the biggest susceptibility peak of the thinnest CoO layer, the blocking temperature cannot be extracted from the curve. This suggests that if the AFM layer is much thinner than the FM layer, it cannot pin the FM spins effectively. Another possibility is the influence of finite size effects in the AFM layer, which have been observed in films of $\leq$10 Å in thickness [28].

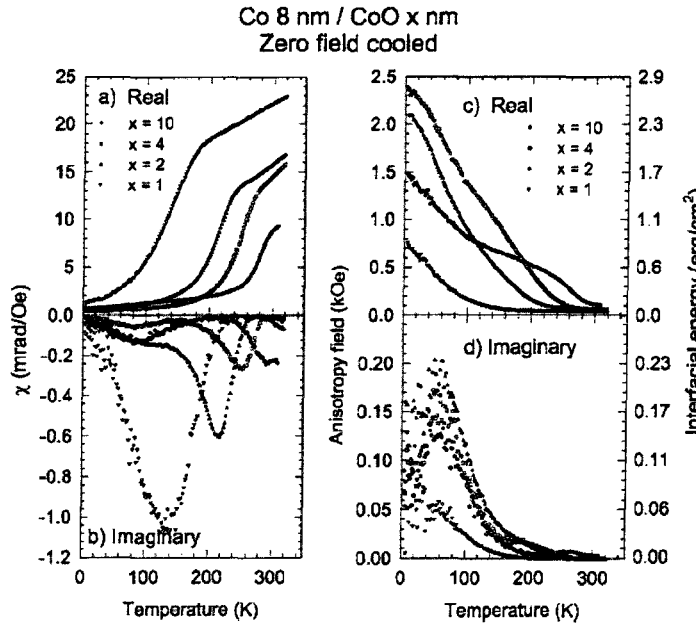

Figure 2.9: Left: Transverse susceptibility measurements on a Co/CoO bilayer system. The larger peaks in the imaginary part of the susceptibility (b) correspond to the Néel temperature (taken from [15]).

system Co/CoO can be calculated

$$\chi = 37 \frac{\mu\text{rad}}{\text{ML}} \times 32\,\text{ML} \times 0.2 \frac{\text{mrad}}{\text{Oe}} = 0.24 \frac{\mu\text{rad}}{\text{Oe}}. \tag{2.55}$$

This is a rotation that should be detectable even with the present setup. On the other hand, for a thinner film of only 1 ML thickness, for example, a Kerr rotation of 7.4 nrad/Oe is expected, which is below the detection limit of the present setup. It remains to show whether the improved setup proposed in this thesis can resolve such small signals.

The above calculation relies only on the theoretically expected rotation for Co/W(110), so using experimental values for the Kerr rotation might be

more accurate. Using a rotation of 16 μrad/ML obtained by Oepen *et al.* [29] for the magnetization saturation of a 2 ML Co/Cu(001) system, a rotation 3.2 nrad/(ML Oe) is expected, which is about 2 times smaller than that expected for the 1 ML Co/W(110) above. However, one has to take into account that Oepen measured the Co rotation on a Cu substrate and not on W, so it seems reasonable that the expected rotation is larger than 3.2 nrad/(ML Oe).

The second approach to the detection of the antiferromagnetic state near T_N employs the transverse susceptibility. By simultaneously polarizing the statistical fluctuations in the two magnetization sublattices and measuring the susceptibility response, a small net magnetic moment can be detected. To estimate the expected signal sizes, transverse susceptibility signals of ferromagnets near the Curie temperature are considered since the net moment arises by an analogous mechanism. In particular, in a FM, the applied transverse field polarizes only statistical fluctuations from the average zero net moment along the hard axis. An estimate for an expected signal size is given based on measurements performed by Jensen *et al.* [30] from the transverse susceptibility of 2 ML Co/Cu ultrathin films.

They detected the Curie transition along the hard axis of the FM, but with a peak signal that was about 500 times smaller than that measured with the parallel susceptibility along the easy axis (see figure 2.10). In previous measurements on the 2 ML Fe/W(110) system in our group, susceptibility peak sizes along the easy axis of about 5 μrad/Oe have been observed. Assuming that the peak AFM susceptibility is 500 times smaller than this, a signal size

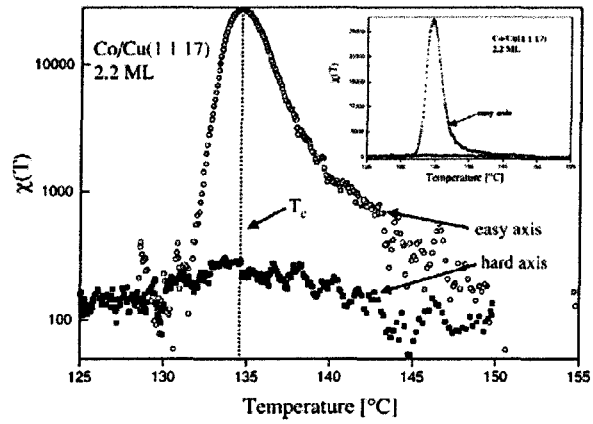

Figure 2.10: Transverse susceptibility measurements on 2.2 ML Co/Cu. The hard axis susceptibility peak is about 100 times smaller than the easy axis peak. Taking into account that the hard axis signal was measured by applying a magnetic field that was 5 times bigger than that along the easy axis, the real ratio between easy and hard axis susceptibility peaks is 500 (taken from [30]).

of 10 nrad/Oe is expected for a 2 ML Fe film. One goal of this thesis is to show whether signals that small can be detected with the new setup. The 2 ML Fe/W(110) system will be used as a test study (see chapter 5).

Chapter 3

Experimental methods

This chapter comprises an overview of the measurement methods employed in this thesis. They include the preparation of ultrathin magnetic films by molecular beam epitaxy (MBE), the characterization and surface analysis of the films and the W(110) substrate, as well as the *in situ* measurement of the magnetic ac-susceptibility by means of the surface magneto-optic Kerr effect (SMOKE) in ultrahigh vacuum (UHV).

The structure of this chapter follows the course of a typical experiment, starting with an introduction to the UHV system and apparatus used. The preparation of ultrathin films is described next, before proceeding to the characterization of substrate and film using Auger electron spectroscopy (AES) and low-energy electron diffraction (LEED). The chapter is concluded with a detailed description of the setup for magnetic ac-susceptibility measurements as performed in this work.

3.1 Ultrahigh vacuum system

The preparation of ultrathin magnetic films and the investigation of their properties *in situ* is a challenging task since all experiments require an ultrahigh vacuum (UHV) environment with a base pressure $\approx 10^{-10}$ mbar. This ensures that the surface of a few atomic layer thin (monolayer) film remains free of residual gas contaminants such as CO and CO_2 for a period of about 4 - 5 hours which sets the typical time frame for an experiment. Measurements on "clean" ultrathin films obviously have to take place in UHV, since the removal of the film from the chamber quickly leads to surface contamination. Though contamination could in principle be avoided by covering the film with a thin non-magnetic capping layer (Au or Cu, for example) which then allows *ex situ* measurements, it has been found that capping layers screen the film's magnetic response and even profoundly alter its magnetic properties by, for example, reducing the Curie temperature [31]. Measurements in this thesis are therefore performed in situ.

3.1.1 Preparation of UHV

In what follows, various components of the vacuum system used in this work (fig. 3.1) are described by illustrating how ultrahigh vacuum conditions are achieved.

Starting from atmospheric pressure in the stainless steel chamber (C) and in all vacuum lines connected to the pumps (that is, the ion pump isolation

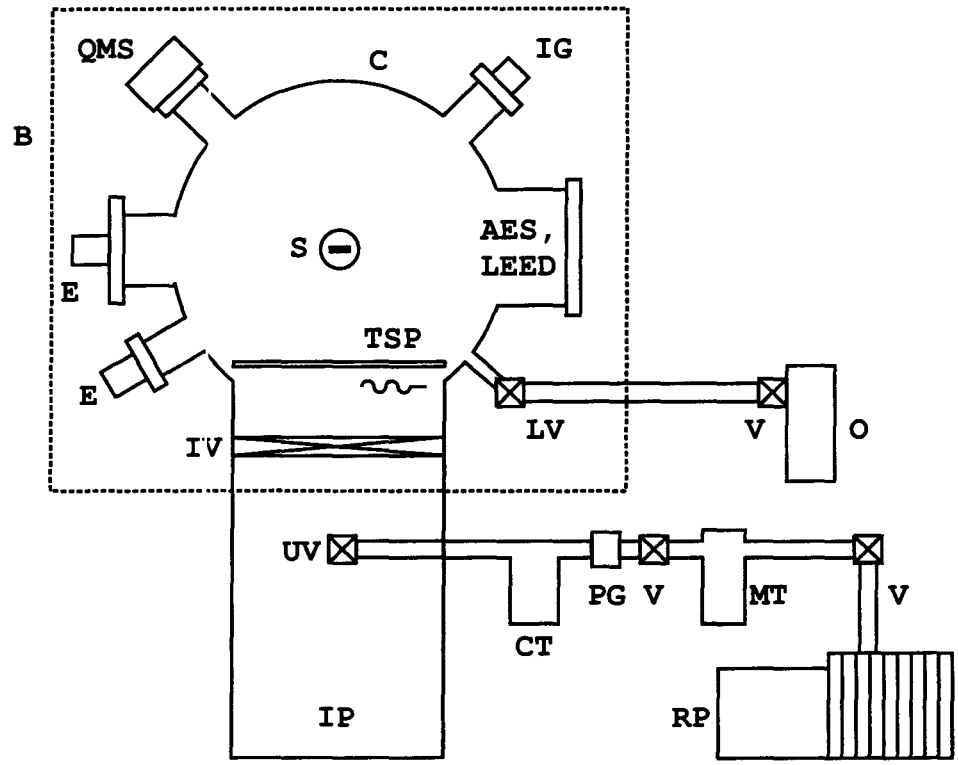

Figure 3.1: UHV apparatus and selected components: QMS - quadrupole mass spectrometer, C - stainless steel chamber (∅=6 in), IG - ion gauge, B - removable bake-out oven, E - metal source evaporators, S - sample with Helmholtz coils, AES - AES and LEED spectrometers, TSP - Titanium sublimation pump, LV - leak valve, V - valve, O - Oxygen gas supply, IV - ion pump isolation valve, UV - ultrahigh vacuum valve, PG - Pirani gauge, MT - molecular sieve trap, CT - liquid N_2 cold trap, IP - ion pump, RP - mechanical rotary pump; not shown: manipulator arm, optical setup

valve (IP) and the leak valve (LV) are closed (see fig. 3.1)), a mechanical rotary pump (RP) is first used to reduce the overall pressure in the system. This type of pump is very reliable and can run continuously as a backing pump. The main disadvantage of the rotary pump is a possible back-streaming of oil and oil vapors into the pump lines and chamber once the pump is shut off when

the lines are still under vacuum. A widely used safety measure is a molecular sieve trap (MT) that is situated further up in the pump fore-line. It is filled with pellets of a porous synthetic material that acts as a very good absorbent due to its extremely large surface area and pore size. It is not only effective in the absorption of oil vapors but also helps reduce the amount of water vapor or other large gas molecules in the fore-line.

After some time, usually about 30 minutes, the pressure in the system reads $\leq 10^{-2}$ mbar on the Pirani Gauge (PG in fig. 3.1). At this point, another type of trap, a so-called cold trap, is used to facilitate the pumping to lower pressures. This cold trap (CT) is cooled in a liquid nitrogen lN_2 bath (hence its name), and is basically a complex tube system mounted in the fore-line with the sole purpose of trapping gas molecules on its walls. After about 1 hour of further pumping with the trap, the pressure is reduced to $\leq 10^{-4}$ mbar. At this point, the ultrahigh vacuum valve (UV) is closed, effectively separating the chamber from the pumping line system. The ion pump isolation valve (IV) is now opened very slowly such that an already working ion pump (IP) below the chamber is not overloaded by too high a pressure. This ion pump is used to further lower the pressure in the chamber down to $\leq 10^{-8}$ mbar, it is also the primary chamber pump and is always running. The pumping relies on sorption processes - ionized gas particles impinge on a titanium plate where they are either absorbed or where they sputter titanium atoms away to nearby surfaces forming a fresh, unoxidized Ti film. This film readily forms solid stable compounds with reactive gas molecules like CO_2, N_2 or O_2.

Once the chamber pressure is in the 10^{-8} mbar range, a bake-out oven (B) is set on top of the chamber, which is then heated evenly for an extended period of time, typically 24 - 48 hours. The purpose of the bake-out is to remove water vapor and gas molecules that have been adsorbed on the surfaces inside the chamber. The bake-out is usually started at a temperature of 80 °C, especially after putting components such as newly charged metal evaporators into the chamber, as they outgas significantly and increase the ion pump pressure up to the low 10^{-6} mbar range. The pressure is monitored simultaneously on the now operating ion gauge (IG) and the ion pump. It is crucial that the ion pump does not trip since it is the only pump working on the chamber. For safety reasons, it will turn itself off above a critical current flow which coincides with the pressure rising above 10^{-6} mbar. After a few hours of bake-out at a low temperature of 80 °C, the temperature is raised to 120 °C - 150 °C. In general, the temperature and time needed for a bake-out are estimated based on experience and on conditions such as the installation of new equipment inside the chamber, the time the chamber has been at atmospheric pressure or even the humidity in the laboratory while the chamber was left open.

After a successful bake-out and cool-down of the chamber, the pressure usually reads $\leq 5 \times 10^{-9}$ mbar. At this point, to achieve the UHV needed for experiments, the last pump in the system is employed, the titanium sublimation pump (TSP). Similar to the ion pump, the TSP makes use of the good getting qualities of titanium. By running a high current of 45 A – 47 A

through a 0.5 cm thick titanium filament (fig. 3.1) for about 45 s, a fresh titanium layer sublimates on the inner side walls of the lower portion of the chamber. A μ-metal plate as shown in figure 3.1 shields the sample holder and other parts of the equipment in the chamber from getting covered with the titanium film. On the chamber walls, titanium reacts with residual gas atoms by quickly adsorbing them. The solid compounds are then either pumped away by the ion pump or embedded in the titanium film and fixed to the chamber walls. Repetitive use of the TSP lowers the pressure of the chamber to its base value of about 2×10^{-10} mbar.

As a last step before experiments can take place, almost all components inside the chamber (quadrupole mass spectrometer (QMS), Auger electron spectrometer (AES) and evaporators (E), for example) have to be degassed. The degassing is a process which facilitates the removal of any leftover surface contamination from the rough surfaces of the equipment by heating them for approximately 1 hour. After degassing, the residual gas composition inside the chamber can be analyzed by a quadrupole mass spectrometer (QMS) which is a standard instrument that can be found in most UHV systems and is also used for leak detection with He gas.

3.1.2 Sample holder and manipulator arm

Another integral part of the UHV system is the sample holder (fig. 3.2) sitting on the manipulator arm. The design used in this work is described in this section, mainly because of its relevance to the mechanical stability required to

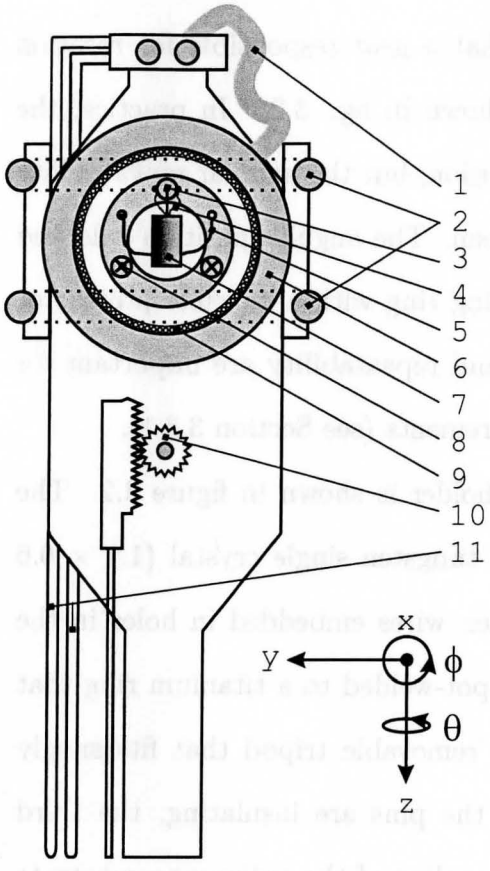

Figure 3.2: Simplified layout of the sample holder:
1 - Copper braid used for cooling, extending to liquid N_2 reservoir, 2 - cross-section through pair of Helmholtz coils, providing an in-plane magnetic field, 3 - part of tripod holding a Ti support ring (with sample), used as cooling finger ensuring even cooling of ring and sample, 4 - Tungsten/rhenium thermocouple embedded in substrate, 5 - one of three W support wires set in holes in the side of the W crystal, 6 - outer metal ring, perpendicular coil for out-of-plane magnetic field, 7 - W single crystal substrate, 8 - insulating part of tripod, 9 - sapphire ball-bearings electrically isolating sample and Ti ring from rest of holder, used for smooth azimuthal rotation (in-plane) of inner ring, 10 - gear for azimuthal rotation, moved by rack translated in z-direction, 11 - cooling pipes leading from LN_2 reservoir to supply outside chamber

optimize magnetic measurements, the theme of this thesis.

The sample holder is clamped to a UHV-compatible metal manipulator arm allowing for translational motion in 3 dimensions (coordinate system shown in fig. 3.2) extending approximately 30 cm into the chamber. The manipulator arm allows additionally for polar angle adjustment (θ in the figure) about the z-axis, adjustable from about $250° < \theta < 110°$ in coarse steps of 1°. In particular, angles of 90° and 270° are set for film growth and AES or LEED measurements, respectively. Sub-degree fine adjustment is obtained by means

of a small screw moving a pinion such that a gear responsible for rotation moves a small fraction of a degree (not shown in fig. 3.2). In practice, the polar angle can be set to at least 0.2° precision, but the angular repeatability is $\geq 0.3°$ due to the design of the mechanism. The angular position is locked by a thumb screw fixing a stationary locking ring with a movable protractor ring attached to the gear. Both locking and repeatability are important for the optical setup used for magnetic measurements (see Section 3.3.1).

A simplified sketch of the sample holder is shown in figure 3.2. The substrate on which films are grown (7), a tungsten single crystal ($1.1 \times 0.6 \times 0.2$ cm^3), is suspended by three tungsten wires embedded in holes in the sides of the substrate (5). The wires are spot-welded to a titanium ring that is supported by three pins (8) forming a removable tripod that fits snugly into rotatable ring underneath. Two of the pins are insulating, the third one is made of copper (3) and is used for cooling of the entire ring-substrate assembly. The pin is attached to a copper braid (1) connected to a liquid nitrogen reservoir. From the reservoir, thin pipes (11) lead outside the chamber and are coiled in a dewar vessel filled with LN_2. Gaseous nitrogen passed through the pipes is liquefied in the coil and then carried into the chamber.

The temperature of the substrate is measured by a $W_{95}Rh_5/W_{74}Rh_{26}$ thermocouple that is in direct contact with the substrate (4). Accurate temperature readings over a range of 150 K to at least 2500 K are made possible in this way. Heating of the substrate is realized in two different ways. For low and intermediate temperature ranges, radiative heating from a W filament

behind the substrate is employed. Higher temperatures up to $\approx$ 2500 K, as needed for the flashing of the substrate, for example, are reached by electron bombardment of electrons thermally emitted by the same filament.

The rotatable ring holding the tripod with the substrate provides an in-plane rotation of the sample about the x-axis. It is isolated from the rest of the sample holder by sapphire ball-bearings (9) and connected only to a gear system (not shown in the figure). A small gear wheel (10) sits at the end of this gear system. It is moved by a rack, which, in turn, is attached to a manipulator outside the chamber through a spring-drive shaft mechanism. It has been found that this setup introduces a mechanical hysteresis and an additional instability into the system. Care must be taken not to touch the manipulator during experiments (see Chapter 4).

The sample holder incorporates two coil systems close to the sample for magnetic measurements. One pair of coreless Helmholtz coils (2) is used to create an in-plane magnetic field of up to 80 Oe, two separate out-of-plane coils underneath a metal ring centered around the substrate (6) can be used to create (dc and ac) fields along the x-axis perpendicular to the substrate. A third coil system is situated outside the chamber. It is used to cancel the effect of Earth's magnetic field (about 0.5 Oe) in the vicinity of the chamber center where the sample normally is located during measurements.

In conclusion, it can be seen that the many degrees of freedom for the positioning of the sample in the chamber and the complex additions to the sample holder (cooling, heating, magnetic coils) make the setup very versatile.

However, they are also responsible for inducing mechanical instabilities which are a major concern for magneto-optic measurements as performed in this thesis (Section 3.3.1). Some approaches used in this work to address this issue are discussed in Chapter 4.2.

3.2 Film preparation and characterization

The preparation of ultrathin films is an essential part of this thesis, since any magnetic measurement relies on successful film growth to begin with.

That is why in the first part of this section, details pertaining to film growth in general are presented. The growth parameters and structural determination of the bcc Fe(110)/W(110) and fcc Fe(111)/Ni(111)/W(110) systems used in this work have been studied and reported in the past [32], [33], [12], and [34] and [26]. Apart from a slight fine-tuning of parameters to optimize film growth, the previously published growth recipes were followed. Growth details are therefore addressed only in a very short form here.

In the second part of this section, two common surface science techniques employed in this thesis, Auger electron spectroscopy (AES) and low-energy electron diffraction (LEED), are described. AES and LEED are important for calibrating the film thickness and for monitoring the film growth and they are treated in this context only.

3.2.1 Film growth

The growth of an ultrathin film starts with the preparation of a clean substrate. The substrate used in this thesis is a tungsten (W) single crystal (dimensions $1.1 \times 0.6 \times 0.2$ cm^3) that is cut to 0.2° precision and polished to expose its crystallographic (110)-face. In addition to being non-magnetic, this substrate material was chosen for several reasons. Firstly, it has a body-centered cubic (bcc) structure with surface lattice constants similar to those of the film material. Film growth is thus facilitated by reducing the lattice mismatch and by supplying a good template for pseudomorphic growth (at least for the first layer(s) before lattice strains lead to reconstruction). Secondly, the W (110)-surface is only weakly reactive and has a relatively high surface energy preventing alloying and interdiffusion processes. This leads to sharp interfaces between film and substrate and is also the reason why "wetting" of the films and smooth film growth are favored. Lastly, the high melting point of W ($\approx$ 3700 K) makes it easy to remove films from the substrate and to prepare a fresh surface by flashing, which is a short (10 s) annealing of the crystal to about 2500 K, a temperature at which most materials desorb from its surface.

Cleaning of the W substrate beyond the simple flashing procedure performed before each experiment usually becomes necessary every 3 to 4 days, as repeated heating of the substrate leads to carbon segregation from the bulk of the crystal that cannot be removed by flashing. Carbon is the main surface contaminant on the tungsten surface. Fortunately, it can be removed by a

series of short heatings of the crystal to roughly 1000 K in an oxygen partial pressure of up to 10^{-6} mbar (thermally activated oxidation of the carbon) and by subsequent flashing up to 2500 K. The success of the cleaning can be verified by AES (see section 3.2.2).

Ultrathin film growth can be accomplished by several techniques such as pulsed-laser deposition (PLD) and molecular beam epitaxy (MBE). While PLD is primarily used for the growth of complex materials like transition metal oxides and has only recently been "discovered" for the growth of metallic ultrathin films [36], MBE is a mature and readily available technique that has been applied successfully to the growth of high-quality metallic films in a layer-by-layer fashion for many years.

In this thesis, MBE is used for the controlled growth of Fe and Ni, two of the three 3d ferromagnets (Fe, Co, Ni). MBE relies on thermal deposition. More specifically, atoms are usually evaporated from a bulk source and the resulting atomic flux is directed at the substrate where the atoms adsorb on the surface. The biggest advantage of this method is the slow deposition rate that allows for good epitaxial growth and that is also especially useful for growing ultrathin (1-5 ML) films.

The layout of an electron beam evaporator used for MBE in our group is illustrated in figure 3.3. The evaporator is custom-made after a design by T. Jones *et al.* [37] that has been refined and set up recently. The working principle is straightforward.

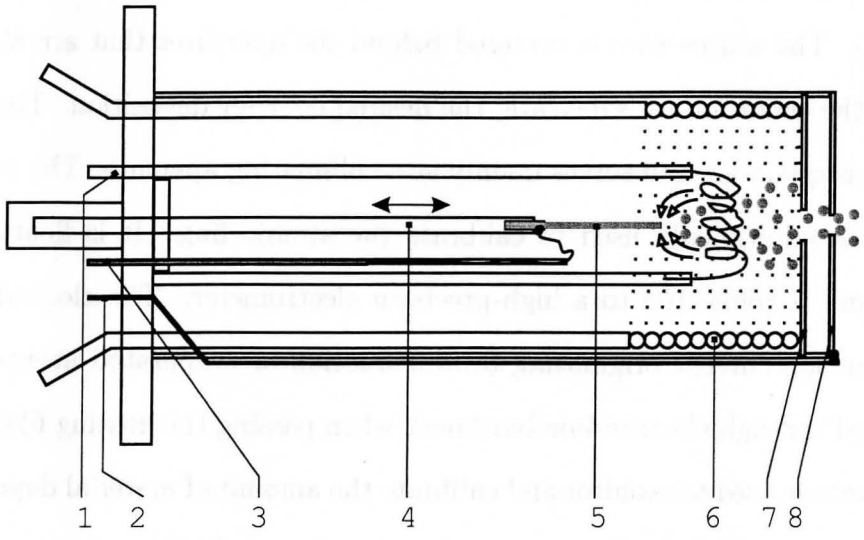

Figure 3.3: Simplified layout of the metal evaporators (not to scale): 1 - current feedthrough for heating filament, 2 - second aperture current feedthrough (ion monitor), 3 - high-voltage feedthrough, 4 - metal rod used for translation of metal source, 5 - high-purity metal source wire (⌀= 1 mm), 6 - cross-section through coiled tube for cooling water, 7 - first aperture (collimating), 8 - second aperture

The source material, a high-purity (99.99%) metal wire (of 1 mm diameter), is held at a high voltage of 1.75 kV, with its tip situated about 14 mm behind a grounded semi-circular W heating filament that has an ac current of 3.5 A running through it. Electrons emitted by the hot filament are accelerated by the high voltage and are focused onto the tip of the source wire, thus melting it and leading to evaporation of the material. Overheating of the evaporation area is avoided by a cooling system that surrounds the source wire and the filament. It consists of a coiled cooling tube through which water is circulating.

The direction and flux of the atoms are calibrated by means of two

apertures. The source wire is centered behind the apertures that are aligned towards the center of the substrate, the desired spot for deposition. The first aperture is grounded and serves mainly as a collimating aperture. The second aperture is additionally used to calibrate the atomic flux. It is floating at +23 V and is connected to a high-precision electrometer. The electrometer records an ion current originating from a fraction of evaporated atoms that are ionized through electron bombardment when passing the heating filament. This current is used to monitor and calibrate the amount of material deposited on the substrate by using its direct proportionality to the flux of atoms leaving the evaporator. Monitoring the second aperture current is therefore a convenient method for maintaining a steady deposition rate. Typical ion currents are in the range of 1 - 2 nA and result in a deposition rate of about 0.2 ML/min. This rate is fairly small compared to other techniques, but it allows the growth of ultrathin films with a high precision. The low atomic flux also ensures that the vacuum inside the chamber remains in the 10^{-10} mbar range during deposition which is rarely the case in other growth techniques.

The way atoms arrange themselves on the substrate surface to build up a film is usually described in the phenomenological framework of equilibrium growth modes that are divided into three categories (fig. 3.4). The simplest one is the Frank-van der Merwe (FM) mode. It is also commonly referred to as layer-by-layer mode because the n^{th} layer does not begin to grow until the $(n-1)^{th}$ layer is complete. This is obviously the preferred mode in ultrathin film engineering since smooth films with perfect interfaces can be grown. More

common but less favored modes are Stranski-Krastanov (SK) and Volmer-Weber (VW). In the SK mode, growth usually starts in a layer-by-layer fashion but upon reaching a certain thickness (sometimes after the first monolayer), three-dimensional islands with bulk lattice parameters start to form. The SK mode is therefore often called layer-plus-island mode. Three-dimensional islands that grow from the onset of film growth are characteristic for the VW mode. Clearly, SK and VW modes are disadvantageous with respect to the ultrathin film research of this thesis since they result in an inhomogeneous film structure. However, metastable growth modes approximating FV can often be realized by varying parameters such as the substrate temperature during growth.

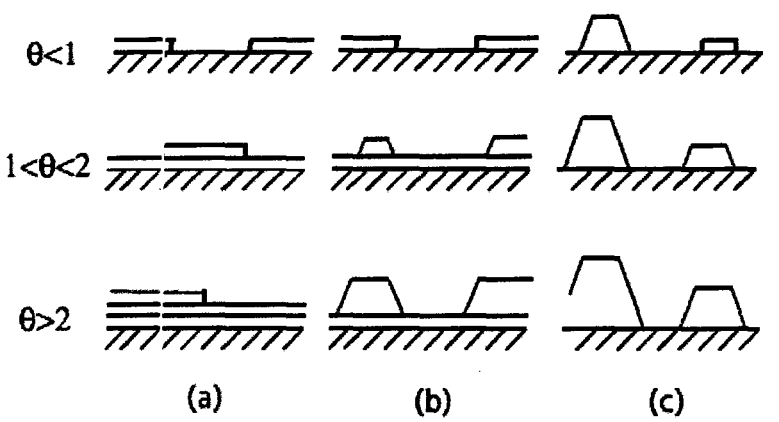

Figure 3.4: Morphology of growing films with increasing film coverage θ in monolayers showing (a) Frank-van der Merwe growth, (b) Stranski-Krastanov growth and (c) Volmer-Weber growth [38]).

The actual growth mode of a film is determined by the exact growth conditions, growth temperature and rate, and depends on the film/substrate

characteristics. Due to these many parameters, the successful growth of ultra-thin films with specific structural properties often represents a challenge.

For example, in the bcc Fe(110)/W(110) system, it has been found [32], [26] that the first monolayer grows in the FM mode when prepared at a temperature 300 K $\leq T <$ 900 K, whereas the second monolayer grows in an approximate layer-by-layer mode only if prepared at 300 K. For this reason, Fe/W films are grown in this thesis as follows: The first monolayer is deposited at room temperature ($\approx$ 300 K) and annealed to 500 K for about 2 minutes to ensure good wetting of the film. All subsequent (partial) layers are then grown again at $\approx$ 300 K.

A more complex growth process can be observed for the fcc Fe(111)/2 ML Ni(111)/W(110) system. Here, Fe that is naturally growing in a bcc structure is coerced into growing as face-centered cubic (fcc) structure (up to a thickness of 3 monolayers where it reverts back to bcc) by using a 2 monolayer thick fcc (111) Ni template on top of W [34]. It should be clear that the growth recipe for Fe/Ni/W is not as straightforward as in the Fe/W system. It is only shortly outlined here for later reference.

The first monolayer of Ni is deposited at a temperature of 550 K and annealed to 600 K for 2 minutes. Examination of the LEED pattern reveals a 7x1 structure of Ni(111)/W(110) (see section 3.2.2). The second layer of Ni is grown at a lower temperature of 390 K before Fe is deposited at 360 K. Finally, the whole film is annealed shortly to 400 K for 2 minutes. This ensures homogeneity and thermal stability of the film against annealing effects.

3.2.2 Film characterization

The verification and determination of the grown film's composition and structure are the next step before performing magnetic measurements. For these purposes, two very popular techniques in surface science are employed: Auger electron spectroscopy (AES) and low-energy electron diffraction (LEED). Both are extremely surface sensitive due to the strong Coulomb interaction between the electrons and the material.

The basic principles of AES and LEED and their application to the characterization of ultrathin films used in our laboratory are presented in this section.

Auger electron spectroscopy

Auger electron spectroscopy (AES) was developed as a surface science technique in the late 1960's and has become one of the most common techniques for determining the composition of surfaces, especially in the limit of ultrathin films. It is named after the Auger effect that first has been observed by Pierre Auger in 1925 [39]. The Auger process is illustrated in figure 3.5.

A highly energetic electron (1.5 keV) hits the sample and ionizes an atom by removing an electron from an inner core shell. The so created core hole can be filled by an electron from a higher shell. This relaxation process is either accompanied by the emission of an X-ray photon (X-ray fluorescence) or by a radiationless transfer of an electron. In the latter case, the energy released in the transition ΔE is passed onto an electron in a higher shell that

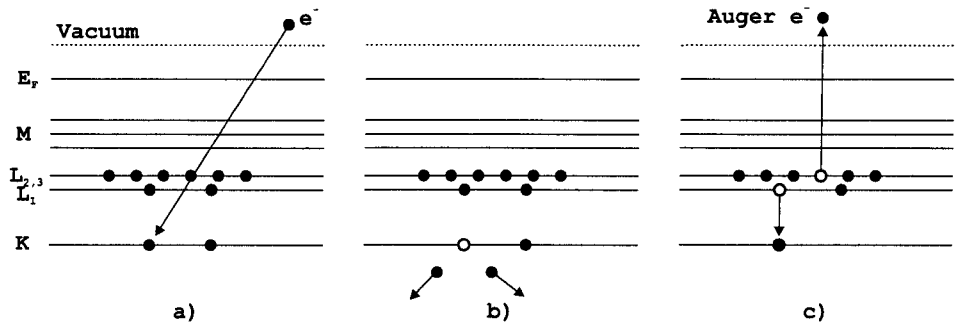

Figure 3.5: Schematic representation of the Auger process. Ionization of the atom (a), creation of a core hole (b), and non-radiative relaxation by emission of an Auger electron (c). Shown is a KLL transition - an electron is ejected from the atom's K-shell, an L-shell electron falls into the vacant hole, and another L-shell electron is emitted as Auger electron, carrying the excess energy away.

can then escape the atom, provided that its binding energy E_B is smaller than the energy difference ΔE. This so-called Auger electron then has a kinetic energy given by

$$E_{kin} = \Delta E - E_B. \tag{3.1}$$

Auger electron energies are typically in the range of 20 - 600 eV and have thus a relatively short inelastic mean free path (IMFP) of only a few lattice spacings. This is the reason why AES is very sensitive to the surface of a material only.

Since the initial ionization-core hole creation can occur in various shells, a spectrum of Auger electrons with specific energies characteristic of each element can be recorded. This is done in AES by detecting the number of electrons hitting a screen while scanning through a range of kinetic energies. In fact, not all electrons hitting the detector stem from Auger processes. Most

detected electrons are back-scattered secondary electrons that produce a big smooth background in the N(E)dE (number of detected electrons at energy E) spectrum obscuring the Auger peaks. In order to enhance the detection of Auger electron peaks, the spectrum of N(E) is differentiated (dN(E)/dE) by making use of a lock-in technique described in detail in [26].

The derivative spectrum shows clear peaks at certain energies that allow the identification of the Auger electron emitting species. One main application of AES based on this element specificity is the monitoring of surface contaminations.

As mentioned in section 3.2.1, the main surface contaminant of tungsten is carbon. The Auger spectrum of a carbon contaminated W surface should therefore show both C and W peaks. Spectra of a clean and contaminated W surface are shown in figure 3.6. Peaks at 168 eV and 182 eV are attributed to tungsten, while the peak at 271 eV is characteristic for carbon.

By calculating the ratio of the peak sizes (C/W) a measure for the cleanliness of the W surface can be obtained. Usually, the W surface is considered to be clean when no carbon peak can be detected. Cleaning of the substrate in O_2 is generally undertaken once a C/W ratio of $\geq 10\%$ is reached since the film growth becomes affected by the carbon contamination at that point.

Another important application of AES in this thesis is the thickness calibration of deposited films. The use of a quartz oscillator often used for monitoring film thicknesses is not favored because in the thickness ranges of

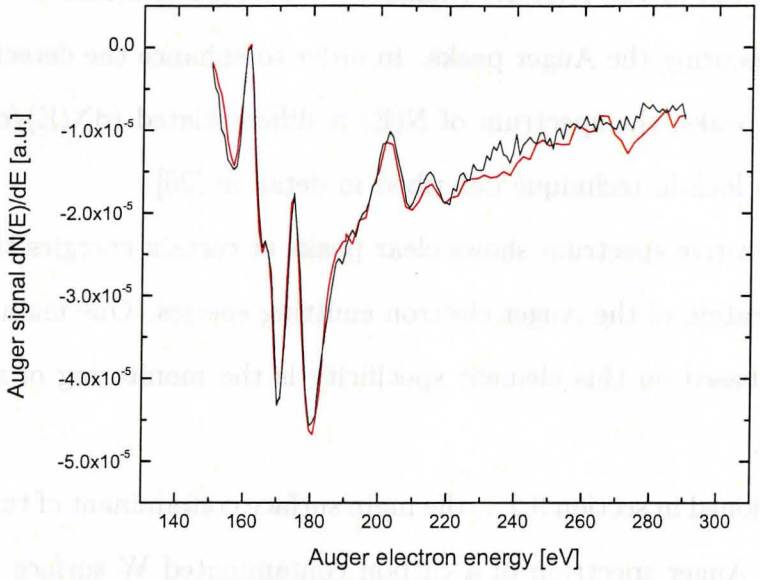

Figure 3.6: Auger spectrum showing W (182 eV) and C (271 eV) features. The red (black) curve corresponds to a C contaminated (clean) W surface.

1-2 ML used in this work, the calibration by AES is more precise.

A particularly convenient calibration method makes use of the Auger intensity attenuation from the bare substrate atoms upon film coverage. As a layer grows on top of the substrate in the Frank-van der Merwe (FM), or layer-by-layer growth mode, the "clean" Auger peak signal decreases linearly reflecting the constant rate in which the surface becomes covered by atoms. Examining the signal as a function of film coverage (or alternatively, as a function of deposition time), linear segments with clear breakpoints are observed (fig. 3.7), with each breakpoint corresponding to the completion of one layer.

The intensities at the breakpoints are decreasing exponentially, which is not surprising since the Auger electrons are exponentially attenuated when traveling through successive film layers. During the growth of the first monolayer (coverage $\theta < 1$) in the FM mode, the Auger signal $h(\theta)$ can be expressed as

$$h(\theta) = h_0 - h_0(1 - \exp(-d/\lambda))\theta \tag{3.2}$$

with h_0 being the clean substrate signal, d the film thickness and λ being the inelastic mean free path (IMFP) of the electrons in the film material.At the first breakpoint, i.e. at completion of the first monolayer, $\theta = 1$, such that equation (3.2) becomes

$$\frac{h_0 - h(\theta = 1)}{h_0} = 1 - \exp(-d/\lambda) \tag{3.3}$$

$$\frac{h(\theta = 1)}{h_0} = \exp(-d/\lambda). \tag{3.4}$$

This means that the relative Auger intensity at the breakpoint depends only on the IMFP of the electrons and the thickness of the adsorbate film. For Fe and Ni grown at room temperature without annealing, the first breakpoint occurs at relative Auger intensities of 0.6 and 0.55, respectively.

If one wishes to study the thickness, composition and the degree of intermixing in a composite system such as Fe/Ni/W, for example, uptake or build-up curves are used instead of substrate attenuation curves [34]. In this method, the element specificity of the Auger process is exploited knowing the characteristic Auger peaks of Fe (47 eV) and Ni (61 eV). Again assuming layer-by-layer growth, the signal is seen to increase linearly until one layer is

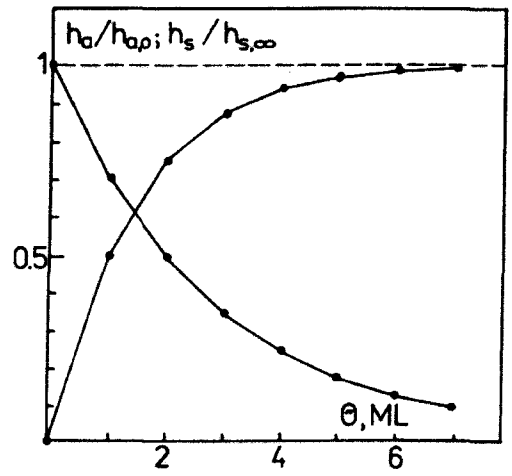

Figure 3.7: Auger attenuation and build-up curves for layer-by-layer growth, showing linear segments and breakpoints corresponding to completion of single layers (taken and adapted from [35]).

completed, at which point it continues to increase at a different slope until the completion of the second layer.

As shown above, the thickness calibration via breakpoints in the attenuation or build-up curves is straightforward for layer-by-layer growth. For other growth modes such as SK or VW, the thickness calibration can be challenging. In the SK (or layer-plus-island) growth, for example, linear segments are observed up to a critical thickness at which island formation sets in, recognizable by a more or less continuous variation in the AES signal. VW growth is characterized by the absence of breakpoints.

Low-energy electron diffraction

Low-energy electron diffraction (LEED) is a powerful technique for the study of surface morphology and structure. It has first been proposed in 1927 by Davisson and Germer [40]. Since then the technique has evolved and been perfected and is very well understood by surface scientists. For many years, LEED has been the technique to beat when it came to determining the location of atoms on surfaces. Only recently, with the availability of UHV compatible scanning tunneling microscopes (UHV-STM), the importance of LEED seems to have receded. This can be attributed to the advantages of STMs which consist in the resolution of atomic positions in real space rather than in reciprocal space (as is the case in LEED). Nevertheless, most UHV systems are equipped with LEED systems rather than with UHV-STMs simply for economical reasons.

The information LEED provides about surface structure can be of both quantitative and qualitative nature [41], [42]. The qualitative use of LEED in ultrathin film research is straightforward and documented well, and is thus applied in this thesis.

LEED is based on the elastic back-scattering of low-energy electrons through diffraction from a surface. A well-collimated monoenergetic beam of electrons (usually in the range of 30 - 300 eV) impinges at normal incidence on the sample surface. A fraction of the electrons is diffracted by elastic scattering from the periodic arrangement of the surface atoms in the lattice.The basics of LEED can be understood from the point of view of conservation of

linear momentum. At normal incidence, all electrons have a wavevector $\vec{k}_i$ perpendicular to the surface. Diffraction at a surface requires conservation of linear momentum parallel to the surface ($\vec{p}_{\|} = \hbar\vec{k}_{\|}$). Electrons thus need to have a component of the wavevector parallel to the surface after diffraction. It is given by

$$\vec{k}_{\|,f} = \vec{k}_{\|,i} + \vec{G}, \tag{3.5}$$

which means that the change in wavevector $\Delta\vec{k}_{\|}$ equals a reciprocal lattice vector $\vec{G}$ (in practice, the parallel component for the incident wavevector is zero due to normal incidence)

$$\Delta\vec{k}_{\|} = \vec{k}_{\|,f} - \vec{k}_{\|,i} = \vec{G}. \tag{3.6}$$

Thus every point in the diffraction pattern corresponds to a reciprocal lattice vector (or a multiple thereof). From the diffraction pattern in reciprocal space, the real space atomic arrangement can be determined.

As mentioned before, the diffraction pattern yields two types of information: On a qualitative level, the spot positions in the diffraction pattern can be used to extract the size, symmetry, and angular orientation of the surface's unit cell in reciprocal space as explained above. This is especially useful for monitoring film growth as the arrangement of the film's atoms on the substrate surface can be determined (see figure 3.10). Furthermore, the sharpness of spots is usually taken as an indication for a clean, homogeneous surface with high structural ordering. In a quantitative use of LEED, intensities of

diffracted beams are recorded as a function of energy of the incident electrons. The comparison of such I(E) curves with theoretical models is rather cumbersome because multiple scatterings at the surface have to be considered.

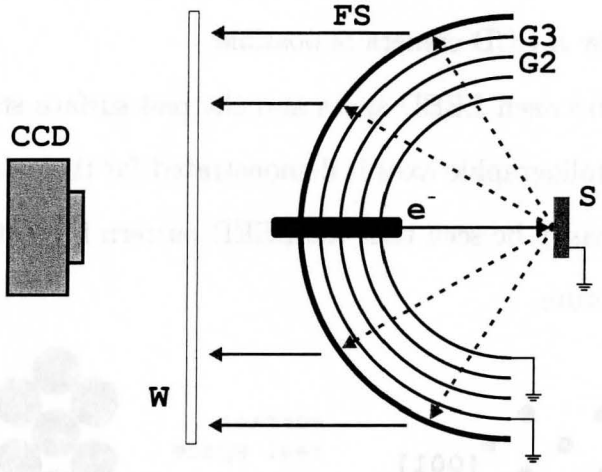

Figure 3.8: Schematic of LEED setup: Electron beam e^- hits the sample S, gets diffracted back and passes retarding grids G2 and G3 (G1 is grounded) before impinging on a fluorescent screen FS. A UHV window W allows the observation of diffraction pattern on the screen, a CCD camera records diffraction images.

The experimental LEED setup as it is used in our lab is shown in figure 3.8. An electron gun creates a beam of electrons that is impinging on the sample surface at normal incidence. The diffracted electrons are detected using a retarding-grid analyser that is also used for AES. As shown in figure 3.8, it consists of 4 hemispherical concentric grids and a fluorescent screen. The first grid is grounded to provide a field-free region between sample and grid minimizing electrostatic interactions that might deflect electrons. The second and third grids are sometimes called suppressor grids, since a negative applied

voltage rejects all inelastically scattered electrons and allows only elastically scattered electrons within a certain energy range to pass. Finally, the electrons are accelerated by a high voltage (5 kV) before hitting the fluorescent screen, making the diffracted beams visible. Through a UHV window, recording of diffraction patterns by a CCD camera is possible.

The relation between LEED spots and the real surface structure with reference to the crystallographic axes is demonstrated for the case of W (110) in figure 3.9. It can easily be seen that the LEED pattern is rotated by 90° to the real surface structure.

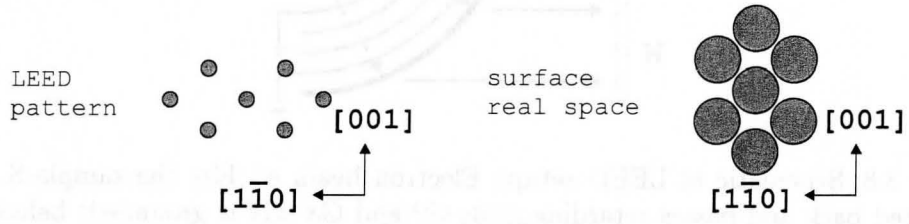

Figure 3.9: Demonstration of the relationship between LEED pattern (reciprocal lattice) and real space surface structure

Three examples of LEED diffraction patterns are given in figure 3.10. The actual LEED patterns are shown in reverse contrast (bright LEED spots on the fluorescent screen appear now as dark spots). The first picture represents the diffraction pattern of the clean W (110) surface. The specular W spot in the center is obscured by the electron gun. In the center and to the left (and upper) side of the gun's position, 3 additional, spurious spots are present in all pictures. These spurious spots originate from electrons escaping

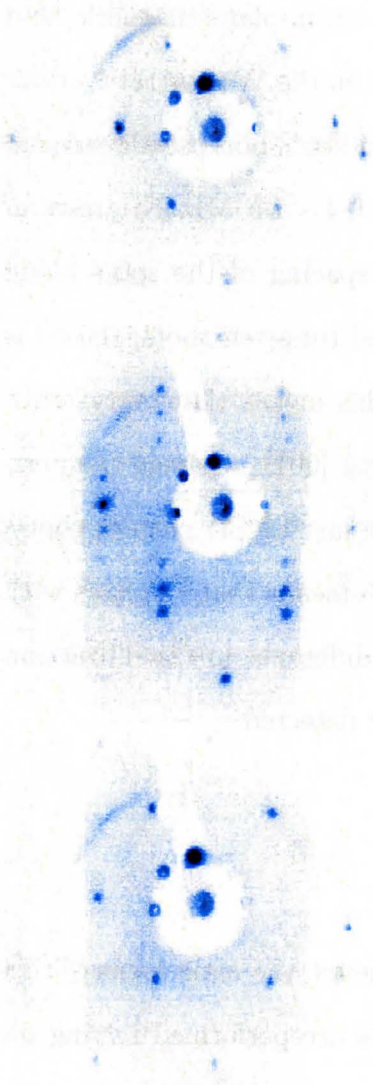

Figure 3.10: LEED diffraction pattern (reverse contrast) recorded by a CCD camera. From top to bottom: (110)-surface of W substrate at 260 eV, 7x1 structure of 1 ML Ni on top of W at 202 eV, pseudomorphic structure of 1 ML Fe on top of W at 265 eV.

the electron gun which is obviously not perfectly shielded by a stainless steel cap. In addition, to each side of the diffracted spots, two very pale (almost white) vertical areas can be perceived that partially cover a diffracted spot in the right side of the Ni and Fe patterns. Those light areas are the shadows of

the two Helmholtz coils that are used to produce an in-plane magnetic field (see figure 3.2). The second picture shows 1 ML Ni on the W substrate. Additional satellite spots around the primary W spots indicate non-pseudomorphic growth. In fact, in the thickness region between 0.4 - 1.5 ML, Ni grows in a strained 7x1 structure on top of W [43]. The spacing of the spots along the [001]-direction is now only 1/7th of the original tungsten spots, the Ni is highly strained in that direction. In real space, this means that every tenth Ni atom coincides with every eighth W atom along [001], whereas the periodicity along the $[1\bar{1}0]$ direction is preserved. The last LEED pattern shows the pseudomorphic growth of 1 ML Fe on W, which means that Fe grows with the substrate structure. That is why basically no difference in the diffraction patterns between clean W and 1 ML Fe/W can be detected.

3.3 Magnetic measurements

This section is concerned with magnetic measurements, the main focus of this thesis. As already mentioned, these measurements are performed relying on SMOKE (2.3.3). This method has been applied to ultrathin films now for about two decades, mainly in a dc setup for the acquisition of magnetization (M vs H) curves [19]. SMOKE is used in this thesis for measurements of the ac susceptibility χ.

The optical setup which forms the basis for the measurement is described in the first part of this section. Modifications to the setup that were

implemented during the course of this work are presented next. Details regarding the basic measurement technique as used for dc measurements are put forth with the purpose of illustrating key aspects of the SMOKE technique and its performance. In particular, an aspect relevant for all in-situ measurements using SMOKE - the effect of UHV windows - is treated.

In the last part of this section, the measurement of the magnetic ac susceptibility is described. The setup is introduced in detail. The section is concluded with a calibration scheme of the ac susceptibility in absolute optical and magnetic units. Details regarding the characterization of the susceptibility setup with respect to its performance (signal-to-noise) are not given in this section. They are discussed in the next chapter.

3.3.1 Optical setup and basic measurement techniques

The optical setup of the in situ SMOKE apparatus is shown in a simplified picture in figure 3.11. Light emerges from a laser, is linearly polarized by a Glan-Taylor polarizing prism with its transmission axis at an angle θ_i from s- or p-polarization and passes through an optical UHV window. Then, upon reflection from the (magnetic) sample, the beam experiences a change in polarization state, passes through a second optical UHV window and then through a Glan-Laser type analyzing polarizer with its axis at an angle θ_a, nearly crossed with respect to the initial polarization. Finally, the light impinges on a photodetector.

To be more precise, the input stage comprises a 5 mW HeNe 632.8 nm

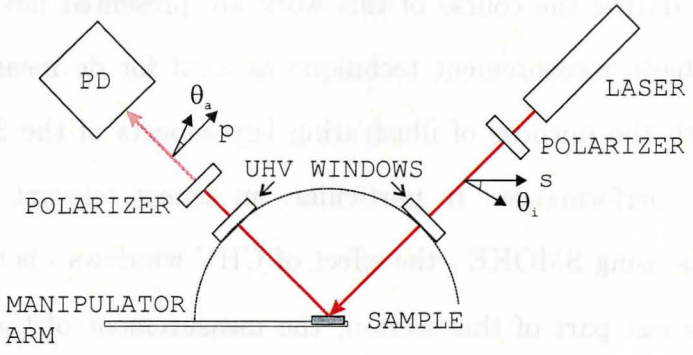

Figure 3.11: Simplified SMOKE setup - the initial polarization after the first polarizer is linear, off-set at an angle θ_i from s- (or p-) polarization, whereas the analyzing polarizer is set at θ_a from p- (or s-) polarization.

laser (type UniPhase 1125p) with a longterm intensity stability of 0.1%, a 5 mm clear aperture Glan-Taylor polarizing prism on a rotational mount with 1° resolution and two beam steering mirrors on gimbal mounts. The light passes through an ordinary $2\frac{3}{4}$ in. quartz window at normal incidence and impinges on the sample at an angle of about 45°. The reflected light then passes through an exit window, of same type as the first, an analyzing 8 mm clear aperture Glan-Laser polarizer, and is subsequently steered through a HeNe red-line 10 nm bandpass filter and focussed onto a silicon photodiode. The detection stage comprising the analyzing polarizer, the HeNe filter, focusing lens, silicon photodiode and amplification electronics is mounted on an arcminute (0.01°) precision rotational stage that is rigidly attached to the UHV window on the chamber. The silicon photodiode has a responsitivity of $\alpha = 0.3$ A/W and its sensitivity is sufficient for the experiments performed in this thesis.

The working principle of the optical setup has in principle remained

unchanged from previous works ([26] and [11]), however, several major constructional changes to the setup have been implemented in the course of this work. All these technical modifications have been undertaken with the goal of increasing the sensitivity to SMOKE signals by primarily enhancing the mechanical stability of the apparatus.

First, a new laser with better intensity stability has been chosen (HeNe type Uniphase 1125p). Second, a Glan-Laser type polarizing prism (Q-switch) with two exit windows and 633 nm anti-reflection coating on all exit faces is now used. Finally, a new detecting stage incorporating the new polarizer has been built, with its cross-section shown in figure 3.12.

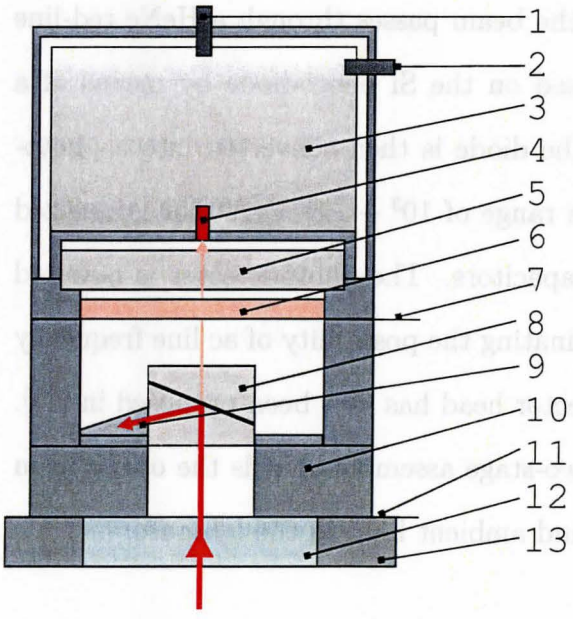

Figure 3.12: Schematics of SMOKE detector stage: 1 - feedthrough to BNC connector, 2 - Detector head housing with gain selection (potentiometer), 3 - Detector electronics/amplifier circuit, 4 - Silicon photodiode, 5 - focusing lens, 6 - HeNe red-line filter, 7 - removable detector head stage, 8 - Glan-Laser polarizing prism with exit ports, 9 - beam dump to absorb totally-internally reflected (TIR) component, 10 - rotational mount upon which polarizer is fixed, 11 - removable rotary stage with arcminute precision, 12 - UHV window, 13 - adapter for rotary stage clamped to UHV window port

The entire detector assembly consists of two separate, removable stages that are bolted onto an adapter rigidly clamped around the UHV view port.

The rotational mount forms the first stage. It holds the analyzing Glan-Laser polarizer with its transmission axis aligned with the center of rotation and a beam dump that almost perfectly absorbs the unwanted totally-internally reflected (TIR) component of the beam. The polarizer/beam dump assembly is surrounded by an Al cylinder whose inner surfaces are roughened and blackened to prevent possible back-scattering into the crystal. This stage is normally attached to the chamber and only removed during bakeouts so as not to damage the polarizer crystal. The second stage consists of a metal plate with perpendicular slits allowing for the insertion of apertures. It also holds the detector head, which is fastened to the rotational mount for experiments. After leaving the polarizing prism, the beam passes through a HeNe red-line 10 nm bandpass filter and is focussed on the Si photodiode by means of a convex lens. The photocurrent at the diode is then converted into a photovoltage with a selectable gain in the range of $10^3 - 10^9$ V/A that is realized by a combination of resistors and capacitors. The photodetector is powered by two 9 V batteries effectively eliminating the possibility of ac line frequency pickup. The design of the photodetector head has first been proposed in [11]. As shown in the figure, the entire two-stage assembly shields the optics from external influences such as background ambient light in the laboratory.

A basic SMOKE measurement utilizes a polarizer setup as shown in figure 3.11. The analyzing polarizer is nearly crossed with respect to the initial polarization.

The intensity detected after the analyzing polarizer is given by

$$I(\theta) = I_{\max}(\sin^2(\theta) + \epsilon) \tag{3.7}$$

where $I_{\max}$ is the intensity incident on the analyzing polarizer and θ is the angle of the second polarizer from the extinction angle. The extinction ratio ϵ is a measure for the quality of the polarizers. It is defined as the ratio of the transmitted intensity for perfectly crossed polarizers to the intensity for parallel polarizers

$$\epsilon = \frac{I_\perp}{I_\parallel}. \tag{3.8}$$

This means that for perfect polarizers, there is no transmitted intensity and that the extinction ratio is zero. A finite value of ϵ, as is the case in any measurement (the polarizers used in this thesis have a guaranteed extinction ratio of $< 10^{-6}$), corresponds to an intensity offset of $\epsilon I_{\max}$ at $\theta = 0$. As shall be seen later, ϵ is one of the factors limiting the sensitivity of SMOKE measurements. As the polarization of the reflected light is slightly rotated by $\delta\theta$ due to the magnetization of the sample[1], the change in the analyzer intensity becomes

$$\delta I = 2I_{\max} \sin(\theta)\cos(\theta)\delta\theta. \tag{3.9}$$

It has been found [44], [45], that rather than measuring at $\theta = 45°$ as eq. 3.9 suggests, the optimal angular setting for θ can be determined from the contrast

[1] $\delta\theta$ will later be referred to as Kerr rotation angle Φ_K.

$\delta I/I(\theta)$. By combining eq. 3.7 with eq. 3.9 and by using a small angle approximation for $\sin(\theta)$ and $\cos(\theta)$, the contrast is given by

$$\frac{\delta I}{I(\theta)} = \frac{2\theta\delta\theta}{\theta^2 + \epsilon}. \tag{3.10}$$

It can be shown that it reaches its maximum for

$$\theta_{\mathrm{m}} = \sqrt{\epsilon} \tag{3.11}$$

at which point the contrast becomes

$$\frac{\delta I}{I(\theta_{\mathrm{m}})} = \frac{\delta\theta}{\sqrt{\epsilon}}. \tag{3.12}$$

It is thus the extinction ratio that limits the signal contrast. The set point angle θ_{m} can easily be found by setting the analyzer angle such that the detected intensity $I(\theta_{\mathrm{m}})$ is twice the intensity at extinction. Eq. 3.12 can be used for calibration of the magnetic signal units of Kerr rotation angle. For example, in a typical magnetization loop (where the transmitted intensity is recorded as a function of applied magnetic field), an ultrathin Fe film causes a polarization rotation on the order of 10 μrad. In fact, the observed switching $\delta\theta/\theta_{\mathrm{average}}$ can lie between 0.2% and 6%, depending on the extinction ratio. This illustrates the importance of a small ϵ in measurements since the signal can otherwise very quickly be buried in noise.

The discussion above has, until now, been applied to a rather perfect system, neglecting a vital aspect relevant for any *in situ* SMOKE measurement - the effect of UHV windows. UHV windows are made of quartz, a material

that becomes birefringent when put under stress (which is obviously the case for UHV windows that are tightly held in a ring bolted to the chamber). The birefringence produces a small change in the polarization state by introducing a phase shift δ that transforms the initial linear polarization into a slightly elliptical state (see fig. 2.6). Even though this phase shift is usually small ($\approx 2° - 3°$) for linearly polarized light under normal incidence, the extinction ratio increases dramatically (up to two orders of magnitude) from the values that could in principle be obtained with the polarizers alone (ϵ typically lies in the low 10^{-6} range). Clearly, this adversely affects the S/N, since the size of the measured signal at the analyzing polarizer is reduced and most likely obscured by a large background due to noise that scales with the intensity of the detected beam.

Several approaches aiming to compensate for window birefringence have been proposed, most of them relying on the use of a quarter-wave plate [3], of a variable wave-plate (a so-called Babinet-Soleil compensator) [46] or even on the use of an elegant setup using a lock-in technique involving a photoelastic modulator (PEM) [47].

In this work, a simple yet very successful method developed in our group [49] is employed for the compensation of the undesirable window effects. The method is simple in the sense that it does not require any additional optical components. It exploits the idea that only s- or p-polarized light is reflected from a non-magnetic sample without changing the polarization state since these are the eigenstates for reflections (see chapter 2.3.3). By slightly

rotating the initial linear polarization from the s- or p-state, an additional phase shift is introduced at the sample surface upon reflection. It is this phase shift that is used to cancel the phase shift from the windows.

Mathematically, this technique can be described in the Jones matrix formalism. In brief, the initial two-component polarization vector $\vec{E}_i$ is transformed through the action of 2x2 matrices representing optical components that, for example, transmit the beam (windows) or reflect it (sample). The effective product matrix $\vec{M}_{eff}$ containing all optical elements in the beam path connects the initial $\vec{E}_i$ and final $\vec{E}_f$ Jones vectors. The final transmitted intensity I_f equals $\left|\vec{E}_f \vec{E}_f^*\right|$ (for more details, see [48] and [49]).

Experimentally, in order to find the angle from s- or p-polarization required to "null" the overall ellipticity, an iterative procedure is employed. In a first step, the initial polarization is set to either the s- or p-state, depending on the desired Kerr geometry (see chapter 2.3.3). The intensity minimum at the detector is found by adjusting the analyzing polarizer. The extinction ratio is calculated. Then, the initial polarizer is rotated by a few arcminutes and the minimum transmitted intensity is found again. If the extinction ratio gets smaller, the process is repeated, otherwise, the initial polarization is adjusted in the opposite direction. The iteration process continues until a global minimum in the extinction ratio is attained. It has been found that with the setup used in this thesis, the minimum extinction ratio occurs at about 3° from the initial s- or p-state, rather than at 5° as measured in the previous setup [49]. The smallest obtained extinction ratio (with the use of 1 mm apertures), how-

ever, is $\approx 2 \times 10^{-6}$, which is about 5x larger than the best extinction ratio achieved with the old setup.

As a final remark regarding the window compensation used to reduce the extinction ratio and to increase the S/N, a drawback of the technique has to be mentioned. Though the method is simple and easy to implement, it does not permit the Kerr rotation θ_K and Kerr ellipticity η_K to be distinguished. (The complex Kerr angle was defined as $\Phi_K = \theta_K + i\eta_K$.) Thus, in measurements performed in this thesis, Φ_K is measured as a mixture of Kerr rotation and ellipticity which is reasonable in the ultrathin film limit where only very small signals are measured anyway.

3.3.2 Ac susceptibility measurements

The ac susceptibility measurement uses the same optical setup as the dc setup presented above. However, the operation principle is quite different. A sinusoidally varying magnetic field $H(\omega) = H_0(\sin(\omega t))$ with amplitude H_0 and frequency ω is applied to the sample causing a magnetization oscillating with the same frequency. It is this ac magnetization that leads to an ac intensity change at the photodetector proportional to $\chi = \partial M/\partial H$ (see chapter 2.2). When the temperature of the sample is varied while measuring the ac magnetic response of the sample, the ac susceptibility as a function of temperature $\chi(T)$ can be recorded.

The detection of the ac intensity is realized by a dual-phase lock-in amplifier. This type of lock-in measures the photodetector intensity at the

frequency of the magnetic field set by the lock-in as a reference frequency in the first place. Furthermore, this dual-phase amplifier is capable of measuring two phases of the ac signal (in-phase and out-of-phase separated by $\pi/2$), which allows a simultaneous recording of the real (χ) and imaginary (χ'') parts of the complex susceptibility $\chi = \chi' + i\chi''$. One example of a $\chi(T)$ curve showing the complex susceptibility is presented in figure 3.13.

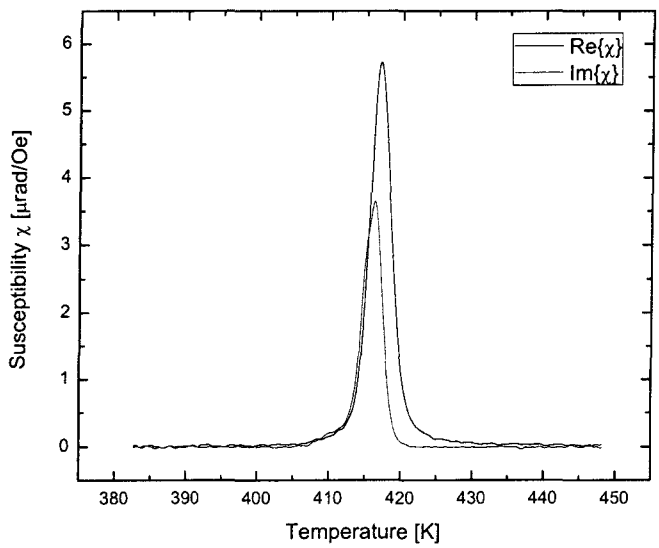

Figure 3.13: Complex susceptibility $\chi = \chi' + i\chi''$ of a 1.8 ML Fe/W(110) film as a function of temperature with an applied magnetic field of 0.5 Oe

A block diagram illustrating the susceptibility setup is shown in figure 3.14. The lock-in amplifier for the optical signal is shown on the left side (labeled EG&G7260). In what follows, this setup is described in more detail starting again with the generation of the oscillating magnetic field.

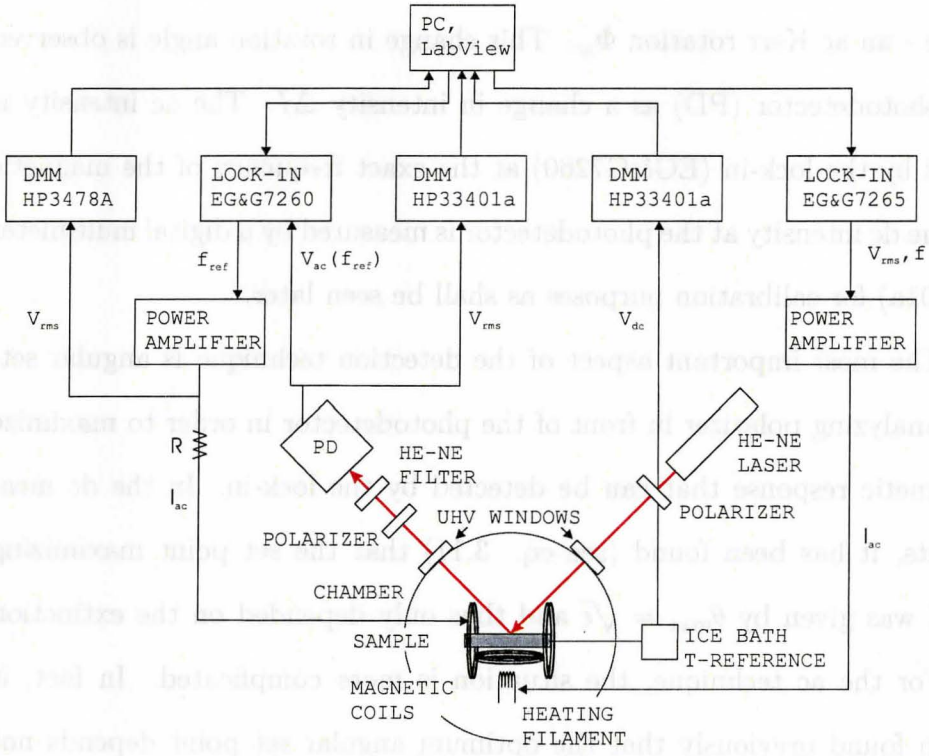

Figure 3.14: Block diagram for susceptibility measurements. See text for details.

The lock-in first supplies a reference frequency that can be set by the computer program (LabView) to a power amplifier at which the amplitude of the current (or magnetic field H_0) can be regulated manually. The ac current output of the power amplifier $I_{\rm ac}$ passes through a 4 Ω resistor (R) and runs through the magnetic coils at the sample creating a magnetic field

either parallel or perpendicular to the field. The amplifier output is monitored and recorded as a rms-voltage $V_{\rm rms}$ at a digital multimeter (HP3478A). It is used for the calibration of the magnetic field.

At the sample, the oscillating magnetic field now causes an ac magnetic response - an ac Kerr rotation $\Phi_{\rm ac}$. This change in rotation angle is observed at the photodetector (PD) as a change in intensity ΔI. The ac intensity is recorded by the lock-in (EG&G7260) at the exact frequency of the magnetic field. The dc intensity at the photodetector is measured by a digital multimeter (HP33401a) for calibration purposes as shall be seen later.

The most important aspect of the detection technique is angular setting of analyzing polarizer in front of the photodetector in order to maximize the magnetic response that can be detected by the lock-in. In the dc measurements, it has been found (see eq. 3.11) that the set point maximizing the S/N was given by $\theta_{\rm max} = \sqrt{\epsilon}$ and thus only depended on the extinction ratio. For the ac technique, the situation is more complicated. In fact, it has been found previously that the optimum angular set point depends not only on the extinction ratio but also on frequency dependent factors such as mechanical vibrations, for example, that introduce intensity fluctuations at the photodetector [50]. For susceptibility measurements as performed in this thesis, a study of the S/N as a function of analyzer angle shows (ch. 4.4.2) that an angular setting of 24 arcminutes gives the best S/N. It is this angle that is used for all measurements.

In the right half of the block diagram (fig. 3.14), components relevant

for the temperature variation at the sample are shown. First of all, the temperature of the sample is measured using a thermocouple embedded in its sides (see section 3.1.2) that is leading to an ice bath reference outside the chamber. The thermovoltage is recorded by a digital multimeter (HP33401a) and provided to the measurement program. The program then controls a lock-in amplifier (EG&G7265) that provides an rms-voltage at a frequency of 4.7 kHz to a power amplifier. The amplitude of the rms-voltage output depends on the difference between the desired and measured temperatures. Different heating rates ($R = \mathrm{d}T/\mathrm{d}t$) can be chosen by the experimenter. They are obtained by linearly increasing the set point temperature (the desired temperature). The voltage output is then changed accordingly in a feedback loop.

As mentioned above, the susceptibility signal is recorded as a change in intensity at the photodetector. A first calibration step that finds the change in the rotation angle of the polarization attributed to SMOKE makes use of eq. 3.7:

$$\Delta\Phi_{\mathrm{ac}} = \frac{\Delta I}{2\theta_{\mathrm{set}} I_{\mathrm{max}}}, \tag{3.13}$$

where θ_{set} is the angular set point at 24 arcminutes (see above), ΔI the ac signal recorded by the lock-in and where $\Delta\Phi_{\mathrm{ac}} = \Delta\theta$ is the Kerr ac rotation. Recalling that the susceptibility is proportional to the change in Kerr rotation divided by the change in magnetic field $\chi \propto \delta\Phi_{\mathrm{ac}}/\delta H$, this equation can be used to approximately calibrate the measured susceptibility in absolute optical

units (radians/Oe):

$$\chi = \frac{\Phi_{ac}}{H_0} \tag{3.14}$$

$$\chi = \frac{\Delta I(\theta_{set}^2 + \epsilon)}{2\theta_{set} I(\theta_{set}) H_0} \tag{3.15}$$

Here, the susceptibility is approximated linearly which is allowed in the limit of very small magnetic fields H_0 given in units of Oersted. A small angle approximation in eq. 3.7 was used ($\sin^2(\theta) \approx \theta^2$) to relate I_{max} to the instantaneous dc intensity at the photodetector $I(\theta_{set})$. Also, the relevant parameters that have to be determined prior to the measurements are shown: the angular set point θ_{set} and the extinction ratio ϵ. (All other parameters are read by the susceptbility program.)

Finally, to convert from optical units into magnetic (SI) units, eq. 3.15 is extended to give

$$\chi = \left(\frac{4\pi}{1000}\right) \frac{\Delta I M_{sat}(\theta_{set}^2 + \epsilon)}{2\theta_{set} I(\theta_{set}) H_0 \Theta_K t}. \tag{3.16}$$

Here, M_{sat} represents the saturation magnetization for bulk iron (1752 emu/cm^3), and Θ_K denotes the saturation Kerr rotation that has been measured previously for a 1 ML Fe/W(110) film. The value of Θ_K is found to be 250 μrad/ML in the geometry used in this thesis. The parameter t is referring to the thickness of the film in monolayers (ML). Finally, the factor $4\pi/1000$ converts between cgs and SI units. This calibration is an approximation, since M_{sat} is taken for bulk iron and is not necessarily the same on a film.

So far, no attention has been paid to the distinction between real and

imaginary parts of the complex susceptibility. Both components were detected by the dual-phase lock-in with the real part being measured in-phase and the imaginary part $\pi/2$ out-of-phase. Considering the measurement technique of the lock-in, it detects signals with the same phase as its reference frequency and 90° to it. However, phase shifts between the lock-in reference frequency output and its signal input are not accounted for. Obviously, it is important to determine those phase shifts in order to properly distinguish real and imaginary parts of the susceptibility.

The phase shifts introduced in the setup are frequency dependent and attributed to three main factors: First, the power amplifier circuit that amplifies and provides the signal at the reference frequency to the magnetic coils introduces a phase shift. Second, the cables leading to the coils and the coils themselves have an inductance and capacitance that changes the phase difference slightly. Finally, the inverting photodetector amplifier circuit induces another phase shift that depends on the detector gain (for a gain of $G = 10^7$ V/A, $R = 10$ MΩ and $C = 5$ pF). In this thesis, all three effects have been quantified by the use of a LRC-bridge and it has been found that for in-plane measurements of the susceptibility at a frequency of $f = 150$ Hz, an overall phase shift of $\phi = 135°$ was present between the lock-in input and output. This phase angle is used in the calibration to separate the real and imaginary components of χ by a simple matrix operation:

$$\begin{pmatrix} \cos(\phi) & -\sin(\phi) \\ \sin(\phi) & \cos(\phi) \end{pmatrix} \begin{pmatrix} x \\ y \end{pmatrix} = \begin{pmatrix} Re(\chi) \\ Im(\chi) \end{pmatrix} \tag{3.17}$$

It is thus easy to convert the detected ac signal at the x and y channels into proper real and imaginary parts using eqs. 3.17 and 3.16.

Chapter 4

Characterization of the system

Considerations on the performance of the ac susceptibility measurements via SMOKE and experiments to characterize the new system are presented in this chapter. In the first part, details concerning the experimental setup and, in particular, changes to the optical setup are discussed and put into context. Furthermore, issues related to the experimental procedure and the signal detection are treated in some detail. After that, a model describing the signal-to-noise ratio (SNR) in ac susceptibility measurements is presented and related to SNR measurements in the present system. The experimental results are used to characterize the performance of the system and to compare it to previous work by C.S. Arnold [11, 50]. Finally, the feasibility of ac susceptibility measurements on antiferromagnetic ultrathin films is discussed and additional possible improvements to the setup are put forward.

4.1 Optical setup

The optical setup is the basis for high-quality measurements of the complex Kerr rotation. It determines the overall performance of the system. One of the main concerns in this thesis is therefore the quality and the proper use of the polarizing crystals, the UHV windows and the laser.

4.1.1 Polarizing crystals and UHV windows

The first significant change to the experimental setup in this work is the use of a Glan-laser polarizing crystal as analyzing crystal. Previously, a Glan-Thompson polarizing crystal has been used. The operation principle of both polarizing crystals is similar and shown in figure 4.1. Both crystals are composed of two separate high-purity calcite prisms that are either glued together (Glan-Thompson) or are assembled by leaving a small air gap (Glan-laser). Elliptically polarized light impinges ideally at normal incidence on the first prism, travels through the material and impinges on the interface between the two prisms. The hypotenuse angle is chosen to be at the Brewster angle for HeNe laser light (632.8 nm) in the particular calcite material. As a result, the polarization component that is parallel to the scattering plane (the ordinary ray) experiences total internal reflection (TIR), while the perpendicular component (extra-ordinary ray) is partially transmitted. This means that when using the crystals as analyzing polarizers set near extinction, it is the TIR component that has almost the full intensity of the incident laser beam.

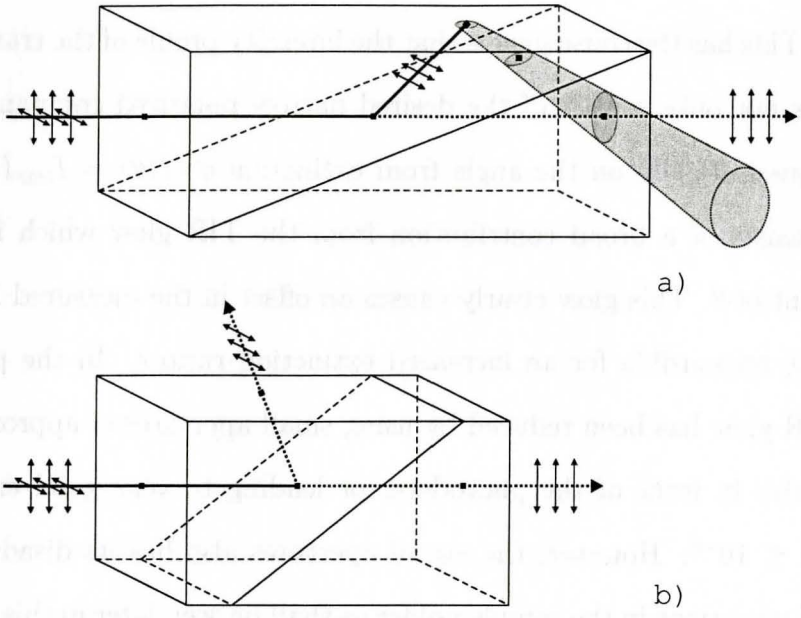

Figure 4.1: Schematic diagram showing the differences between Glan-Thompson (a) and Glan-Laser (b) polarizers. See text for details.

The difference between the two polarizers consists in the treatment of the TIR component that has a significant impact on the performance of the polarizers, i.e. the extinction ratio.

In order to prevent the TIR component from reaching the exit face of the polarizer, the Glan-Thompson crystal is embedded in calcite index-matched epoxy (except the entrance and exit faces) and in a black, absorbing holder. This measure is, however, only partially effective since a fraction of the TIR component is reflected back into the crystal from the blackened side face as shown in figure 4.1(a). Multiple scattering of this component inside the crystal produces a diffuse "glow" on the exit face that is easily visible with the room

lights off. This has the consequence that the intensity profile of the transmitted beam does not only consist of the desired narrow polarized component that depends quadratically on the angle from extinction θ ($I(\theta) = I_{\max}(\theta^2 + \epsilon)$). It also consists of a broad contribution from the TIR glow which is nearly independent of θ. This glow clearly causes an offset in the measured intensity $I(\theta)$ and is responsible for an increased extinction ratio ϵ. In the past, the diffuse TIR glow has been reduced by using small apertures of approximately 0.1 mm^2 size in front of the photodetector leading to very good extinction ratios of $\epsilon \leq 10^{-6}$. However, the use of apertures also has its disadvantages because of vibrations in the sample holder as shall be seen later in this chapter.

In the Glan-laser polarizer used in this thesis (figure 4.1(b)), a different approach is used to ensure that the TIR component does not interfere with the selected polarization at the exit face. At the position where the TIR beam is expected to hit the crystal surface, an additional exit window allows the TIR component to escape under an angle of roughly 70° to the incident beam. The escape beam can now either be detected and used for measurements or can be absorbed by a beam dump. In this thesis, a customized beam dump (from a black plastic pen tip cut to tightly enclose the exit window) is used due to space constraints in the detector stage (shown in figure 3.12). It is tilted slightly such as to accommodate the exit beam at its escape angle. The absorption of the TIR beam is nearly perfect and only a small portion of the beam has been found to scatter back into the crystal. The arrangement of the beam dump with respect to the escaping beam could definitely be improved by

manufacturing a properly sized beam dump to fit in the detector stage. In an attempt to improve the setup, a glass beam dump (the inside was etched and toner-blackened) has been used in lieu of the plastic beam dump. However, in comparison with the black plastic beam dump, no improvement has been observed.

An additional advantage of the new Glan-laser polarizer is the fact that all entrance and exit faces are covered with an anti-reflection coating for 633 nm laser light. This reduces undesired back-scattering in the chamber and in the polarizer crystal significantly.

From the above mentioned features of the Glan-laser polarizer, a small extinction ratio $\leq 10^{-6}$ should be achievable without the use of apertures. In practice, however, the smallest achieved extinction ratio with this setup in this work is $\epsilon = 7 \times 10^{-6}$ without using apertures. The reason for this might be two-fold.

Firstly, the absence of reflections from the polarizer entrance face due to the anti-reflection coating makes the collimation and beam alignment more difficult[1]. It might therefore be possible that the beam alignment used in this work is not absolutely perfect.

Secondly, two so far neglected optical components, the UHV windows, play an essential role for the smallest achievable extinction ratio. As already mentioned in chapter 3.3.1, the birefringence of the windows caused by stress in

[1]In previous work, the reflections from the UHV exit window and the reflection from the polarizer entrance face were made to lie on top of each other on the substrate surface for an optimal beam alignment.

the quartz material causes the beam to acquire a slight ellipticity, though this effect can be compensated for to a large extent. In fact, it is rather the material quality of the windows that leads to an increase in extinction ratio. The quality is mainly determined by imperfections in the quartz or scratches on the surface that scatter the beam. In the course of this work, it has been observed that the achievable extinction ratio can vary immensely depending on the position the beam passes through the UHV windows. Fortunately, the optical alignment has many degrees of freedom (adjustable beam steering mirrors and the substrate, for example) that allow for small adjustments in the beam path so that a good quality spot on the UHV windows could be found. Nevertheless, the exit UHV window had to be exchanged twice because the material quality was not satisfactory.

4.1.2 Laser performance

Another integral part of the optical setup is the 5 mW JDS Uniphase HeNe laser ($\lambda = 632$ nm) used in this thesis. As the complex Kerr rotation from the magnetic films is detected as a change in intensity near extinction of the two polarizers, one of the first experiments was concerned with the stability of the laser intensity. By recording the photodetector intensity as a function of time (figure 4.2), a low frequency drift of the laser intensity of $\approx \pm 2\%$ with a period of about 45-50 minutes has been observed. This fluctuation is considered to be laser specific and not related to a drift of the sample holder or the chamber for two reasons.

Firstly, the mean power drift of $\approx \pm 2\%$ corresponds to the specifications given by the manufacturer and secondly, a comparable measurement with a different laser (NEC-GLG 5261) gave a different period and mean fluctuation.

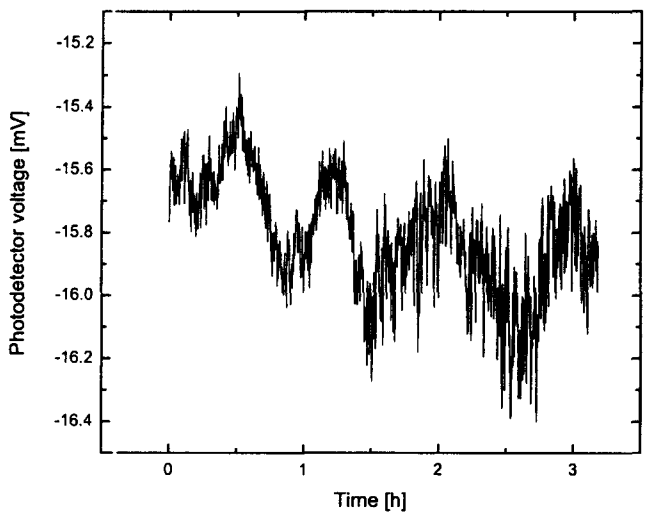

Figure 4.2: The intensity of the laser fluctuates by $\approx 2\%$ with a period of about 45-50 minutes. The origin of the higher frequency noise on top of the signal in the figure could not be determined. It is suspected that this noise is related to vibrations of the sample holder and to high frequency intensity fluctuations of the laser.

The low frequency intensity fluctuation is also observed in ac susceptibility measurements. In the experiment, the extinction ratio ϵ and the angular setting θ_{set} of the polarizer remain constant while the recorded intensity at the extinction is slowly changing with time. In order to avoid calibration instabilities, the settings for ϵ and θ_{set} are verified before each experimental run.

During the experiment, the instantaneous value of the dc intensity at the photodetector is recorded and used to calculate the maximum intensity from

$$I_{\max} = \frac{I(\theta_{\text{set}})}{(\theta_{\text{set}}^2 + \epsilon)}. \tag{4.1}$$

This has been found to give a more reliable calibration to optical units[2] than the procedure used previously [11], which kept the dc intensity at the photodetector constant by changing θ_{set}. This issue is illustrated in figure 4.3.

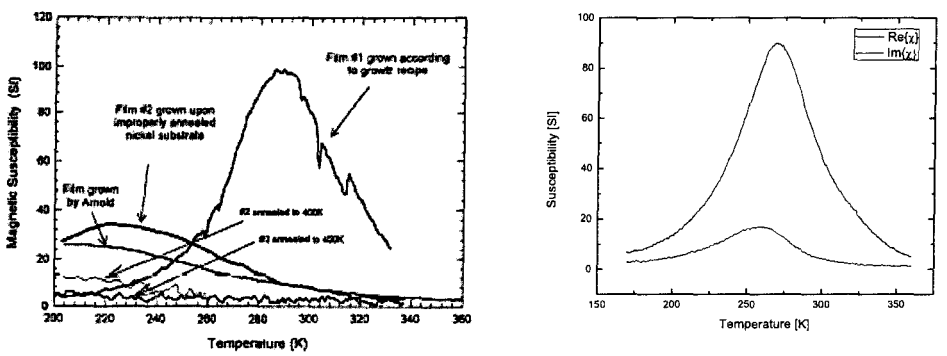

(a) (b)

Figure 4.3: Low frequency intensity fluctuations are compensated by changing θ_{set} during the experiment causing sharp dips in the $\chi(T)$ curve 4.3(a) (right side of film#1 curve, taken from [51]). Changing the experimental procedure by recording the instantaneous dc intensity while keeping θ_{set} fixed allows for a more accurate and noise-free calibration of the signal 4.3(b).

[2]The recorded ac voltage ΔI at the lock-in is related to the complex Kerr rotation $\Delta\Phi_{\text{ac}}$ and the maximum intensity $I_{\max}$ by $\Delta I = 2\theta_{\text{set}} I_{\max} \Delta\Phi_{\text{ac}}$. Thus knowing the instantaneous value of $I_{\max}$ from eq. 4.1 allows for an accurate calibration of $\Delta\Phi_{\text{ac}}$.

4.2 Mechanical stability of the setup

Mechanical stability is of paramount importance for SMOKE measurements. To reduce vibrations, the entire chamber is isolated from the ground by a set of large rubber mounts. Also, the mechanical rotary pump that usually runs as a backup pump (see chapter 3.1.1, figure 3.1) is isolated from the chamber through a series of flexible flanges. It has been observed that this method of vibration isolation is not very effective. However, any vibrations introduced by the mechanical pump can be taken care of by simply turning the pump off for the duration of the experiment. Vibrations from the optical setup are avoided by clamping the laser input and the detection stages directly to the UHV chamber windows.

Another source of mechanical instability is the sample holder mounted on the 30 cm long manipulator arm inside the chamber. Due to technical requirements for the film growth and characterization, the holder is not rigidly mounted in the chamber (see chapter 3.1.2). Mechanical vibrations of the sample holder influence the measured Kerr signal by producing noise in the reflected light beam as shown in figure 4.4.

Two different situations can be thought of generating the noise (in principle, they are coupled and should not really be considered separately). First of all, through a vertical deflection of the sample holder, the beam path and the polarization state can be changed slightly as in figure 4.4(a), resulting in a false polarization rotation signal at the photodetector. In fact, already a

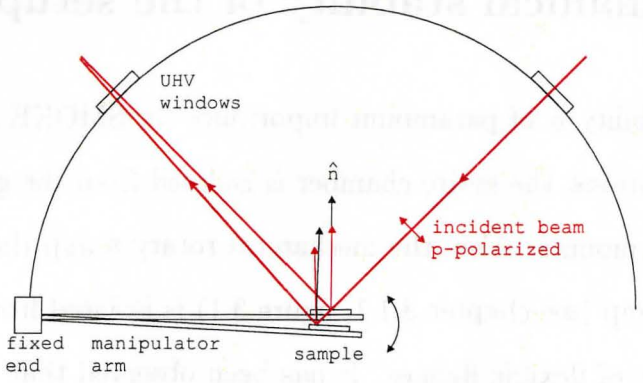

(a) sideview of the chamber

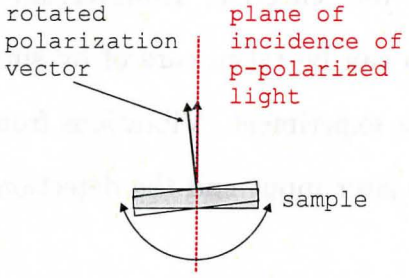

(b) view along axis of sample holder

Figure 4.4: Illustration of how vibrations of the sample holder produce vibrations in 4.4(a) both beam path and polarization state and in the polarization state 4.4(b). The incident light is p-polarized (in the plane of incidence) and therefore parallel to the sample normal for the undisturbed setup. Deflection or rotation of the sample causes the p-polarization to deviate from the sample normal and the plane of incidence, producing noise in the detected final polarization.

small deflection of the sample holder is converted to noise in the polarization signal that is comparable to the SMOKE rotation signal. For example, considering that the sample holder extends about 30 cm into the UHV chamber, a deflection of the holder by 5 μm suffices to create a false rotation signal on the order of 10^{-5} radians, which is comparable to the longitudinal SMOKE signal expected from one monolayer of iron.

The second situation arises from a slight rotation of the sample holder around its axis (figure 4.4(b)). It is easy to see that this directly produces noise in the polarization state of the incident and reflected beams.

In an attempt to stabilize the sample holder, two heavy duty springs have been incorporated in the manipulator setup outside the chamber. This reduces rotations about the axis of the holder (figure 4.4(b)) and prevents an accidental horizontal translational deflection. Furthermore, since it has been found that the manipulator rotational stage and the spring-drive mechanism responsible for the in-plane rotation of the sample are mechanically coupled, extreme care is taken not to touch any of these parts while the experiments are running.

In order to investigate the frequency dependence of the aforementioned noise contributions and to find a suitable modulating frequency for the ac susceptibility measurements, the absolute noise levels in dBV ($V = 10^{x(dBV)/20}$) at the photodetector have been recorded using an HP3582 spectrum analyzer. The result is shown for measurements in a frequency range of 0-250 Hz in figure 4.5. This measurement has been used to gain qualitative insight into the different noise contributions.

The figure shows several interesting features. First of all, sharp peaks from the line subharmonic (30 Hz), fundamental (60 Hz) and higher harmonics (120 Hz and 240 Hz) are clearly visible. Their peak size can be reduced by turning off the ion gauge within the chamber and the room light that enters the chamber and hence the detector through UHV windows (the detector stage

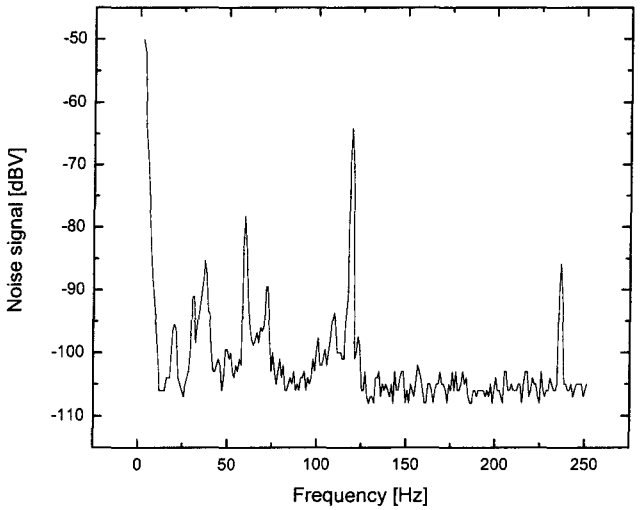

Figure 4.5: Measured noise in the SMOKE intensity at the photodetector.

itself is shielded from stray light by an aluminum housing). Furthermore, a discrete peak at 20 Hz can be observed. It has been verified that this peak originates from vibrations of the mechanical pump. Finally, rather broad peaks around 36 Hz, 72 Hz and 108 Hz have been detected. These peaks are associated with the fundamental mode of the sample holder at 36 Hz and higher harmonics which was confirmed by slightly tapping on the manipulator and viewing the response on the spectrum analyzer.

Figure 4.5 was finally used as an indicator for a good noise-free frequency region suitable for the ac susceptibility measurements. From the graph and past experience, the modulating frequency of the magnetic field was chosen to lie in between the line harmonics at 150 Hz and 210 Hz. In principle,

measurements at 210 Hz should not be ideal because 210 Hz is near a harmonic of the sample holder frequency. However, in the figure, this 6th harmonic contribution seems to be negligible.

4.3 Signal detection - photodetector and lock-in

In this section some general considerations regarding the signal detection with regard to the detector assembly and the lock-in amplifier are presented.

The detector head has been used previously in a different detection stage incorporating the old Glan-Thompson polarizer. In this thesis, some effort has been made to build a mechanically stable detector assembly consisting of the rotational mount containing the Glan-laser polarizer and the removable detector head. Special care has also been taken to shield the detector assembly from stray light. The photodetector electronics has not been changed in the course of this work. It consists of an ordinary Si photodiode with a responsivity of α=0.3 A/W at 633 nm and a current-to-voltage amplification circuit that transforms the photodiode current with a selectable gain G between 10^3 V/A and 10^9 V/A. The detector is battery-powered.

In most ac susceptibility experiments, the photodiode currents are amplified and converted with a gain of 10^7 V/A. In previous work, where apertures were necessary to prevent light scattered in the polarizer crystal from reaching the detector, a gain of 10^8 was usually chosen for best results. This choice of

a higher gain has the consequence that the detector noise voltage V_D at the lock-in increases by a factor of $\sqrt{10} \approx 3$ due to Johnson noise.

$$V_D = GN_D/\sqrt{\tau} \tag{4.2}$$

$$= G\sqrt{\frac{4k_BT}{R}}/\sqrt{\tau}. \tag{4.3}$$

Here, k_B is the Boltzmann constant, T the temperature and R the combined resistance of the detector circuit (shunt resistance + resistance in amplification circuit). τ is the time constant of the lock-in and determines the bandwidth of the measurement.

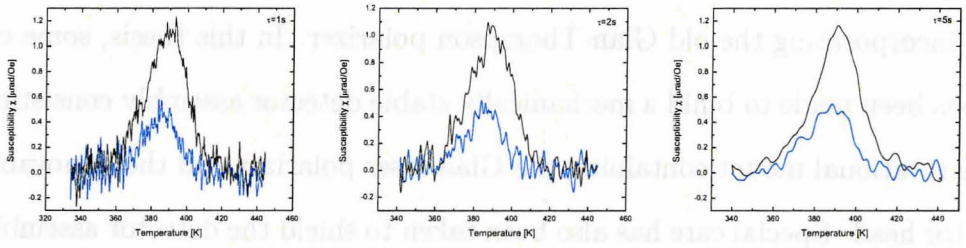

(a) (b) (c)

Figure 4.6: Susceptibility $\chi(T)$ (Re$\{\chi\}$ - black, Im$\{\chi\}$ - blue) of a poorly grown 1.8 ML Fe/W(110) film recorded with different time constants of the lock-in amplifier: 1s - 4.6(a), 2s - 4.6(b) and 5s - 4.6(c). The right choice of τ can reduce the noise significantly.

The influence of the time constant on the quality of susceptibility data is shown in figure 4.6 on a poorly grown (underannealed) 1.8 ML Fe/W(110) film. As one would expect, with increasing time constant, the data gets less noisy. Since a larger time constant results in longer data acquisition times, a compromise has to be made in experiments. In this thesis, a time constant

of $\tau = 2$ s has been found to give satisfactory results. Depending on the temperature sweeping rate and therefore the number of acquired data points, a binning procedure can also be used to reduce noise.

4.4 SNR in ac susceptibility measurements

In chapter 3.3.1, it has been mentioned that the extinction ratio is the sole limiting factor of the SNR in dc SMOKE measurements as the signal contrast goes as $1/\sqrt{\epsilon}$ determining the optimal setting angle of the polarizer $\theta_{\text{set}} = \sqrt{\epsilon}$. In an ac SMOKE (or susceptibility) measurement, the signal optimization is more difficult due to frequency dependent noise contributions that are specific to the used setup. A model that describes these issues and the performance of the system depending on the set angle θ_{set} has been successfully applied in the past [50]. It incorporates the main noise contributions that have been presented in the previous sections.

In this section, the SNR model is described and applied to the present setup. It is compared to measurements of the SNR and discussed with respect to previous work on the system as it existed prior to this thesis. After that, the feasibility of AFM ac susceptibility measurements is discussed based on the performance characteristics of the present system.

4.4.1 SNR model

As in the dc treatment of the SMOKE performance, the starting point is the detected dc intensity at the photodetector

$$I(\theta) = I_{\max}(\theta^2 + \epsilon), \tag{4.4}$$

with the variables having their usual meaning. Now, an ac modulation of the magnetization and hence of the polarization rotation leads to an ac modulated intensity signal S at the photodetector

$$S = 2I_{\max}\theta_{\text{set}}\Phi_{\text{ac}}, \tag{4.5}$$

which corresponds to the slope of eq. 4.4 at the set point θ_{set}. Φ_{ac} is the modulated Kerr rotation.

The following noise sources are considered relevant for the SNR in the ac SMOKE measurements. First of all, as mentioned earlier, fluctuations in the dc intensity $I(\theta)$ play an important role. These fluctuations $f(\omega)$ occur through fluctuations in $I_{\max}$ due to sample vibrations as shown in figure 4.4(a), scale with the intensity and produce noise ΔI_{I} at the lock-in signal within $1/\tau$ of the modulation frequency ω.

$$\Delta I_{\text{I}} = I(\theta)f(\omega)/\sqrt{\tau} \tag{4.6}$$

$$= I_{\max}(\theta^2 + \epsilon)f(\omega)/\sqrt{\tau}. \tag{4.7}$$

At the lock-in, this intensity noise is measured as a noise rms voltage ΔV_{I}

$$\Delta V_{\text{I}} = \alpha G I_{\max}(\theta^2 + \epsilon)f(\omega)/\sqrt{\tau}. \tag{4.8}$$

The second noise source at the lock-in stems from fluctuations in the rotation angle θ due to vibrations of the sample holder as in fig. 4.4(b),

$$\Delta V_\theta = 2\alpha G I_{\max} \theta \delta\theta(\omega)/\sqrt{\tau}. \tag{4.9}$$

ΔV_I and ΔV_θ are obviously correlated through the vibrations of the sample holder, however, in this model, they are treated as statistically independent for simplicity. Also, only fluctuations in the dc intensity have been taken into account. In principle, fluctuations of $I_{\max}$ or θ_{set} in the modulated signal S could be considered. But since those noise sources are much weaker than those originating from the dc intensity, they are neglected here.

A third source of noise entering the ac SMOKE measurement is the Johnson noise from the photodetector electronics

$$N_\mathrm{D} = \sqrt{\frac{4k_B T}{R}} \tag{4.10}$$

The detector noise within $1/\tau$ of the modulation frequency is transformed into a rms noise voltage at the lock-in by

$$\Delta V_\mathrm{D} = \frac{G N_\mathrm{D}}{\sqrt{\tau}}. \tag{4.11}$$

Summing the three noise terms ΔV_I, ΔV_θ and ΔV_D in quadrature and grouping terms according to θ-dependence, the signal-to-noise ratio can be written as

$$\frac{S}{N}(\theta) = \frac{2\Phi_{\mathrm{ac}}\theta\sqrt{\tau}}{\sqrt{A\theta^4 + B\theta^2 + C}}, \tag{4.12}$$

where

$$A = f^2(\omega), \tag{4.13}$$

$$B = 2f^2(\omega)\epsilon + [2\delta\theta(\omega)]^2, \tag{4.14}$$

$$C = \left(\frac{GN_{\mathrm{D}}}{V_{\max}}\right)^2 + [\epsilon f(\omega)]^2. \tag{4.15}$$

The detector noise voltage was given by eq. 4.3 and is given here again for completeness

$$V_{\mathrm{D}} = GN_{\mathrm{D}}/\sqrt{\tau} = G\sqrt{\frac{4k_{\mathrm{B}}T}{R}}/\sqrt{\tau}. \tag{4.16}$$

The $S/N(\theta)$ curve has a maximum at an angle $\theta_{\max}$ given by

$$\theta_{\max} = \left(\frac{C}{A}\right)^{1/4}, \tag{4.17}$$

at which point the SNR reaches a value of

$$\frac{S}{N}(\theta_{\max}) = \frac{2\Phi_{\mathrm{ac}}\sqrt{\tau}}{\sqrt{B + 2\sqrt{AC}}}. \tag{4.18}$$

For small values of θ, the SNR is limited by C, which is dominated by the detector noise. For intermediate values, term B (including both intensity and angular noise) gets more important and determines the maximum of the SNR as shall be seen later. For large θ, the intensity noise given by A dominates the behavior of the SNR.

4.4.2 SNR measurements and comparison with previous work

As a test study, the SNR was measured using a 1.5 ML Fe/2 ML Ni/W(110) film. In this range of iron coverage, the film magnetization is oriented per-

pendicular to the film plane. Using the polar SMOKE, a broad peak in the ac susceptibility near room temperature can be detected. It was therefore relatively easy to maintain a constant Kerr modulation Φ_{ac}. Three different measurements of the SNR on the same film are shown in figure 4.7. All measurements were performed at constant temperature and at a frequency of 210 Hz. A lock-in time constant of 2 s was employed. The three measurements differ in the following important aspects.

The rms Kerr modulation Φ_{ac} is different for all three measurements due to the film quality. For the first measurement (c), Φ_{ac} has been determined from eq. 4.5 to be 2.15 μrad. For subsequent measurements (b) and (a), the Kerr rotation has been found to be $\Phi_{ac} = 1.95$ μrad and $\Phi_{ac} = 0.66$ μrad, respectively. The last measurement (a) was performed with apertures in front of the detector to simulate experimental conditions by C.S. Arnold. This measurement was also taken almost 12 hours after the first measurement (c) and so the degraded film quality is responsible for the smaller signal[3]. Ultimately, for the characterization of the system, these plots will be scaled to a constant value of Φ_{ac} to compare them side by side.

A second difference between the three measurements arises from a variation of the extinction ratio ϵ. This has to be explained in more detail. The SNR measurements in this thesis have been performed many times on several films. It has been found that not all features of the SNR curve (especially for

[3]In fact, one might think that the smaller Kerr rotation is a result of the apertures. This has not been observed experimentally, however, so the film quality is the determining factor for the size of Φ_{ac}.

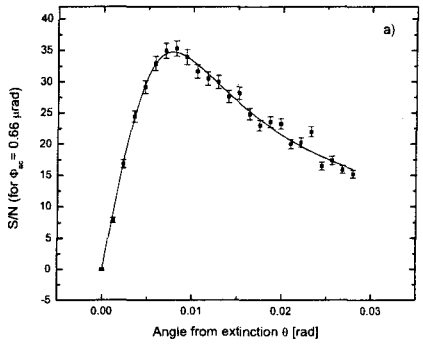

(a) taken last, with apertures

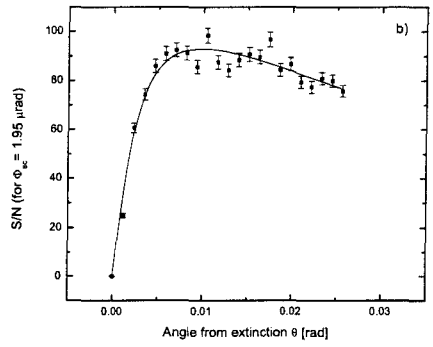

(b) taken second, without apertures

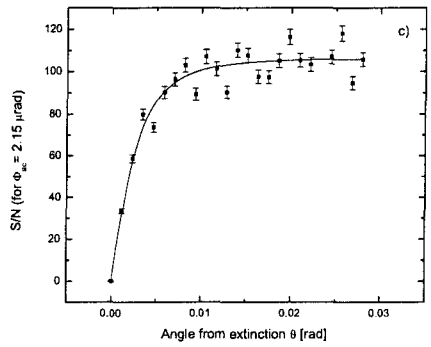

(c) taken first, without apertures

Figure 4.7: SNR measurements on a 1.5 ML Fe/2 ML Ni/W(110) film. The curves a) - c) are taken for different extinction ratios ϵ that determine the overall shape of the SNR curves. The absolute size of the SNR scales with the rms Kerr rotation Φ_{ac} which is also different for the three measurements.

large θ) have been reproducible. This was attributed to varying experimental conditions, such as the film quality, the temperature stability and, most importantly, the optical setup, i.e. the extinction ratio ϵ. In the measurements presented in this thesis, the experimental conditions have been slightly varied

through tiny changes in the optical alignment resulting in a range of ϵ values.

For the determination of ϵ and $V_{\max}$, the dc intensity at the photodetector has been recorded simultaneously with the ac modulated signal S at the lock-in from eq. 4.4. The data points in the plots were obtained from an average of about 500 points for each angular setting θ, resulting in a acquisition time of 4 minutes for one data point in the plot. The uncertainty of the data points results primarily from the uncertainty in Φ_{ac} and the standard deviation given by the average of the recorded points.

The data points were fit to the model in eq. 4.12 first by ignoring B and C for large θ, determining A. Then, C was approximately determined from the observed $\theta_{\max}$ (eq. 4.17). These parameters have then been used as starting values in a least square fitting procedure to find B, C and A. The fitting curves to the data are shown in figure 4.7. The fitting parameters and the noise contributions resulting from eq. 4.13-4.15 have been determined and are summarized in table 4.1. From the figure and the values in the table, several features can be discussed. First of all, the dependence of the SNR on ϵ is quite interesting.

For large values of ϵ, A gets smaller resulting in a smaller contribution from intensity noise $f(\omega)$. This can be explained when considering that for a larger ϵ, the alignment is not as perfect resulting in a smaller $V_{\max}$. The setup becomes less sensitive to changes in the recorded intensity. Another point regarding the intensity fluctuations arises from comparing $f(\omega)$ for setups with and without apertures: the noise is reduced by a factor of 2 when no apertures

	Arnold's SNR	run (a)	run (b)	run (c)
comments	with apertures	with apertures	without apertures	without apertures
detector gain G (V/A)	10^8	10^8	10^7	10^7
extinction ϵ ($\times 10^{-5}$)	0.17	0.583 ± 0.005	1.7 ± 0.2	2.3 ± 0.2
rotation Φ_{ac} (10^{-6} rad)	4.6	0.66	1.95	2.15
V_{max} from eq. 4.4 (V)	8600	4040 ± 30	2210 ± 20	1975 ± 25
A ($\times 10^{-12}$ 1/Hz)	180	8.2 ± 0.4	1.7 ± 0.3	0.028 ± 0.014
B ($\times 10^{-15}$ 1/Hz)	2.8	0.46 ± 0.07	1.4 ± 0.1	1.62 ± 0.06
C ($\times 10^{-20}$ 1/Hz)	2.6	3.0 ± 0.2	1.7 ± 0.3	2.2 ± 0.5
V_D from C and eq. 4.3 (10^{-7} V)	9.0	5.0 ± 0.2	2.1 ± 0.2	2.0 ± 0.3
$f(\omega)$ ($\times 10^{-6}$ /$\sqrt{\text{Hz}}$)	13	2.86 ± 0.07	1.30 ± 0.08	0.17 ± 0.05
$\delta\theta(\omega)$ (nrad/$\sqrt{\text{Hz}}$)	23.3	10 ± 1	18.3 ± 0.8	20.1 ± 0.4
θ_{max} (arcmin)	≈ 10	≈ 24	≈ 32	≈ 100

Table 4.1: Results of fits to the SNR measurements using eq. 4.12. The data by C.S. Arnold in the second column for the old setup is given here to facilitate the comparison.

are employed. This agrees with the idea that apertures are responsible for cutting the beam off when its position is fluctuating (through sample holder vibrations, for example).

Comparing the azimuthal noise $\delta\theta(\omega)$ in the three measurements a)-c),

there seems to be a correlation between the extinction ratio and the size of the angular noise, namely that it is smaller for smaller extinction ratios. This difference in angular noise is not believed to be due to the presence or absence of apertures, since $\delta\theta$ is related a change in polarization state which should not be influenced by the choice of apertures.

When comparing the values of $\delta\theta$ with measurements by C.S. Arnold (second column in table 4.1), it seems that the extinction ratio is not the only factor influencing $\delta\theta$. In fact, upon comparison of Arnold's value with the only other measurement using apertures (run a), the angular noise is reduced by a factor of 2 between the two setups. This implies that the present setup is mechanically more stable and resistant to angular fluctuations of the sample holder.

The last parameter of the fit C has been related to its dominant contribution, the detector noise N_D (and hence V_D). The determined values agree fairly well with the calculated values for V_D from the measured detector resistances. Furthermore, the mentioned reduction of the detector noise by roughly a factor of 3 by choosing a smaller gain is also confirmed.

Finally, the optimal angular setting to achieve the largest SNR has been determined from the parameters according to eq. 4.17. A shift in θ_{max} from 3 mrad (10 arcmin) for the old setup to larger values ($\geq$ 7.2 mrad (24 arcmin)) has been observed. The calculated value of θ_{max} depending on the different ϵ gives in principle the optimal operating point for the ac susceptibility measurements. However, as can be seen in the figures for larger ϵ (fig. 4.7(b)

and 4.7(c)), scatter in the SNR can be observed in the regions above $\theta = 30-35$ arcmin and thus this region is avoided. The origin of that scatter remains unclear. It has been suspected that the poor extinction ratio of the system might be related to light scattered in the crystal from the beam dump that influences the SNR at large θ. However, this does not explain why the SNR data is not scattered much for small θ where the possible scattering from imperfections of the beam dump should have the biggest influence.

As a consequence of the above considerations, it has been decided to choose a set angle of $\theta_{\max} = 24$ arcmin for all experiments. Furthermore, since the intensity noise $f(\omega)$ is reduced for setups without apertures as the beam gets no longer cut off, measurements are taken in that configuration - without apertures. This is also beneficial to the experimenter as the alignment with apertures usually takes a long time and has to be verified (and modified if necessary) very often due to vibrations of the sample holder. Also, without apertures, a smaller detector gain can be chosen (since the signal is larger) which effectively reduces the detector noise.

Direct comparison of the SNR with previous work

To get a better insight into how the performance of the present setup compares to the previous setup, the SNR is simulated from eq. 4.12 with the obtained parameters in table 4.1 for a Kerr rotation of $\Phi_{ac} = 4.6$ μrad. This value has been chosen to compare the present results directly to measurements by C.S. Arnold. Besides, a Kerr rotation response of around 4.6 μrad (4-5 μrad) is

often observed in the system under investigation. The resulting SNR curves are shown in figure 4.8.

As can be seen from the figure, the SNR reaches a maximum of about 350 which is about 2.5 times larger than that obtained previously. As will be seen later, this improvement opens the door to ac SMOKE measurements of antiferromagnetic films and ferromagnetic anisotropies.

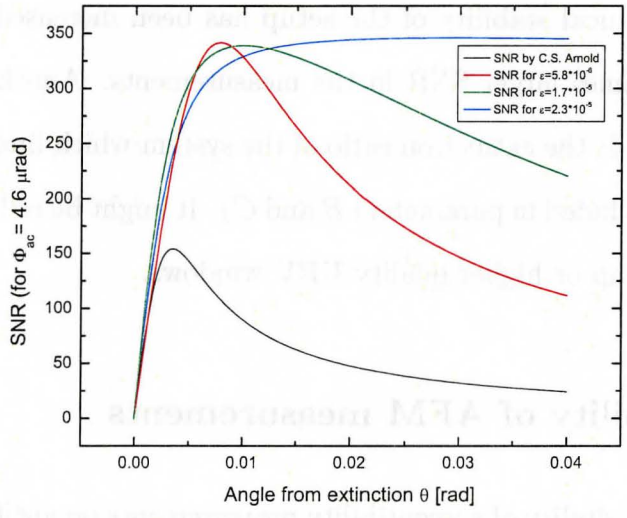

Figure 4.8: Simulated SNR data for $\Phi_{ac} = 4.6$ μrad. The black curve shows data obtained by C.S. Arnold [50] for an extinction ratio of $\epsilon = 1.7 \times 10^{-6}$. The red, green and blue curves are obtained for $\epsilon = 5.8 \times 10^{-6}$, $\epsilon = 1.7 \times 10^{-5}$ and $\epsilon = 2.3 \times 10^{-5}$, respectively.

Obviously, the SNR could be increased further. For example, one could imagine replacing the photodetector by a photomultiplier tube which would reduce the observed Johnson detector noise and shift θ_{max} to smaller values

(in particular, $\theta_{\max}$ shifts to the dc optimal setting of $\sqrt{\epsilon}$ if $N_{\mathrm{D}} \approx 0$).

Nevertheless, even with eliminating N_{D}, the size of the maximum SNR will not improve significantly, mainly because it is determined by the angular noise $\delta\theta$ in parameter B (which has been reduced by a factor of 2 in this thesis). When comparing past and present work on the performance of the system, it becomes clear that the main problem for the SNR in the ac SMOKE measurement, the lack of rigidity of the sample holder, still remains, even though the mechanical stability of the setup has been increased significantly leading to a 2.5 times larger SNR in the measurements. Another point that could be improved is the extinction ratio of the system which limits the overall sensitivity (it is included in parameters B and C). It might be reduced by using a better beam dump or higher quality UHV windows.

4.4.3 Feasibility of AFM measurements

To estimate the feasibility of susceptibility measurements on antiferromagnetic films with the present setup, the smallest detectable Kerr rotation Φ_{ac} is calculated. Consider the SNR parameters A, B, C obtained from measurement b) (fig. 4.7(b)) as a typical measurement situation with $\epsilon = 14$ arcmin, $f = 210$ Hz and $\tau = 2$ s. From eq. 4.12, the Kerr rotation Φ_{ac} at which signal and noise become equal is given by

$$\Phi_{\mathrm{ac}} = \frac{\sqrt{A\theta^4 + B\theta^2 + C}}{2\sqrt{\tau}\theta}. \tag{4.19}$$

With

$$A = 1.7 \times 10^{-12}\ 1/\text{Hz} \quad \text{and} \quad B = 1.4 \times 10^{-15}\ 1/\text{Hz},$$
$$C = 1.7 \times 10^{-20}\ 1/\text{Hz} \quad \text{and} \quad \theta = 6.98 \times 10^{-3}\ \text{rad},$$

the signal and noise become equal at a Kerr rotation of

$$\Phi_{ac} = 15\ \text{nrad}.$$

In fact, it has been observed experimentally that this result really is the resolution limit of the present setup under normal operating conditions for the recording of $\chi(T)$ curves (see figure 4.9(b)). This point is not obvious since all above calculations and measurements of the SNR were done for a constant temperature and did not take into account the influence of heating and cooling of the sample during the actual experiment. For example, in previous measurements by M. Dunlavy on a 1.8 ML Fe/W(110) film as shown in figure 4.9(a), the resolution limit for $\chi(T)$ is roughly 10 SI units which is equivalent to 0.4 μrad/Oe. This has been observed for many experiments. This resolution limit is in clear contrast to the one calculated from the SNR parameters by C.S. Arnold, which gives a limit of 40 nrad/Oe - 10 times better than actually observed in later experiments. This means that the present setup is actually a lot more sensitive (between 2.5 and 25 times more) than the setup just before this thesis began. The limit of resolution is given by $\Phi_{ac} = 15$ nrad for a frequency of 210 Hz, a time constant of 2 s and an extinction ratio of $\epsilon = 14$ arcminutes.

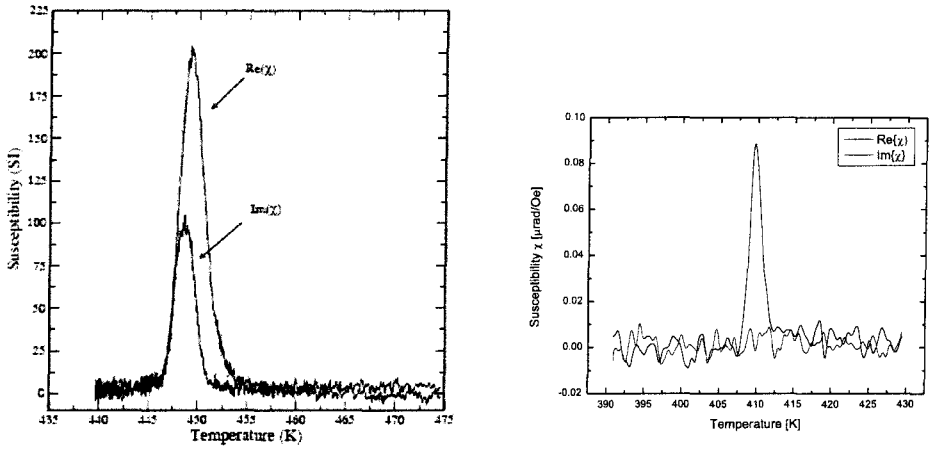

(a) (b)

Figure 4.9: Resolution limit in a typical $\chi(T)$ measurement on a 1.8 ML Fe/W film 4.9(a) in previous work and present work 4.9(b), in which $\chi(T)$ is measured along the hard [110] direction. (figure 4.9(a) taken from [26])

The resolution limit of the present setup of 15 nrad implies that, when looking at the estimated signal sizes in chapter 2.4, the signal of a 1 ML Co/CoO exchange coupled system could be barely detectable for an applied field of 3 Oe for which a rotation of 23 nrad is expected. In fact, even with the smaller estimate of 3.2 nrad/(ML Oe) from Oepen's Kerr rotation for the saturation magnetization of 16 μrad/ML of Co on a Cu substrate, a 5 ML thick Co/CoO film should suffice to detect a signal when a magnetic field of 2 Oe is applied.

Considering the direct observation of antiferromagnetic signals estimated from the observation of ferromagnetic hard axis susceptibility signals (estimated to give a signal of about 10 nrad/Oe for a 2 ML Fe/W(110) film),

the present setup is not expected to resolve the susceptibility peaks unless a much thicker film is used or a large field of 5 Oe is applied.

The improved sensitivity of the ac SMOKE measurements shows that the detection of antiferromagnetic signals from ultrathin films should now be feasible whereas it was impossible with the previous setup which had a resolution limit of about 0.3-0.4 μrad under the same experimental conditions.

Chapter 5

Transverse susceptibility measurements on Fe/W(110)

In this chapter, transverse susceptibility measurements on Fe/W(110) films are presented as a test study for the performance of the improved ac SMOKE setup. The goal is the detection of a small ferromagnetic transverse susceptibility signal on the order of nrad/Oe, estimated from previous experiments on Fe/W(110) and similar measurements by Jensen *et al.* on Co/Cu ultrathin films [30]. The Fe/W(110) system has been chosen because its structure and its magnetic properties have been studied extensively in the past [53]. However, to our knowledge, no transverse susceptibility measurements using the ac SMOKE technique have been reported yet.

The chapter is organized as follows. In the first part, a short introduction to the Fe/W(110) system is given with regard to film structure and film properties from previous magnetic measurements. Also, the expected Kerr rotations from anisotropy considerations are calculated. In the second part,

the performed experiments are described and the most important results are shown. Finally, in the last part, attempts at an interpretation of the results are made based on three aspects relevant for the system.

5.1 Introduction to the Fe/W(110) system

In the thickness regime considered in this thesis (1.5-2 ML), iron is known to grow pseudomorphically on the W substrate and in an approximate layer-by-layer (Frank-van der Merwe growth) fashion under the proper growth conditions. In particular, the first monolayer is deposited at room temperature, then annealed at 500 K for 2:30 minutes to encourage wetting. The second layer is then also grown at room temperature. Due to a strong uniaxial in-plane anisotropy (see later in this section), the easy axis of magnetization has been found to lie along the $[1\bar{1}0]$ direction in the film plane. This strong uniaxial anisotropy is also responsible for the two-dimensional (2D) Ising-like phase transition that has been observed in this system for film thicknesses close to 2 ML by determining the critical exponent γ of the magnetic (parallel) susceptibility [12].

In the following experiments, the transverse susceptibility on approximately 2 ML thick Fe/W(110) films is measured with a magnetic field applied along the hard magnetic axes [001] or [110]. To determine the magnitudes of the possibly detectable SMOKE rotations, two separate situations ([001] in-plane and [110] out-of-plane anisotropy) have to be considered. Con-

sider first the out-of-plane anisotropy. The free surface energy density for the Fe(110)/W(110) surface is given by [54]

$$K_s \cos^2\theta + K_{s,p} \sin^2\theta \cos^2\phi, \tag{5.1}$$

where θ is the angle from the surface normal [110] and ϕ is the in-plane angle from the hard [001] direction. Since K_s is positive and $|K_{s,p}| \ll |K_s|$, the film plane is the easy plane of the magnetization. The anisotropy field holding the spins in that plane is thus given by

$$H_{\text{an}} = \frac{K_s}{tM_{\text{sat}}}. \tag{5.2}$$

With the saturation magnetization of iron $M_{\text{sat}} = 1752\,\text{emu/(cm}^3\,\text{G)}$, a film thickness of $t = 5.6$ Å (2 ML) and the surface anisotropy constant $K_s = 3.2\,\text{erg/cm}^2$, the anisotropy field H_{an} attains a value of 32.6 kG. By applying a magnetic field H_0 perpendicular to the plane along [110], the magnetization can be deflected by a small angle φ out of the plane

$$\varphi = \frac{1}{H_{\text{an}}} H_0 = 30.7\,\frac{\mu\text{rad}}{\text{Oe}} H_0. \tag{5.3}$$

From this, the expected Kerr rotation Φ can be calculated using the Kerr rotation obtained for the saturated sample (250 μrad/ML)

$$\Phi = 250\frac{\mu\text{rad}}{\text{ML}} \times 2\,\text{ML} \times 30.7\,\frac{\mu\text{rad}}{\text{Oe}} H_0 = 15.3\,\frac{\text{nrad}}{\text{Oe}} H_0. \tag{5.4}$$

Similarly, for the in-plane anisotropy, the total free energy density is given by [54]

$$f = \frac{K_1}{4}(\sin^2(2\phi) + \sin^4\phi) - \frac{2K_{s,p}}{t}\sin^2\phi, \tag{5.5}$$

where $K_1 = 4.5\times10^5$ erg/cm^3 is the volume anisotropy and $K_{s,p} = 0.055$ erg/cm^2 is the surface anisotropy (considered equal for the two interfaces substrate-film and film-vacuum). The anisotropy field can be calculated from the effective in-plane anisotropy with the above values

$$H_{\text{an}} = \frac{|K_{\text{eff}}|}{M_{\text{sat}}} = \frac{|K_1/4 - 2K_{s,p}/t|}{M_{\text{sat}}} = 1.06\,\text{kG}, \tag{5.6}$$

giving an expected Kerr rotation of $\Phi = 0.472\,\frac{\mu\text{rad}}{\text{Oe}} H_0$. For the experiments in this chapter this means that if signals along the hard axes can be observed, the out-of-plane [110] response is expected to be 30 times smaller than the in-plane [001] response.

5.2 Experimental results

The films were grown according to the above mentioned growth recipe. The first monolayer was deposited at 300 K, then annealed at 500 K for 2:30 minutes to facilitate good wetting of the second layer. The thickness and structure of the first layer were monitored and verified by AES and LEED. The second layer was then again deposited at room temperature and the film thickness was determined by AES with an uncertainty of 0.2 ML. The homogeneity of the film was also verified using AES by recording spectra at different points on the substrate and calculating the substrate attenuation coefficients. LEED was used to align the sample along $[1\bar{1}0]$ or [001] with the magnetic field coils.

All measurements were performed in either the longitudinal (for $[1\bar{1}0]$ and [001] directions) or the polar ([110]) Kerr geometry. The first susceptibility

measurements were always taken along the easy $[1\bar{1}0]$ axis to find T_C for the film, to verify the film quality and to compare it with previous measurements by M. Dunlavy [12]. To that end, the real susceptibility peak sizes and FWHM have been determined, in some cases for different applied fields. In figure 5.1, some values obtained in this work have been superimposed (full circles) on previously measured values by M. Dunlavy (open circles), indicating that the films are of a comparable, equally high quality.

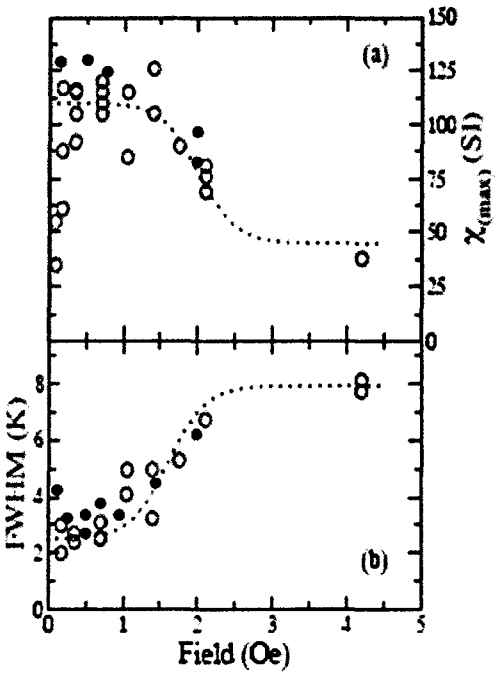

Figure 5.1: FWHM and real susceptibility peaks obtained in this work (full circles) and in previous measurements (empty circles) (taken from [12]).

Prior to the in-plane hard axis susceptibility measurement, the sample was carefully aligned with the axis of the magnetic coils by using the LEED

pattern of Fe(110)/W(110). The angular alignment is accurate to within ±2°. All measurements were performed at a modulating frequency of 150 Hz and at a lock-in time constant τ=2 s. The sample was heated radiatively from a W filament behind the sample with the slowest possible temperature rate of 0.05 K/s at the temperature controller (corresponding to an effective heating rate of 0.03 K/s). The applied ac magnetic field strength varied between 0.15 Oe and 2 Oe.

In figure 5.2, a typical measurement of the complex susceptibility along the easy and hard axes for a 1.85 ML thick Fe/W(110) film is shown for an applied field of 0.5 Oe. In figure 5.2(a), the complex susceptibility for the two in-plane directions [1$\bar{1}$0] (larger signal) and [001] (smaller signal) is shown. The hard axis susceptibility along [001] is shown again in more detail in figure 5.2(b), the hard axis $\chi(T)$ curve along the surface normal ([110]) is given in figure 5.2(c). Two especially interesting features in the hard axis measurements are the absence of an imaginary part Im$\{\chi\}$ and the narrow shape of the curve (small FWHM). This observation is common to all hard axis measurements and is taken as an indication that a "real" hard axis response is measured. This point will be discussed later.

As can be seen in the figures, both hard axis signals are very small. In fact, the resolution limit for this experiment lies at about 20 nrad/Oe, which is very close to the estimated 15 nrad/Oe from the SNR measurements.

A natural question that arises from the signals in figure 5.2(b) and 5.2(c) is whether they could have been measured with the previous setup. From

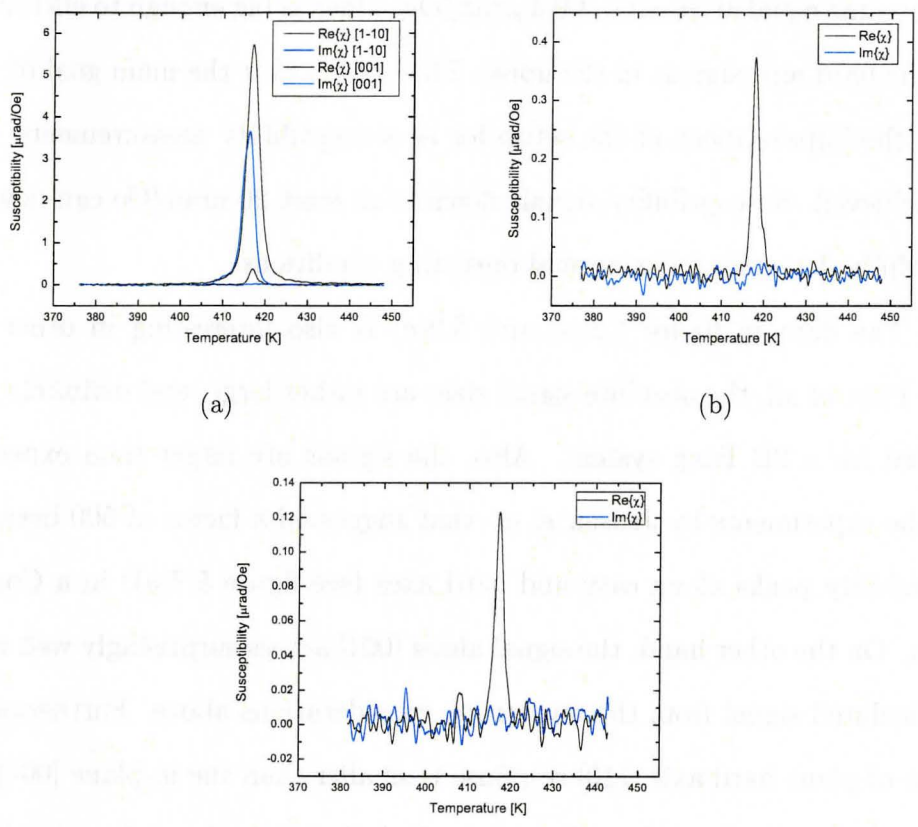

Figure 5.2: $\chi(T)$ measurements along different crystallographic directions. In 5.2(a), the parallel susceptibility along $[1\bar{1}0]$ (large signal) is compared to the transverse susceptibility along [001]. Figure 5.2(b) and 5.2(c) show the $\chi(T)$ measurements along [001] and [110], respectively. Note that in figure 5.2(c), the geometric factor due to the polar Kerr geometry has not been taken into account - the real signal is 4.2 times smaller.

the conclusions of chapter 4.4.2 and especially when looking at data that has been obtained previously by M. Dunlavy, the answer is no, the signals could not have been detected. Under normal operating conditions, the signal and

noise became equal at about 0.3-0.4 μrad/Oe, which is big enough to effectively bury the hard axis signals in the noise. This means that the main goal of this thesis, the improvement of the setup for ac susceptibility measurements, has been achieved. Susceptibility signals down to at least 20 nrad/Oe can now be successfully detected under normal operating conditions.

The data in figure 5.2(b) and 5.2(c) is also interesting in other aspects. First of all, the absolute signal sizes are rather large, and definitely not expected for a 2D Ising system. Also, the signals are larger than expected from the experiments by Jensen *et al.* that suggested a factor of 500 between susceptibility peaks along easy and hard axes (see figure 5.7(a)) in a Co/Cu system. On the other hand, the signal along [001] agrees surprisingly well with the calculated signal from the anisotropy considerations above. Furthermore, the out-of-plane hard axis [110] response is smaller than the in-plane [001] response as expected from the anisotropy calculation, though not by a factor of 30 but rather 16 (including the factor of 4.2 in sensitivity that the polar Kerr effect signals exceed the longitudinal signals). These two last points suggest that real hard axis responses are measured.

Secondly, it can be observed that the shape of the $\chi(T)$ curves along the hard axes is narrower than that along the easy axis. So far, no clear explanation for this behavior has been found. However, several experimental sources that might have contributed to this behavior have been ruled out based on additional experiments. These experiments also confirmed that the measured signals are real and not, for example, a result of an offset field at

the sample or of the chosen Kerr geometry.

Two important experiments were performed to confirm the results in figure 5.2. The first one considers the fact that the sample is heated radiatively by sending an ac current of 4700 Hz through the W heating filament beneath the substrate. It has been found previously that a dc heating current produced an offset field of 0.1 Oe at the sample surface. To determine whether the ac heating current had a similar effect or whether it is responsible for the shape of the $\chi(T)$ curves, the susceptibilities were measured during heating and cooling cycles, respectively. The cooling data were obtained with no current running through the filament. Since no changes were observed in the susceptibility curves with respect to the heating curves, it was concluded that a possible offset field does not influence the shape or the size of the observed signals.

The second experiment is related to the Kerr geometry employed in this thesis. In most measurements, the incident polarization of the light was chosen parallel to the plane of incidence (p-polarized). This fact is usually not relevant for longitudinal (or parallel) susceptibility measurements, however, it might be for transverse measurements. When the sample is rotated by 90 degrees to measure the transverse susceptibility, the large magnetic moment along the easy axis is oriented perpendicular to the p-polarization and can thus give rise to a Kerr signal (the transverse Kerr effect). Though this signal is expected to be extremely small, it might contribute to the shape of the susceptibility curve and even to the size of the recorded signal. One simple way to verify that the transverse Kerr effect did indeed not influence the

hard axis susceptibility measurements was the use of s-polarized light in the experiment. This experiment was performed and gave qualitatively the same result, i.e. similar narrow line shapes and absolute signal sizes. Unfortunately, the measurement was performed on a different film of a different thickness, such that the results are not quantitatively comparable. However, since no significant differences have been found, the Kerr geometry is ruled out as a factor contributing to the appearance of the specific shape of the hard axis signals.

5.3 Further experiments and discussion

After it has been established that the transverse susceptibility responses are related to some real physical process, the main focus in further experiments was the investigation of characteristic susceptibility features along the hard axes, namely the absence of an imaginary part and a narrow FWHM in the real susceptibility peak, with the goal to gain insights into the mechanisms responsible for the observed signals.

5.3.1 Transverse susceptibility χ_t along the [001] in-plane hard axis

In a first experiment, the in-plane hard axis response along [001] was examined. To that end, the transverse susceptibility was measured along [001] and at small angles from it. The measurements were compared with respect to the FWHM of the real susceptibility peak and with respect to the sizes of the real

and imaginary parts of the complex susceptibility. The results are shown in figures 5.3 and 5.4.

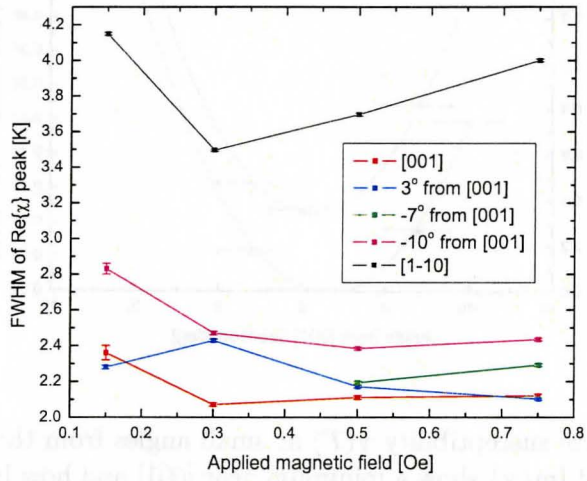

Figure 5.3: FWHM of the Re$\{\chi\}$ peak compared along easy [1$\bar{1}$0] and hard [001] axes and along small deviations from [001].

As can be seen in figure 5.3, the FWHM of the real susceptibility peak along the easy [1$\bar{1}$0] axis is almost twice as big as the FWHM along the hard [001] axis. Furthermore, small angular deviations from the hard axis lead to an increase in FWHM. It can also be observed that the trend in FWHM is independent of the applied field size in the region of 0.3-0.75 Oe, consistent with findings by M. Dunlavy. An increase in FWHM for extremely small fields is attributed to the fact that the real susceptibility peak signal nearly vanishes at these low fields, leading to increased noise and a wider FWHM.

Figure 5.4 shows the behavior of the real and imaginary susceptibility

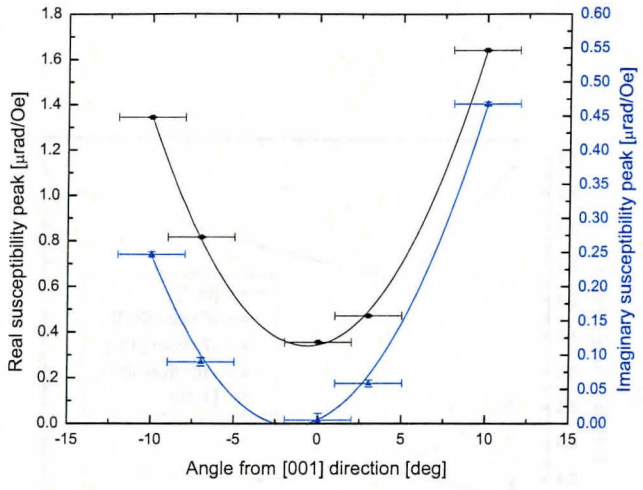

Figure 5.4: Transverse susceptibility $\chi(T)$ at small angles from the hard axis [001]. Note how $\mathrm{Re}\{\chi\}$ and $\mathrm{Im}\{\chi\}$ show a minimum near [001] and how $\mathrm{Im}\{\chi\}$ disappears along [001].

peaks near the hard [001] axis. Obviously, both components of the susceptibility exhibit the same dependence on the angle from the hard axis. The data can be well fitted by a $\sin^2\theta$ function, with a minimum along the hard axis for both $\mathrm{Re}\{\chi\}$ and $\mathrm{Im}\{\chi\}$. The most important features are the disappearance of $\mathrm{Im}\{\chi\}$ along [001] and the appearance of an imaginary part for angles θ from [001].

These features suggest the following interpretation of the signals: While the transverse susceptibility along [001] is a pure hard axis response, all other measurements at angles θ from the hard axis are a superposition of the transverse and parallel susceptibilities and therefore related to the critical fluctuations along the easy axis in the system. In particular, when the sample is

rotated by an angle ϑ, a small component of the large easy-axis moment is oriented parallel to the applied field, giving rise to a parallel susceptibility signal. This is supported by the fact that an imaginary part typical for the easy axis response arises in the susceptibility for $\theta \neq 0$ and that this χ'' increases with increasing rotation angle.

However, this observation does not explain the different shapes of the susceptibility curves or the absolute size of the signal. The only conclusion from the above argument is that critical fluctuations along the easy axis are not the source of the large hard axis response along [001] and that a different process must be involved in the creation of the signal. This assumption is also corroborated by the distinctly different observed FWHM.

5.3.2 Transverse susceptibility χ_t along the [110] out-of-plane hard axis

Consider next the transverse susceptibility measurements along the hard axis [110] perpendicular to the film. In principle, this measurement should be straightforward. However, it has been found that the out-of-plane signal depends crucially on the position of the sample in the plane. The reason for this can be explained best by looking at figure 5.5 in which the the real and imaginary susceptibility peaks as well as the FWHM are shown for a 1.9 ML Fe/W(110) film.

When the [110] transverse susceptibility is measured with the film being oriented along the easy axis ($\theta = 0$), a small signal in $\chi'_{[110]}$ and a comparably

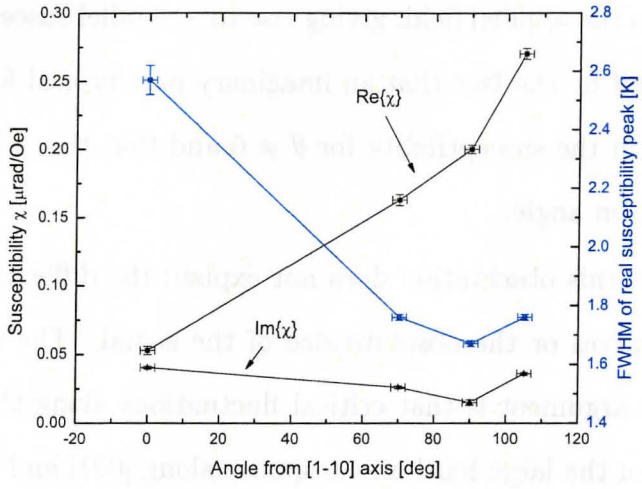

Figure 5.5: Transverse susceptibility $\chi(T)$ along [110] for different sample positions in the plane measured from $[1\bar{1}0]$. See text for details.

large signal in $\chi''_{[110]}$ is observed. The FWHM is large and comparable to the FWHM of the easy axis signal. This is shown in figure 5.6(a) and 5.6(c) where $\chi'_{[110]}$ and $\chi''_{[110]}$ are compared to the easy axis signals $\chi'_{[1\bar{1}0]}$ and $\chi'_{[1\bar{1}0]}$, respectively.

Upon rotation of the sample in the film plane, $\chi'_{[110]}$ increases while $\chi''_{[110]}$ and the FWHM decrease. A minimum for $\chi''_{[110]}$ and the FWHM is reached when the film is aligned along the in-plane hard axis ($\theta = 90°$). At this point, the imaginary part of the transverse susceptibility and the FWHM exhibit a similar behavior to the [001] in-plane hard axis case discussed before (this is shown in figure 5.6(d)). In contrast to the [001] measurement though, the real susceptibility peak along [110] does not reach its minimum at the same

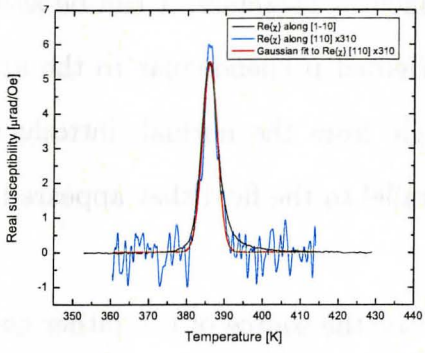

(a) Re{χ} along out-of-plane hard axis

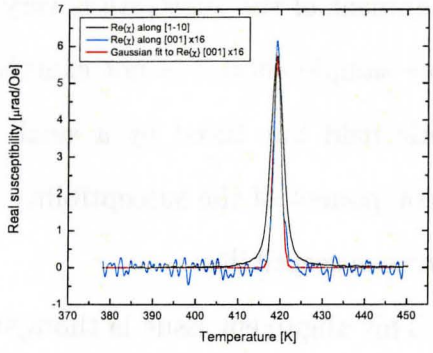

(b) Re{χ} along in-plane hard axis

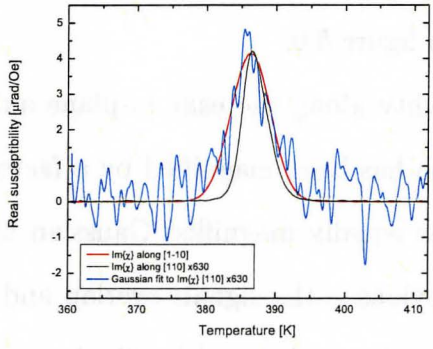

(c) Im{χ} along out-of-plane hard axis

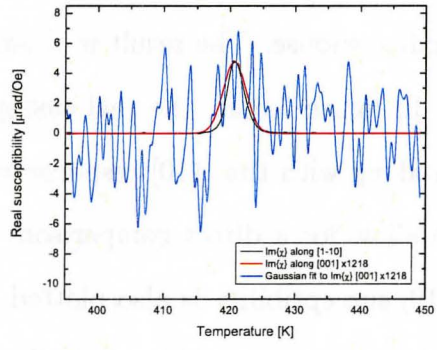

(d) Im{χ} along in-plane hard axis

Figure 5.6: Transverse real (imaginary) susceptibility signals along [1$\bar{1}$0] in 5.6(a) (5.6(c)) and [001] in 5.6(b) (5.6(d))are.compared to the shape of the easy axis signal. To that end, the hard axis response and a Gaussian fit to it have been magnified to allow for a direct comparison with the easy axis signal. Note that 5.6(a), 5.6(c) and 5.6(b), 5.6(d) have been measured on two different films.

position as the imaginary peak. It even increases when the sample is rotated further. This effect is a consequence of the sample mount and alignment.

As mentioned in chapter 3.1.2, the W substrate is held in a Ti ring by three W support wires forming a tripod. Due to this setup, a perfectly

flat alignment of the substrate is very difficult. Therefore, it can be assumed that the sample surface is not exactly oriented perpendicular to the applied magnetic field but tilted by a small angle from the normal, introducing a small component of the susceptibility parallel to the field that appears in the transverse susceptibility.

This alignment issue is thought to be the source of the rather complicated behavior of the transverse susceptibility $\chi_{[110]}$. Evidence that supports this idea has been found by comparing the two hard ([001] and [110]) with the easy axis response. The result is shown in figure 5.6.

In figure 5.6(a), the real susceptibility along the easy in-plane axis is shown along with the [110] response which has been magnified by a factor of 310 to allow for a direct comparison. The equally magnified Gaussian fit to the [110] susceptibility is also plotted. Obviously, the signals overlap and the peaks have the same width. A similar behavior is observed for the imaginary part of the susceptibility along [110] as shown in fig. 5.6(c) (even though the FWHM do not exactly match). This confirms the above assumption that a small tilt of the sample gives rise to the perpendicular susceptibility signal at $\theta = 0$ and that the recorded signals along $[1\bar{1}0]$ and [110] have indeed the same origin.

In comparison, consider figure 5.6(b) which displays the real susceptibility [001] in-plane hard axis response plotted in a similar fashion as in figure 5.6(a) to allow for a comparison. Note that the hard axis signal is only 16 times smaller than the easy axis signal. Moreover, the indication that a dif-

ferent mechanism is responsible for the hard axis signal is this case is that the hard axis signal clearly does not overlap with the easy axis signal. The FWHM is definitely different. Also, consider the imaginary parts $\chi''_{[110]}$ and $\chi''_{[001]}$ in figures 5.6(c) and 5.6(d), respectively. In the [110] case, the imaginary part has to be magnified by a factor of 630 to see an overlap of the Gaussian fit with the easy axis signal. As mentioned earlier, the FWHM do not perfectly match, but nevertheless, it can definitely be said that they somewhat overlap. On the other hand, in the [001] case, the imaginary response is extremely small and its Gaussian fit has to be magnified by 1218 to have the peak signal reach the easy axis peak. In fact, if one did not use a Gaussian fit (by supplying T_C to the fitting procedure), one could not even distinguish the peak from the noise, so it could be argued whether a signal is really there or not.

This behavior of a very narrow real χ' and a vanishing imaginary susceptibility χ'' is also observed for the out-of-plane response when the sample is oriented along [001] in the plane. However, the out-of-plane signal is usually 10 to 30 times smaller than the in-plane signal. This observation agrees with the ratio of 30 between in-plane and out-of-plane hard axis signal sizes estimated from the Fe/W(110) specific anisotropy constants in section 5.1. Nevertheless, it remains unclear whether the [110] transverse signal for the sample along [001] is a pure hard axis response or whether a small parallel susceptibility component contributes to the real susceptibility signal as well.

From a measurement such as shown in figure 5.6(a), the sample's tilt angle (between the normal and the magnetic field) at $\theta = 0$ can be estimated

using the absolute signal sizes of the real susceptibility measured at the same strength of the magnetic field. In the experiments, it has been found that the in-plane signal along the easy axis is usually 250 to 320 times bigger than the out-of-plane signal. These values imply that the sample is tilted by 0.18°-0.23° for a easy axis peak signal of 5.5 μrad/Oe.

5.3.3 Comparison to other work and interpretation of the transverse susceptibility signal

The first approach that might give some insight into the origin of the measured signals is given by the work of Jensen *et al.* [30]. They studied the transverse magnetic susceptibility of a 2.2 ML Co/Cu film by a SMOKE technique similar to that used in this thesis and related their measured signal to the anisotropy in the system.

The measurements for the in-plane hard and easy axes are shown in figure 5.7(a). The most remarkable findings are that a) the observed real transverse susceptibility peak at the phase transition is very broad (and noisy) and b) the applied field along the hard axis necessary to detect a transverse signal is five times larger than that applied along the easy axis, giving a ratio of the easy vs hard axis real susceptibility peaks of 500. Moreover, they demonstrate that the local, microscopic anisotropy persists above T_C in the paramagnetic regime and falls off slowly. They further show how to extract the microscopic anisotropy from the value of the inverse hard axis susceptibility $\chi^{-1}(T)$ at T_C. The obtained inverse susceptbilities are shown in figure 5.7(b).

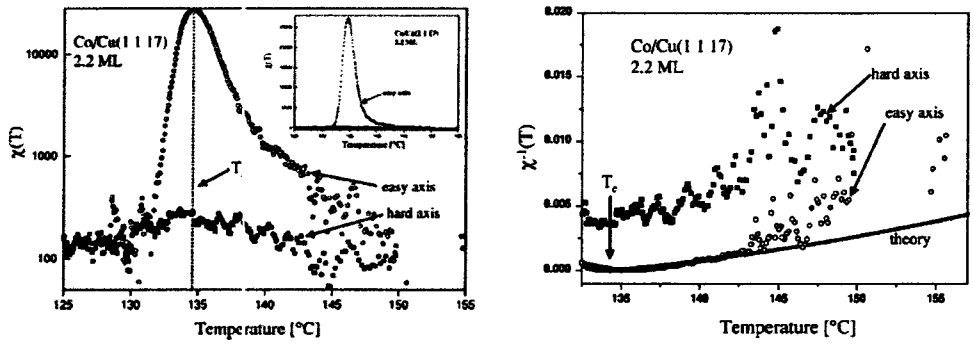

Figure 5.7: Figure 5.7(a): The parallel and transverse susceptibilities are shown for a 2.2 ML Co/Cu film along the in-plane easy and hard axes, respectively. The field applied along the hard axis is 5 times bigger than that applied along the easy axis. In figure 5.7(b), the inverse susceptibilities are shown for a temperature range near T_C. (taken from [30]).

The results by Jensen *et al.* differ from those obtained in this thesis in several aspects. Here, the transverse susceptibility peak is very narrow for the hard axis response and the magnetic field strength does not need to be increased to detect a signal. Especially the fact that our signal is sharply falling off to both sides of T_C in the same fashion does not agree with their results and seems to point to the fact that a different mechanism is responsible for the signals. Even if one thought that some dissipative processes in our films causes the susceptibility to decrease quickly below T_C, the sharp drop above T_C cannot be explained.

Moreover, the in-plane hard axis signal in this thesis has been observed to be only 15-40 times smaller than the in-plane easy axis signal, which is in clear contrast to Jensen *et al.*'s findings - they observed a 500 times smaller

signal.

In summary, the results of Jensen *et al.* clearly contradict our findings. They have found a small broad peak of the hard axis susceptibility while we have found a very sharp and quite large peak instead. From anisotropy arguments, the transverse susceptibility shape should be rather broad and not narrow.

Another measurement displaying the anisotropic behavior of the susceptibility near the phase transition has been put forward by Back *et al.* [55]. They describe the magnetic behavior of ultrathin Fe/W(110) films in the thickness regime between 1-2 ML within in a renormalization group approach.

In measurements on films between 1-2 ML thickness, Back *et al.* observed the transverse susceptibility as shown in the lower panel of figure 5.8. The susceptibility was not measured directly but was derived from the difference in magnetization curves using the Kerr effect. Since the field dependence was linear over a wide temperature range above and below T_C, the susceptibility $\delta M/\delta H$ could be calculated. Quite remarkably, the susceptibility displays a rather narrow peak with a FWHM of about 8 K for an applied field of 12 Oe. Assuming that the peak gets even narrower for smaller fields, an extremely narrow peak is expected for fields similar to those used in our measurements. Also, and this supports our measurements, the susceptibility drops to zero below T_C and does not stay constant as claimed by Jensen *et al.*. Therefore, it seems that the transverse susceptibility data presented in this thesis is likely to be in agreement with that of Back *et al.*. As a last aspect in the interpre-

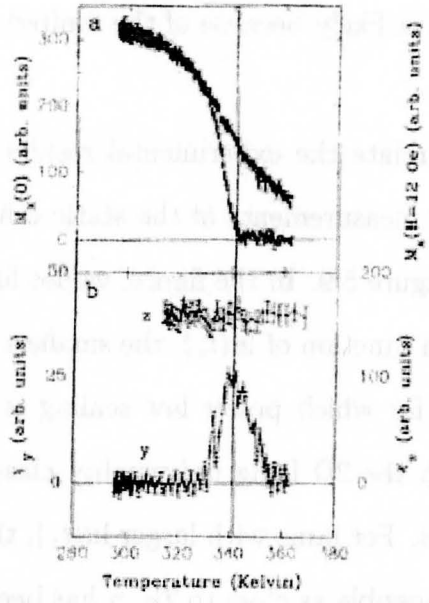

Figure 1. a) Temperature dependence of M_z in zero field and in an applied field of 12 Oe. b) Temperature dependence of M_y and M_z in an applied field of 12 Oe and 1.1 kOe, respectively.

Figure 5.8: In the lower panel: Behavior of the transverse magnetization $M(T)$ in an applied field of 12 Oe and 1.1 kOe for the hard y-axis ([001]) and z-axis ([110]) of a Fe(110)/W(110) film (1.4 ML), respectively (taken from [55]).

tation of the transverse susceptibility consider measurements that observe a 2D Ising-like behavior [12] for the Fe/W(110) system for film thicknesses near to 2 ML as performed in this thesis. In a 2D Ising system, a small transverse susceptibility signal is expected as shown by Fisher [56]. In fact, for a plane square lattice, the transverse susceptibility signal should be very broad ($\chi_t(T_C)/\chi_t(0) \approx 1.2$) and should drop off upon reaching its maximum value slightly above T_C.

In previous work by M. Dunlavy, no transverse susceptibility signal has

been observed. This is most likely because of the limited sensitivity of the old setup.

In an attempt to relate the experimental results in this thesis to M. Dunlavy's work, consider measurements of the static critical exponent of the susceptibility γ given in figure 5.9. In the figure, values for γ determined from many films are shown as a function of $\ln(t_x)$, the smallest value of the reduced temperature $(T/T_C - 1)$ for which power law scaling is valid. Obviously, γ exponents consistent with the 2D Ising universality class ($\gamma = 7/4$) are only observed for $\ln(t_x) < -5.4$. For films with larger $\ln(t_x)$, that is films for which power law scaling is not possible as close to T_C, γ has been shown to lie in the range of 2.3-3.5 which might indicate a dimensional crossover from the Ising to an anisotropic Heisenberg system.

Upon examination of figure 5.9 it can be seen that the results for the determined critical exponents are found to be correlated to the film thickness. For films thinner than 2 ML, and especially for films of 1.75 ML or a thickness below 1.5 ML, a non-2D Ising behavior has been observed. The films can be found in a range were $\ln(t_x) > -5.4$ and all show a γ that is larger than 2.3. This observation is consistent with the experience that the magnetic properties depend critically on the film thickness and morphology. Though quasi layer-by-layer growth is expected for the first 2 ML Fe/W(110) at least, some recent experiments [57] show that the growth might proceed in a more complicated way.

Looking at the thicknesses of the films used in this thesis, the following

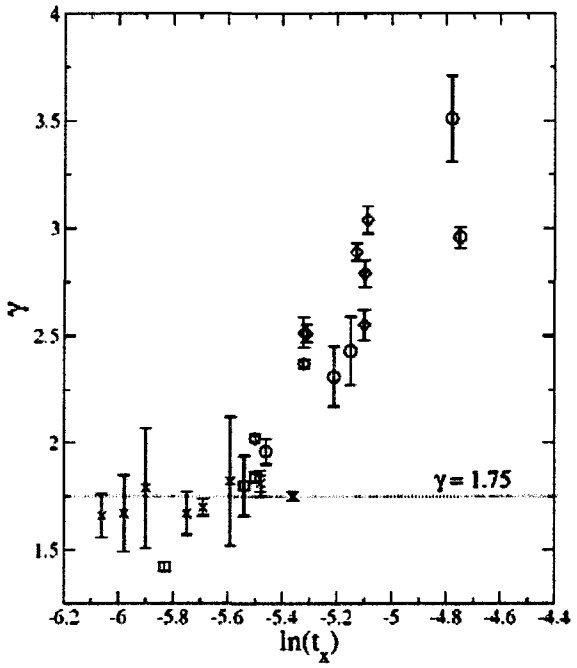

FIG. 6. Best-fit values of γ plotted as a function of reduced temperature cutoff, $\ln(t_x)$. Open circles represent films that are slightly less than 1.5 ML, squares are 1.5 ML films, diamonds are 1.75 ML, and X's are 2.0 ML.

Figure 5.9: Critical exponents obtained from many measurements on 1.5-2.0 ML thick Fe/W(110) films (taken from [12]).

can be observed: Though the thickness determination by AES indicates that films in a thickness range between 1.8-2.1 ML are grown in this thesis, the T_C determined from the susceptibility measurements are all in the range of 390-425 K. This does not agree with the findings of M. Dunlavy who attributed a much higher T_C of 450 K to a 1.8 ML thick film. The reason for this discrepancy is unclear, since the growth conditions are essentially identical. It might be possible that the present iron source is of inferior quality that results

in a reduction of T_C. However, it seems more likely that all films grown in this thesis are too thin and that their unexpected behavior is a consequence of this. Alternatively, the films grown by M. Dunlavy could be all too thick - but this hypothesis cannot be verified.

Finally, the size of the transverse susceptibility peak and the reason for the particular shape remain unclear. It seems that the peak is too sharp to result from anisotropies or a 2D Ising-like transverse susceptibility. Rather, it looks like some critical process is responsible for the peak, though it is not from an easy axis critical fluctuation.

In an attempt to gain further insight into the origin of the transverse susceptibility peak or if it is related to some 2D Ising-like behavior, the following experiments could be envisioned: First of all, a thicker film should be grown with a Curie temperature corresponding to that found for 2 ML (465 K) by M. Dunlavy. Then it would be very interesting to see whether a transverse susceptibility can be measured. Another experiment could involve the determination of the critical exponent in the experiments on the transverse susceptibility in films as grown in this thesis ruling out or confirming a 2D Ising-like behavior of the film under consideration.

Chapter 6

Conclusion

This thesis has dealt with the optimization of magnetic ac susceptibility measurements by the surface magneto-optic Kerr effect in the investigation of ultrathin magnetic films. Several modifications to the experimental setup and to the measurement method have been implemented. In particular, the mechanical stability of the setup has been enhanced and the optical setup for the detection of the Kerr effect has been refined to reduce the influence of mechanical vibrations from the sample holder.

The performance of the system has been investigated by measuring the signal-to-noise ratio in ac susceptibility measurements. The data were analyzed by employing a simple model that incorporates the three major system-specific noise sources: 1) Intensity fluctuations at the detector through deflections of the laser beam and 2) through polarization rotation changes due to sample holder vibration and 3) detector noise. As a main result of this analysis, it has been found that the effect of mechanical vibrations inherent

to the UHV system cannot be completely eliminated, but that its influence on the measurements can be reduced by removing apertures that have been employed in previous work. The SNR can be maximized by performing measurements with a smaller detector gain at a different angular set point ($\theta = 24$ arcminutes). Overall, the modifications to the system have led to an increase in the signal-to-noise ratio in the ac susceptibility measurements of at least a factor of 2.5.

The detection limit of the ac susceptibility measurements in units of Kerr rotation is found to be 15 nrad/Oe under normal operating conditions. This is about one magnitude smaller than observed in other measurements performed prior to this thesis and by other groups. The increase in sensitivity is considered to make ac susceptibility measurements feasible on antiferromagnetic ultrathin films that exhibit a much smaller response than ferromagnets (on the order of nrad/Oe). The detection of the antiferromagnetic critical properties using the ac susceptibility signals from exchange coupled ferromagnetic/antiferromagnetic bilayers should be unproblematic even for very thin (3 ML) films. On the other hand, the direct observation of the antiferromagnetic state expected for ultrathin film systems such as Cr/W(110) or Mn/W(110) is more challenging and might only be possible for rather thick (5 ML) films or applied driving fields of several Oersted.

As a test study for the optimized system, transverse susceptibility measurements on 1-2 ML thick Fe/W(110) films have been performed in this thesis with surprising results. First of all, a transverse susceptibility signal could be

detected. This can be rated as a major success of this thesis. It has been shown that the detection of these signals is a direct result of the improved ac SMOKE susceptibility setup.

The transverse susceptibility signals from the investigated Fe/W(110) films exhibit interesting features. The susceptibility peak signals along the magnetically hard axes are found to be bigger than expected from anisotropy considerations and are not in agreement with other work [30] that observed a small and broad susceptibility peak near T_C. The measured transverse susceptibility in this thesis exhibits a distinct narrowing of the line shape.

The source of the transverse signals as well as their size and shape are not fully understood but possible scenarios were discussed. It has been concluded that the signals do not arise from easy axis critical fluctuations near T_C and that they are most likely not a result from the system's anisotropy. Furthermore, the shape of the peaks suggests that the observed signal is not related to a theoretically expected broad transverse susceptibility in a 2D Ising system. Based on the narrow shape of the peak, it is hypothesized that some critical process is involved in the creation of the signal, however, it is not yet understood what that process might be.

Bibliography

[1] B. Heinrich and J.A.C. Bland (Eds.), *Ultrathin Magnetic Structures Volume I-IV*, Springer-Verlag Berlin Heidelberg 1994

[2] S.A. Wolf, A.Y. Chtchelkanova, and D.M. Treger, IBM J. Res. Develop. **50**, 101 (2006)

[3] Z.Q. Qiu and S.D. Bader, Rev. Sci. Instrum. **71**, 1243 (2000)

[4] P.J. van der Zaag, Y. Ijiri, J.A. Borchers, L.F. Feiner, R.M. Wolf, J.M. Gaines, R.W. Erwin, and M.A. Verheijen, Phys. Rev. Lett. **84**, 6102 (2000)

[5] M. Bode, E.Y. Vedmedenko, K. von Bergmann, A. Kubetzka, P. Ferriani, S. Heinze, and R. Wiesendanger, Nature mat. **5**, 477 (2006)

[6] W. Kuch, F. Offi, L.I. Chelaru, M. Kotsugi, K. Fukumoto, and J. Kirschner, Phys. Rev. B **65**, 140408 (2002)

[7] D.P. Pappas, K.P. Kamper, and H. Hopster, Phys. Rev. Lett. **64**, 3179 (1990)

[8] S. Pütter, H.F. Ding, Y.T. Millev, H.P. Oepen, and J. Kirschner, Phys. Rev. B **64**, 092409 (2001)

[9] C.S. Arnold, H.L. Johnston, and D. Venus, Phys. Rev. B **56**, 8169 (1997)

[10] H.B. Callen, and E. Callen, J. Phys. Chem. Sol. **27**, 1271 (1996)

[11] C.S. Arnold, Ph.D. thesis, McMaster University, Hamilton, Canada (1997)

[12] M.J. Dunlavy and D. Venus, Phys. Rev. B **69**, 094411 (2004)

[13] A. Aspelmeier, M. Tischer, M. Farle, M. Russo, and K. Baberschke, J. Magn. Magn. Mater. **146**, 256 (1995)

[14] J. Nogués and I.K. Schuller, J. Magn. Magn. Mater. **192**, 203 (1999)

[15] D. Venus and F. Hunte, Phys. Rev. B **72**, 024404 (2005)

[16] J.H. van Vleck, J. Chem. Phys. **9**, 85 (1941)

[17] T.R. McGuire, E.J. Scott, and F.H. Grannis, Phys. Rev. **102**, 1000 (1956)

[18] C. Kittel, *Introduction to Solid State Physics*, Wiley New York (2004), p. 467

[19] S.D. Bader, E.R. Moog, and P. Grünberg, J. Magn. Magn. Mater. **53**, L295 (1986)

[20] P. Asthana, B I. Finkelstein, and A.A. Fennema, IBM J. Res. Develop. **40**, 543 (1996)

[21] P.N. Argyres, Phys. Rev. **97**, 334 (1955)

[22] J.L. Erskine and E.A. Stern, Phys. Rev. B **8**, 1239 (1973)

[23] P. Bruno, Y. Suzuki, and C. Chappert, Phys. Rev. B **53**, 9214 (1996)

[24] J. Zak, E.R. Moog, C. Liu and S.D. Bader, Phys. Rev. B **43**, 6423 (1991) and Phys. Rev. B **46**, 5883 (1992)

[25] J. Zak, E.R. Moog, C. Liu and S.D. Bader, J. Magn. Magn. Mater. **89**, 107 (1990)

[26] M.J. Dunlavy, Ph.D. thesis, McMaster University, Hamilton, Canada (2003)

[27] Z.Q. Qiu, J. Pearson, and S.D. Bader, Phys. Rev. B **46**, 8195 (1992)

[28] T. Ambrose and C.L. Chien, Phys. Rev. Lett. **76**, 1743 (1996)

[29] H.P. Oepen, S. Knappmann, and W. Wulfhekel, J. Magn. Magn. Mater. **148**, 90 (1995)

[30] P.J. Jensen, S. Knappmann, W. Wulfhekel and H.P. Oepen, Phys. Rev. B **67**, 184417 (2003)

[31] R. Vollmer, S. van Dijken, M. Schleberger, and J. Kirschner, Phys. Rev. B **61**, 1303 (2000)

[32] U. Gradmann and G. Waller, Surf. Sci. **116**, 539 (1982)

[33] M. Przybylski, I. Kaufmann and U. Gradmann, Phys. Rev. B **40**, 8631 (1989)

[34] H.L. Johnston, C.S. Arnold, and D. Venus, Phys. Rev. B **55**, 13221 (1997)

[35] S. Mróz and A. Mróz, Thin Solid Films **367**, 126 (2000)

[36] H. Jenniches, M. Klaua, H. Höche and J. Kirschner, Appl. Phys. Lett. **69**, 3339 (1996)

[37] T. Jones, J. Sawler, and D. Venus, Rev. Sci. Instrum. **64**, 2008 (1993)

[38] M. Wuttig and X. Liu, *Ultrathin Metal Films - Magnetic and Structural Properties*, Springer-Verlag Berlin Heidelberg New York 2004, p. 6

[39] P. Auger, J. Physique Radium **6**, 205 (1925)

[40] C.J. Davisson and L.H. Germer, Phys. Rev. **30**, 705 (1927)

[41] M.A. Van Hove, W.H. Weinberg, C.-M. Chan, *Low-Energy Electron Diffraction - Experiment, Theory and Surface Structure Determination*, Springer-Verlag Berlin Heidelberg New York 1986

[42] J.B. Pendry, *LEED - The Theory and its Application to Determination of Surface Structure*, Academic Press 1974

[43] C. Schmidthals, D. Sander, A. Enders and J. Kirschner, Surf. Sci. **417**, 361 (1998)

[44] C.A. Ballentine, R.L. Fink, J. Araya-Pochet, and J.L. Erskine, Appl. Phys. A **49**, 459 (1989)

[45] B. Heinrich and J.A.C. Bland (Eds.), *Ultrathin Magnetic Structures Volume II*, Springer-Verlag Berlin Heidelberg 1994, Ch. 2

[46] W.S. Kim, M. Aderholz and W. Kleemann, Meas. Sci. Technol. **4**, 1275 (1993)

[47] K. Sato, H. Hongu, H. Ikekame, Y. Tosaka, M. Watanabe, K. Takanashi and H. Fujimori, Jpn. J. Appl. Phys. **32**, 989 (1993)

[48] R.M.A. Azzam and N.M. Bashara, *Ellipsometry and Polarized Light*, North Holland New York 1977

[49] C.S. Arnold and D. Venus, Rev. Sci. Instrum. **66**, 3280 (1995)

[50] C.S. Arnold, M. Dunlavy, and D. Venus, Rev. Sci. Instrum. **68**, 4212 (1997)

[51] M.J. Dunlavy, M.Sc. thesis, McMaster University, Hamilton, Canada (1998)

[52] see, for example, J.J. Sakurai, *Modern Quantum Mechanics (Revised Edition)*, Addison-Wesley Publishing Company, Inc. (1994), p. 331ff

[53] for example, see U. Gradmann, J. Korecki, and G. Waller, Appl. Phys. A **39**, 101 (1986); H.J. Elmers, J. Hauschild, and U. Gradmann, Phys. Rev. B **54**, 15224 (1996) or M.J. Dunlavy and D. Venus, Phys. Rev. B **69**, 094411 (2004)

[54] U. Gradmann, J. Korecki, and G. Waller, Appl. Phys. A **39**, 101 (1986)

[55] C.H. Back, A. Kashuba, and D. Pescia, Phys. Low-Dim. Struct. **2**, 9 (1994)

[56] M.E. Fisher, J. Math. Phys. **4**, 124 (1963)

[57] N. Weber, K. Wagner, H.J. Elmers, J. Hauschild, and U. Gradmann, Phys. Rev. B **55**, 14121 (1997)